

25
63 84942
Order 5

18 P

NASA CR-51029

Research Summary No. 36-2 Volume I, Part One

for the period February 1, 1960 to April 1, 1960



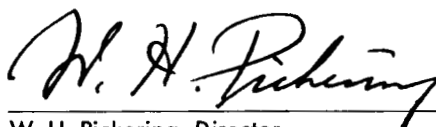
JET PROPULSION LABORATORY
CALIFORNIA INSTITUTE OF TECHNOLOGY
PASADENA, CALIFORNIA

April 15, 1960

CASE FILE COPY

Preface

The Research Summary is a report of supporting research and development activities at the Jet Propulsion Laboratory, California Institute of Technology. This bimonthly periodical is issued in two volumes. *Volume I, Part One*, contains unclassified information concerning the deep space instrumentation facilities, spacecraft communication techniques, satellite and interplanetary trajectories, and guidance and control techniques. *Volume I, Part Two*, contains unclassified information on instrumentation, computers, materials, propulsion techniques, gas dynamics, physics and mathematics. *Volume II* contains the information classified Confidential about propulsion systems and wind tunnel development testing.



W. H. Pickering, Director
Jet Propulsion Laboratory

Copyright © 1960
Jet Propulsion Laboratory
California Institute of Technology

Contents

I. Deep Space Instrumentation Facility	1
A. Goldstone Station	1
B. Goldstone Transmitter Site	7
C. Goldstone Receiver Site	9
D. Mobile Tracking Station	12
II. Spacecraft Communications	15
A. Communications System Components	15
B. Analysis of Coherent Two-Way Doppler Communication System . .	23
C. Deep Space Range Measurement	26
III. Systems Analysis	37
A. Trajectory Analysis	37
B. Orbit Determination	42
C. Systems Analysis Research	44
D. Space Flight Studies	46
E. Powered Flight Studies	49
IV. Spacecraft Guidance and Control Techniques	51
A. Spacecraft Attitude Sensing Techniques	51
B. Low-Noise Amplifier Studies	56
C. Molecular Aggregate Devices	58
D. Gas Bearings	58
E. Parasol Solar Panel and Antenna	62
References	64

I. DEEP SPACE INSTRUMENTATION FACILITY

A. Goldstone Station

1. Project Echo

The transmit-receive stations located at Goldstone, California (JPL operated), and Holmdel, N. J., Bell Telephone Laboratories operated (BTL), will provide an east-to-west communication link at 960.05 mc and a west-to-east communication link at 2390 mc via a 100-foot diameter balloon functioning as a passive repeater. An additional 2388-mc signal will be used at the Goldstone site to track the balloon, described in *Space Programs Summary No. 6 (SPS 6)* Section III, and provide data useful for orbit determination. Approximately 1 kw of RF power will be transmitted to the balloon from the Goldstone transmitting site to provide a balloon-reflected signal for the 2388-mc tracking receiver at the Goldstone receiving site.

a. Moon-bounce experiments, 960.05 mc. The fourth in a series of Moon-bounce tests leading to the Project Echo balloon-bounce experiment was conducted between the hours 0000 GMT and 0900 GMT, 10 February 1960. (See *SPS 37-1* for a description of earlier experiments.) The period of the test was divided into two sections of 4 hours each for the purpose of fulfilling the specific test objectives of both BTL and JPL. The primary objective of the

test was to provide an evaluation of narrow-band FM transmission over the Moon reflection path. Secondary objectives were to (1) provide additional data on CW propagation via the Moon, (2) determine the effects of the transmission media and the Moon's reflecting surface on a phase modulated signal, (3) secure additional operational training for Project Echo, and (4) secure additional information on the instrumentation requirements for measuring lunar characteristics. A preliminary evaluation of the results for the JPL portion of the test has been completed and is reported here.

During the CW portion of the test, the BTL transmitter, using the JPL exciter (*SPS 37-1*, pp 42, 43) in conjunction with the BTL 10-kw amplifier and 60-foot-diameter parabolic antenna, beamed a 10-kw signal at the Moon. The 960.05-mc low-noise listening receiver at Goldstone was operated as a phase coherent system with equivalent noise bandwidths (at the received signal level) of 16, 40, and 140 cps. The average carrier frequency as read out at the Goldstone station was 960.04522 mc.

The average received signal level as measured at the Goldstone receiver input was $-120 \text{ dbm} \pm 3 \text{ db}$. The total measured circuit loss for the 960.05-mc signal via the Moon from an isotropic radiator to an isotropic collector on the Earth was $278 \pm 5 \text{ db}$. The circuit loss is determined from the average received signal level, the BTL

measured transmitter power of 10 ± 0.25 kw, and the following system parameters:

Transmitter

Antenna gain	43.5 ± 1 db
Antenna ellipticity	0.8 db
Antenna polarization	right-hand circular
Transmission line loss	0.6 db

Receiver

Antenna gain	46.2 ± 1.0 db
Antenna ellipticity	± 0.3 db
Antenna polarization	left-hand circular
Transmission line feed loss	0.2 db

Distance to the Moon

(calculated from parallax) 249,300 miles

Using the radar equation and the measured value of received signal level, the radar cross section of the Moon was determined as 8.1×10^{10} meters². This represents 0.0085 of the projected area of the Moon (projected area = 9.5×10^{12} meters²) or a reflection loss with respect to a perfect sphere of 20.7 db. The measurement uncertainty is approximately ± 5 db.

For all three values of the receiver noise bandwidth, the RF dynamic phase error reached maximum peak-to-peak values of ± 90 degrees in a recording bandwidth of 1 kc. The RF dynamic phase error for CW transmission while using the 140-cps RF-loop bandwidth is shown in Figure 1. The waveform of the CW signal reflected from the Moon indicated an amplitude modulation of approximately ± 7.5 db.

During a portion of the test, the carrier was phase-modulated with single-tone sine waves ranging in frequency from 10 cps to 5 kc. The measurements of phase modulation of the signal received via the Moon path agreed essentially with the corresponding measurements while using the collimation tower. This indicates that very little of the phase modulation was converted into AM by the transmission media and the Moon's reflecting surface.

The threshold of the low-noise 960-mc phase coherent receiver as measured prior to the Moon bounce experiment (antenna directed at the collimation tower) was -162 dbm. This is in fair agreement with the value of -161.1 dbm as calculated from the apparent antenna temperature of 88°K, the measured noise figure of 2.75 db, and the 0.2 db loss in the antenna feed and transmission line. The calculated threshold with the antenna directed at the Moon was -161.4 dbm (based on the apparent antenna temperature of 58°K and the noise figure and feed loss listed above) while the threshold test using the Moon-reflected signal indicated a value of -162 +3, -0 dbm. Thus, the measurements show that within the accuracy of the experimental data, the threshold via the Moon path is essentially the same as the threshold using the signal generator at the collimation tower method. This indicates that there is very little broadening of the spectral line of the CW signal upon reflection from the Moon's surface.

b. Moon-bounce experiments, 2388 mc. On 3 March 1960, approximately 1 kw of RF power was transmitted from the Goldstone transmitting site to the Goldstone receiving site via the Moon. Automatic tracking of the

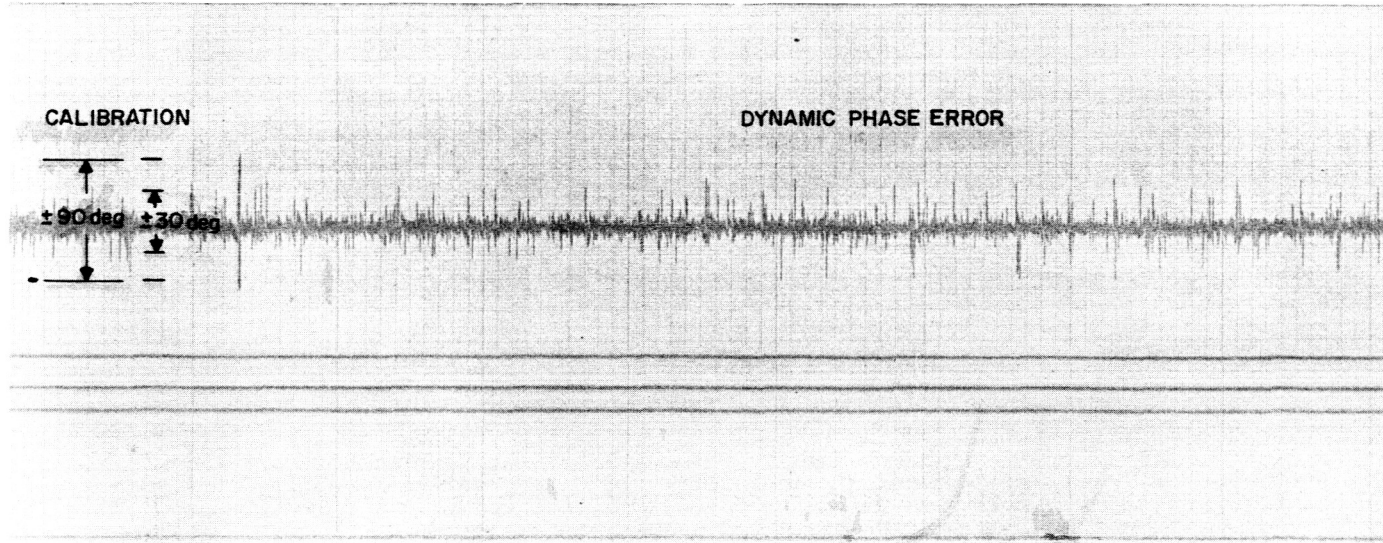


Figure 1. Recording of RF dynamic phase error during Moon-bounce experiment

Moon-reflected 2388-mc signal was accomplished at the Goldstone receiver site. Further evaluation of the tracking system is planned using reflected signals from both the Moon and dark satellites.

2. Angular Encoding System

The angular encoding systems are now installed at the Goldstone transmitter and receiver antennas. Each digital and decimal channel is identified with either the azimuth or elevation axis. Specifications for overall design accuracy were 20 seconds of arc, rms, or better; i.e., the indication of the angular position of a shaft to which the multipoled resolver (sensor) is directly coupled is to be accurate to 20 seconds of arc or 0.0056 degree, rms. Referring to SPS 5 for a description of the system, the overall system accuracy is affected by the inaccuracies of the flexible coupler, the multipoled resolver, and the servo-repeater (followup), which includes the mechanical and the encoding disk assemblies. Compensation cams are used to reduce the repeatable errors in the multipoled resolver and mechanical gearing.

Each angular encoding system was optically checked to determine the overall system accuracy. The results for the two complete systems (including both binary and decimal channels) have now been plotted and analyzed.

The system accuracy test setup is pictured in Figure 2. The sensors consisting of a single-poled and a multipoled resolver transmitter are positioned angularly by means of a T-3 theodolite. This results in a multiple angular change in the binary and decimal encoding disks' position. A combined electronic and mechanical stepup takes place in the servo-repeater (followup). Conducting and nonconducting segments on the encoding disks are sensed by brushes and displayed visually. A binary lamp bank (each lamp represents the state of one of 18 binary digits) and a projection type inline decimal readout shown in Figure 2 are the visual displays.

The visual displays provide an indication of count transition at which all measurements are taken. This eliminates the effect of quantizing error inherent in all digital systems and confines the measurement to those inaccuracies which are theoretically removable.

Having positioned the shafts of the resolvers for a particular count transition, the telescope portion of the theodolite is returned to a zero reference target. A fixed positioned reticle in the telescope of a T-2 theodolite serves as a target. A direct reading by means of optics within the T-3 theodolite indicates the rotation undergone by the resolver shafts to an accuracy of ± 1 second of arc. The multipoled resolver serves as an input-output comparator of the servo-repeater in the region of the single-poled resolver's null. The single-pole resolver becomes part of the loop only for coarse positioning required to remove pole ambiguity of the multipoled resolver.

The comparison between the encoding disks' output at a particular count transition and the optical reading of the rotation of the multipoled resolver (to bring about the count transition) represents each data point in Figure 3. The measurements were used to calculate the sample mean and rms errors as shown below:

$$x^* = \frac{1}{n} \sum_{k=1}^n (x_{ks} - x_k)$$

$$s^* = \left\{ \frac{1}{n} \sum_{k=1}^n [x^* - (x_{ks} - x_k)]^2 \right\}^{0.5}$$

where x^* is the sample mean angular error, x_{ks} the k th reading of the angle represented by the encoder output count, x_k the k th reading of the angular position of the input shaft of the multipoled synchro resolver, s^* the rms error about the sample mean, and n is 100 or greater.

As shown on Figure 4, the rms accuracy for each channel was better than 0.0056 degree, or 20 seconds of arc, rms.

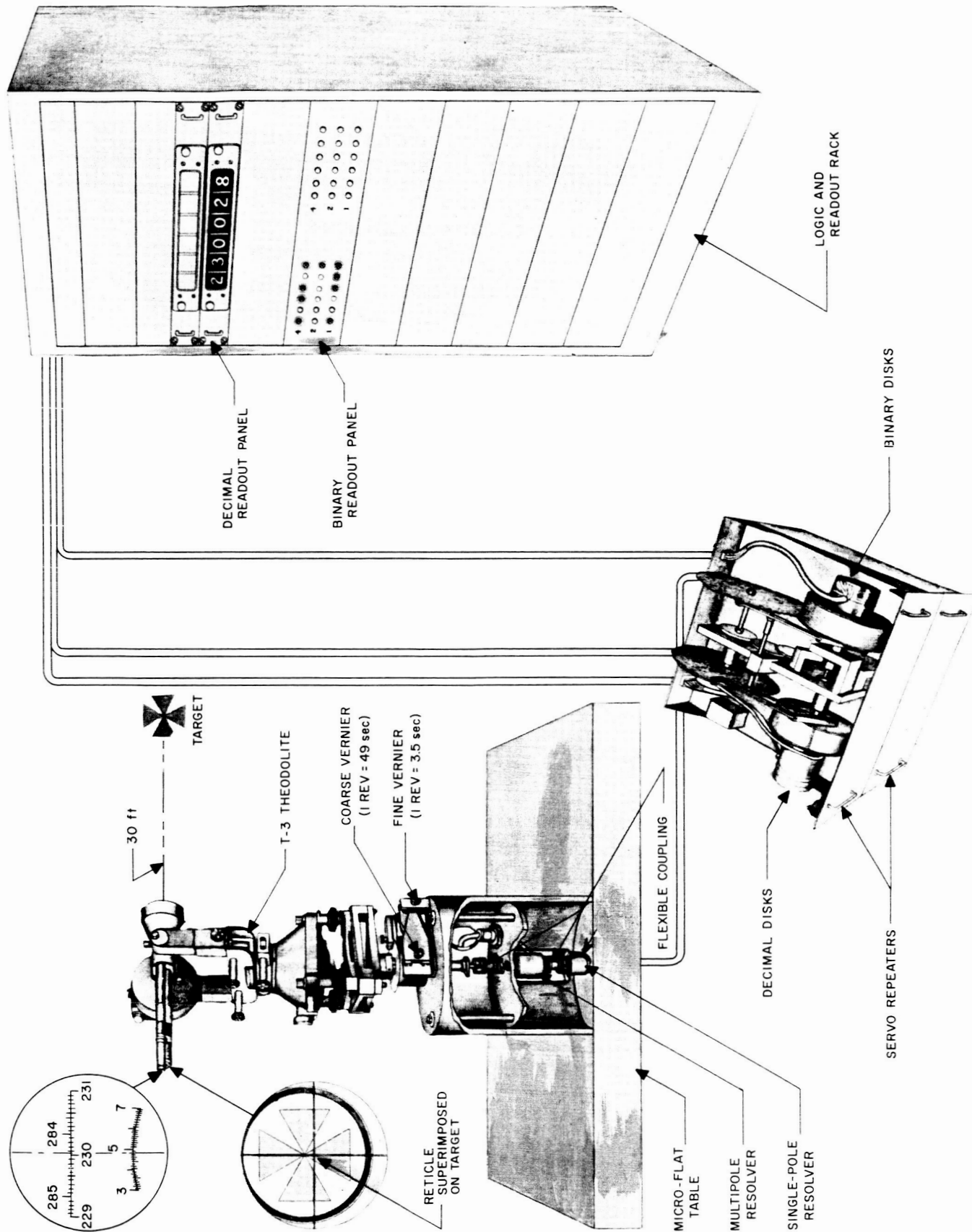


Figure 2. Angular encoding system accuracy test setup

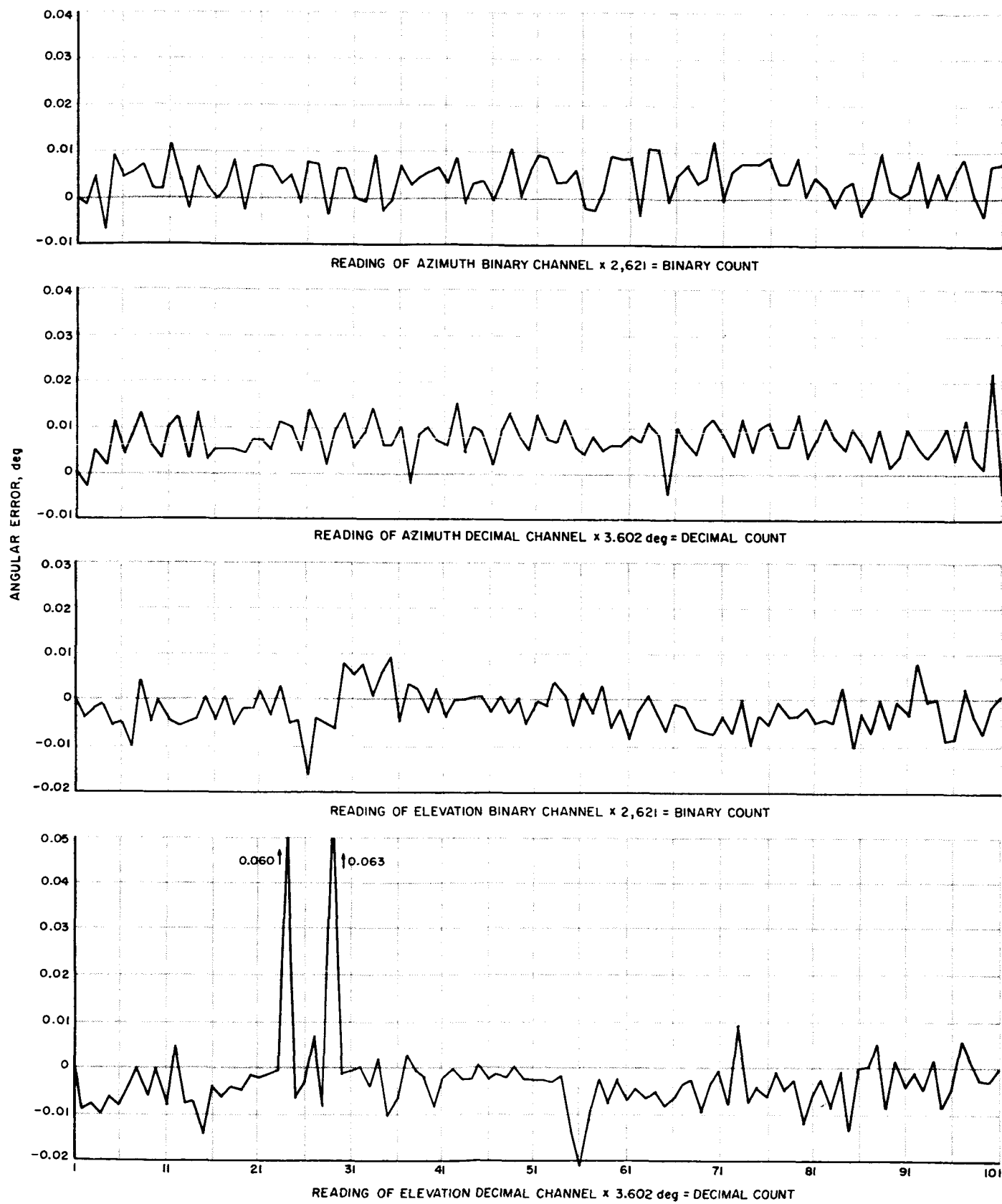


Figure 3. Angular error vs encoder output setting

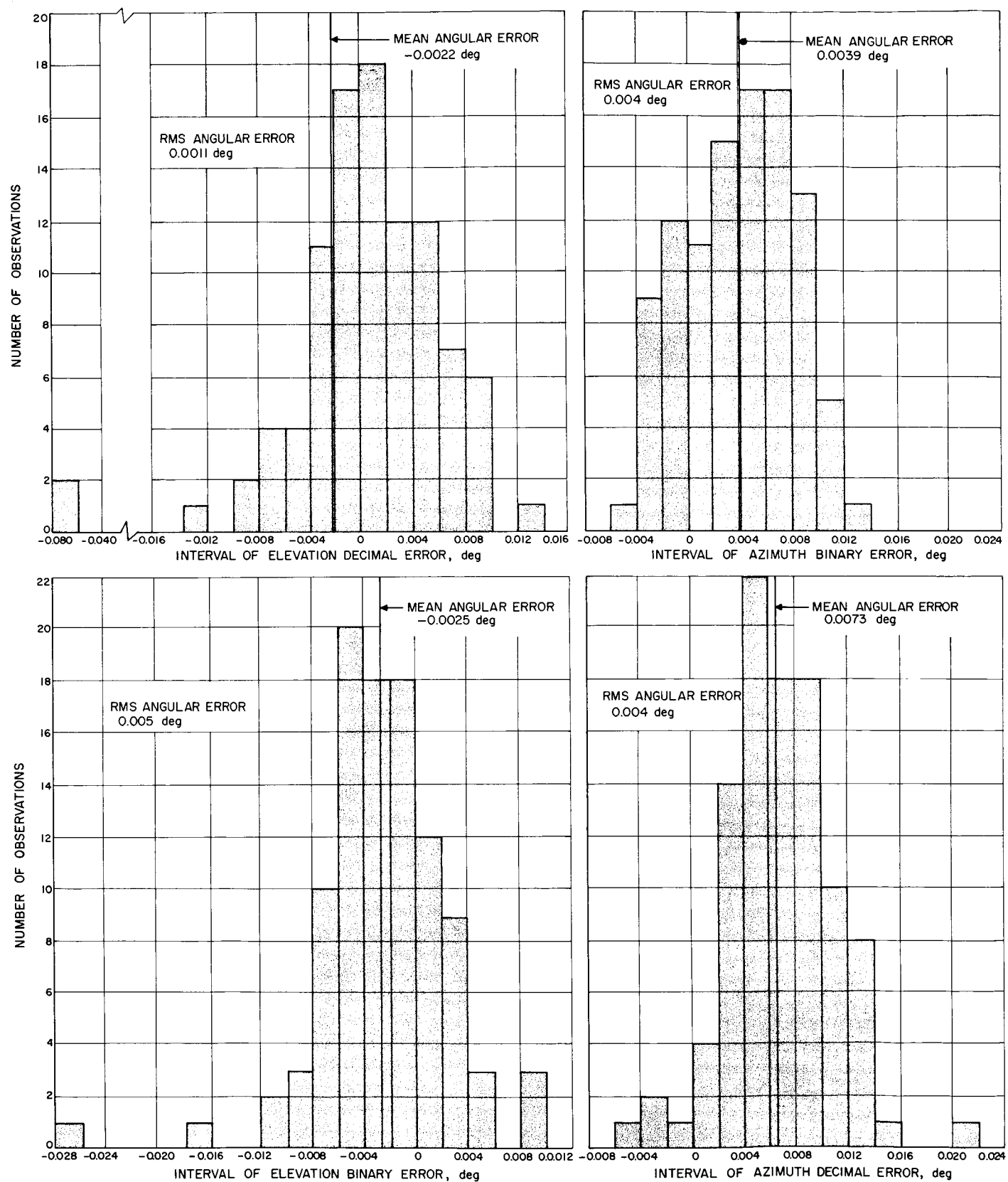


Figure 4. Distribution of angular errors of encoding system

B. Goldstone Transmitter Site

1. Transmitter Antenna Feeds

The primary feeds and transmission lines to be supplied by the Rantec Corporation for the new 85-foot transmitting antenna were described briefly in *Research Summary No. 36-1, Vol I.* At the present time, the 2200-to-2400-mc waveguide and the circularly polarized feed horn have been installed (Fig 5) and partially tested. The 3½-inch coaxial line for the 875-to-975-mc system has been partially installed and the mounting of the horn for this system has been tested. The installation of the collimation tower antennas and transmission lines has been completed. In addition, a 6-foot reflector has been mounted on the side of the 85-foot reflector and will be used as a standard antenna for antenna gain measurements.

Most of the initial tests were performed at 2388/2390 mc; some of the results are presented in Table 1. Each of the antenna feeds to be used for transmitting purposes will provide a single pencil beam. The coarse pattern measurements accomplished at present show that the 3-db beamwidths using the circularly polarized feed are an average of 0.34 degree at 2390 mc. The sidelobe levels in the azimuth and elevation planes are more than 24 db below the peak of the main beam. These results are very satisfactory.

In addition, the waveguide and circularly polarized feed system has been operated several times at 2388 mc

Table 1. Transmitter 2388/2390-mc system with circularly polarized feed

Characteristic	Value
Beamwidths, deg (avg)	0.34
Ellipticity on-axis, db	1.2
Highest sidelobe, db	-24
VSWR of transmission line and feed at 2388/2390 mc	1.20

at the designed high power level of 10 kilowatts. During these operations, the waveguide was pressurized at about 2 psi above atmospheric with dry nitrogen. The high power operations were all satisfactory. Also, the amount of reflected power from the transmission line, measured at the klystron output, was suitably low.

2. Transmitter RF Safety Tests

The operation of an 85-foot transmitting antenna radiating 10 kw of average power requires certain safety precautions against RF radiation hazards to personnel. The most generally known hazard is that produced by the conversion of RF energy into heat energy as it penetrates the body.

A safety level for maximum exposure of personnel has been set by the Air Force and Navy at an incident power flux density of 10 mw/cm². The Bell Telephone Laboratories, however, has chosen 1 mw/cm² as a safe power density. These values were arbitrarily chosen to include a safety factor above any power density known to have produced biological damage. Although it is



Figure 5. Transmitting antenna feed

expected that either safety level would provide adequate protection for continuous exposure under normal conditions, it is necessary to test all working areas to determine the actual power density.

At Goldstone, a testing program has been underway since the initial operation at high power to determine any unsafe areas for personnel. All normal working areas in the vicinity of the antenna have been tested and found safe. The main beam peak power density of the antenna has not been tested yet and, at present, is presumed to be hazardous in the near field region. Calculations of the expected power densities and the measured power densities will be presented when the testing program is completed.

Power densities were measured with portable microwave power bridges and broad beamwidth antennas consisting of a dipole over a groundplane. A directional antenna is normally undesirable since the measurement should determine the total of the incident and all reflected power at a particular location. Some of the measured data is presented in Table 2 for a radiated power of 10 kw (CW) at 2388 mc.

3. VHF Wideband Power Amplifiers

A study has been initiated for the purpose of comparing transistorized and vacuum tube power amplifiers in the VHF range. Recently, VHF transistors have become available which have a high gain-bandwidth product and a 200-mw or more power output capability. One application for wideband VHF power amplifiers is in the design of crystal-controlled frequency multiplier chains for UHF transmitters which are phase-modulated at VHF with a wide bandwidth modulation signal. The comparison has

been made between one of the new silicon triode transistors, the 2N707, and two power amplifier tubes, the subminiature 5703 and the coaxial GL-6771. These three devices are shown in Figure 6.

A single-stage power amplifier operating between 50-ohm impedances was assembled for each device with the gain, bandwidth, and impedance matching optimized for each circuit. The tubes were operated grounded-grid, and the transistor, common-base. At a transistor case temperature of 100°C, the 2N707 has a dissipation rating of 0.5 watt. The efficiency as a 160-mc power amplifier is 30%. As an adequate heat sink was not used, comparisons were limited to power outputs of not greater than 200 mw. The performance figures for the three amplifier configurations are shown in Figure 7. The 2N707 is seen to have a gain-bandwidth product of approximately 140 mc, almost three times that of the 5703 subminiature tube, and 50% greater than the high-transconductance GL-6771 tube.

Using the measured gain-bandwidth information from Figure 7, data for a typical multistage VHF amplifier, with an overall gain of 20 db and a maximum bandwidth, has been calculated for each amplifier type. The expected performance figures for the three amplifier configurations are presented in Table 3. A synchronously tuned cascaded amplifier was assumed with a single tuned circuit per amplifier stage. Table 3 illustrates that for wide-band applications the 5703 is limited to bandwidths of approximately 12 mc. Higher bandwidths (19 mc) may be obtained using a higher gm tube such as the coaxially constructed GL-6771. The 2N707 transistor, however, exceeds the performance of either tube with an expected bandwidth of 28 mc, and in addition it has the advantages

Table 2. Transmitter antenna maximum 2388-mc power densities for 10 kw radiated

Test location	Antenna pointing direction	
	Zenith	Horizon
Above surface of reflector (near trap door to electronics cage), mw/cm ²	5 to 6	5 to 6 (6.6 = maximum predicted)
Slightly in front of lower edge of reflector, mw/cm ²	—	0.6 to 0.8 (1 = maximum predicted from primary feed taper)
Maximum anywhere on ground (but not near beam axis), mw/cm ²	0.1	0.8
Maximum anywhere on ground behind reflector surface, mw/cm ²	—	0.2
Maximum on ground more than 50 ft behind reflector, mw/cm ²	—	0.1

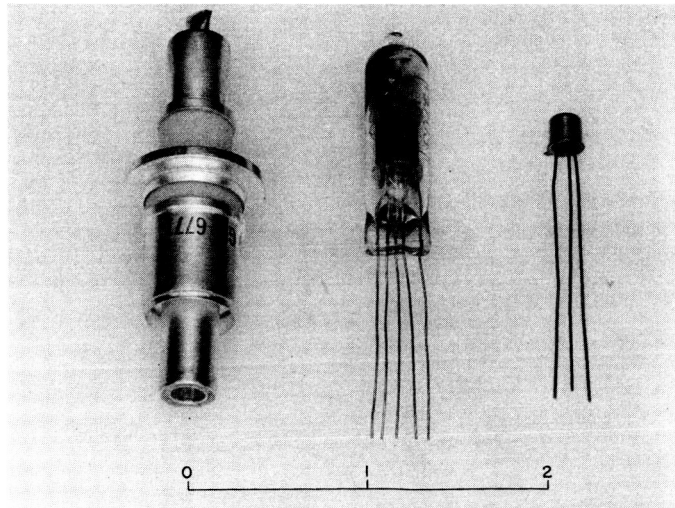


Figure 6. Vacuum tubes GL-6771 and 5703 and transistor 2N707

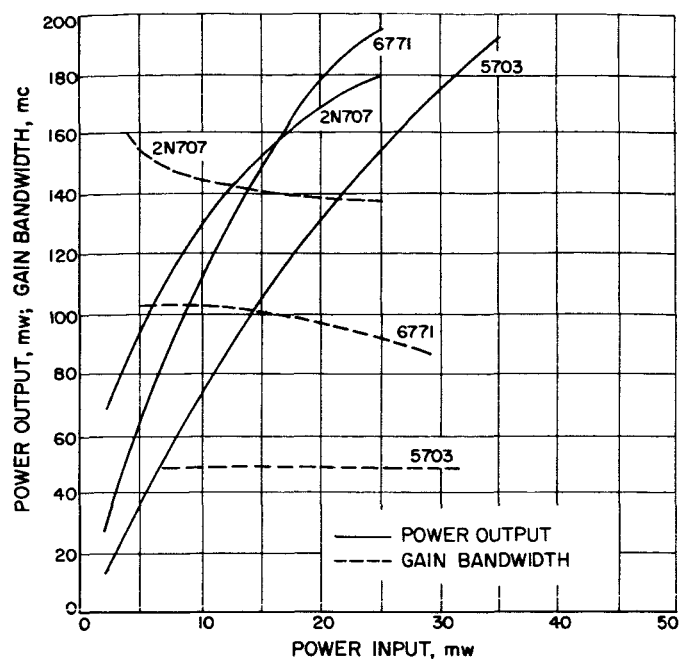


Figure 7. Single-stage 160-mc power amplifiers, comparing vacuum tubes and transistor

of greatly simplified circuit construction and economy of dc power. A two-stage 160-mc amplifier is being developed and tested using the 2N707 transistor, and the actual performance will be reported in a later *Summary*.

Table 3. Comparison of transistors and vacuum tubes in a 160-mc power amplifier

Characteristic	Vacuum tubes		Transistors
	Type 5703	Type GL-6771	Type 2N707
Amplifier gain, db	20	20	20
Power output, mw	200	200	200
Number of stages	4	2	2
GB factor per stage, mc	48	95	140
Bandwidth per stage, mc	27	30	44
Bandwidth shrinkage factor	0.44	0.64	0.64
Amplifier bandwidth, mc	12	19	28
Total dc power input, watts	12	12	1.0

C. Goldstone Receiver Site

1. Low-Noise 960-mc Receiver

A low-noise 960-mc receiver incorporating a parametric up-converter has been developed at the Jet Propulsion

Laboratory and installed at the Goldstone receiver station. The installation was described in detail in *Space Programs Summary No. 6*, Section III. In typical operation of the parametric up-converter, an overall noise figure of 2.3 db has been obtained with an up-conversion gain of 25 db and a bandwidth of 0.4 mc.

The low-noise receiver has been used in conjunction with the Project Echo Moon-bounce experiments between Holmdel, N. J. and the Goldstone tracking station on 24 and 25 November 1959, 6 January and 9 February 1960. The experience gained during these tests indicated that the parametric amplifier exhibited a significant amount of detuning and change in gain during the test and calibration. Figure 8 shows the overall receiver signal level vs AGC voltage characteristic measured at various times during the 9 February Moon-bounce experiment. It may be noted that the gain changed by approximately 8 db during the test. It was hypothesized that the effect was due to the ambient temperature change over the 12 to 15 hours of test and calibration, and an investigation of a temperature regulation scheme for the parametric up-converter was begun to check the hypothesis.

A temperature regulating device was developed and installed at the Goldstone site. The temperature regulator comprises a small aluminum box containing three resistive heating elements, a thermostat and arc-suppressing capacitor operating directly from the 110-volt-ac power

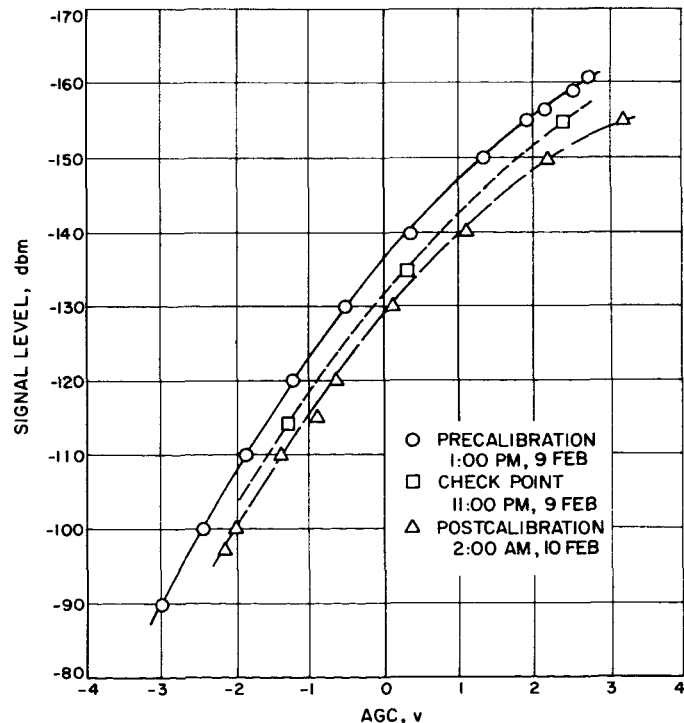


Figure 8. Low-noise 960-mc receiver sensitivity before temperature regulation

line. The total dissipation of the heating elements is 50 watts. Figure 9 is a photograph of the heater box with cover plate removed. The box has been bolted to the parametric up-converter waveguide with the critical portion of the circuit insulated with blocks of styrofoam. In order to minimize conductive heat loss to noncritical portions of the circuit, mica separation windows have been placed in the pump waveguide choke flange joints, and the critical waveguide parts are mechanically supported by a Micarta insulating clamp. A photograph of the installation is shown in Figure 10.

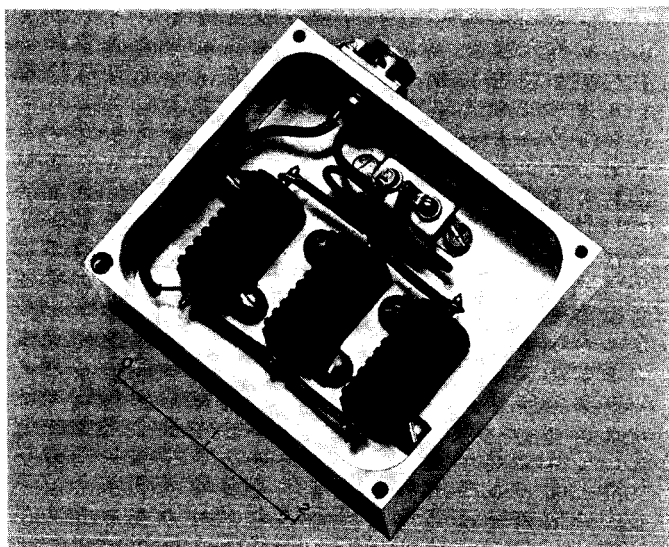


Figure 9. Heater box for low-noise 960-mc receiver

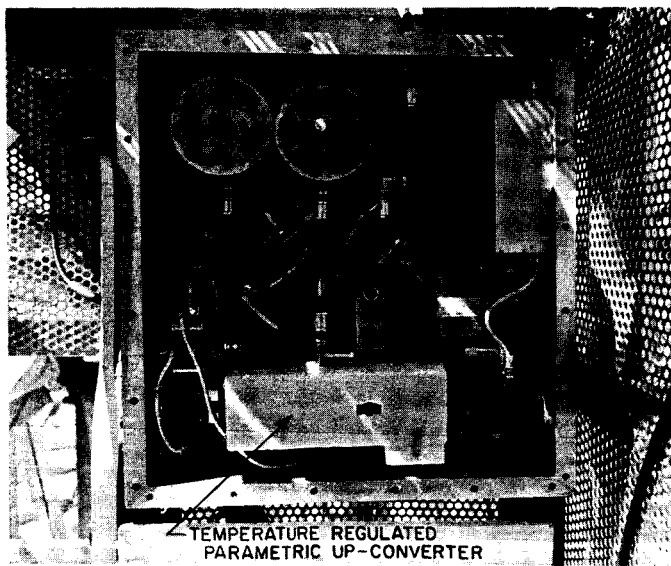


Figure 10. Low-noise 960-mc parametric amplifier with temperature regulating device

Prior to installation of the heater on the Goldstone receiver, temperature tests were conducted in a temperature box using a mockup of the up-converter. The temperature of the varactor mount was maintained between 90 and 100°F for an ambient temperature range of 30 to 90°F.

Closed-path gain curves were taken using the low-noise parametric up-converter following installation of the temperature stabilization equipment at Goldstone. The low-noise receiver was operated from a period early in the afternoon of 16 March 1960 (ambient temperature approximately 65°F) until 11:00 pm that evening (ambient temperature approximately 45°F). The noise figure of the receiver was 2.6 db at 2:30 pm. The gain characteristic is shown in Figure 11. At 11:00 pm, the noise figure was 2.7 db and the gain characteristic was as shown in Figure 11. It will be noted that the change in gain is less than 1 db. No significant detuning of the 960-mc parametric amplifier was observed during the period of test.

The temperature regulator installed as part of the 960-mc low-noise receiver at Goldstone tracking station has provided a significant improvement in the tuning and gain stability of the parametric up-converter. Further evaluation of the 960-mc low-noise parametric amplifier will be made in later Moon-bounce tests.

2. Stable Crystal Oscillator

Since improved oscillator stability can increase sensitivity in a phase coherent receiving system by permit-

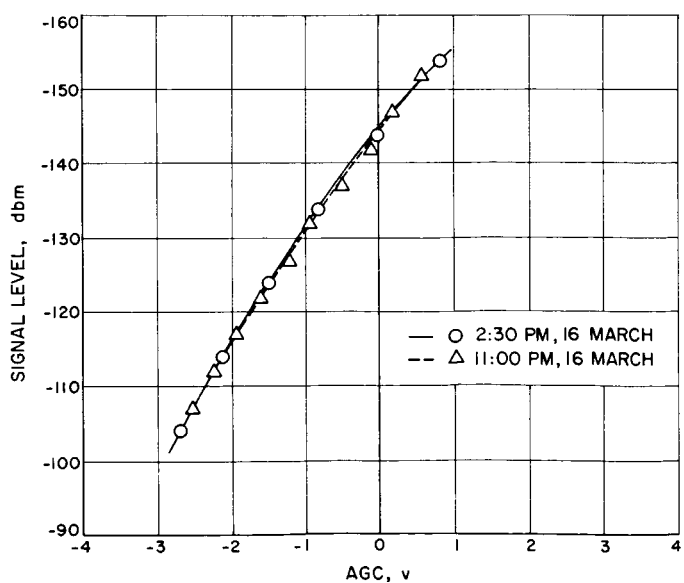


Figure 11. Low-noise 960-mc receiver sensitivity after temperature regulation

line. The total dissipation of the heating elements is 50 watts. Figure 9 is a photograph of the heater box with cover plate removed. The box has been bolted to the parametric up-converter waveguide with the critical portion of the circuit insulated with blocks of styrofoam. In order to minimize conductive heat loss to noncritical portions of the circuit, mica separation windows have been placed in the pump waveguide choke flange joints, and the critical waveguide parts are mechanically supported by a Micarta insulating clamp. A photograph of the installation is shown in Figure 10.

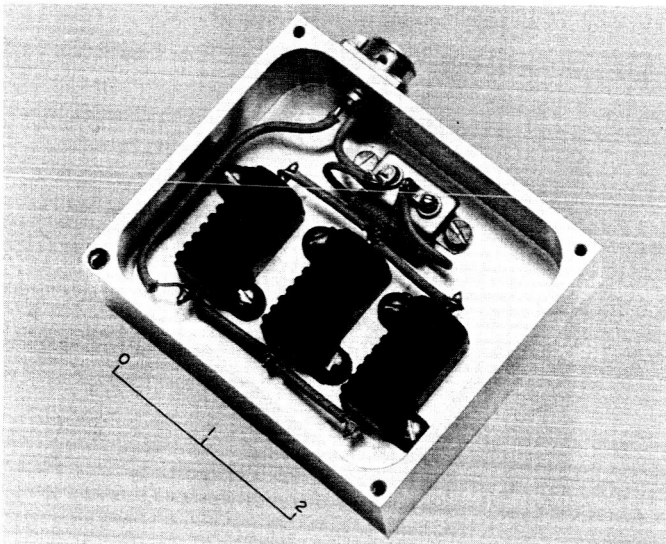


Figure 9. Heater box for low-noise 960-mc receiver

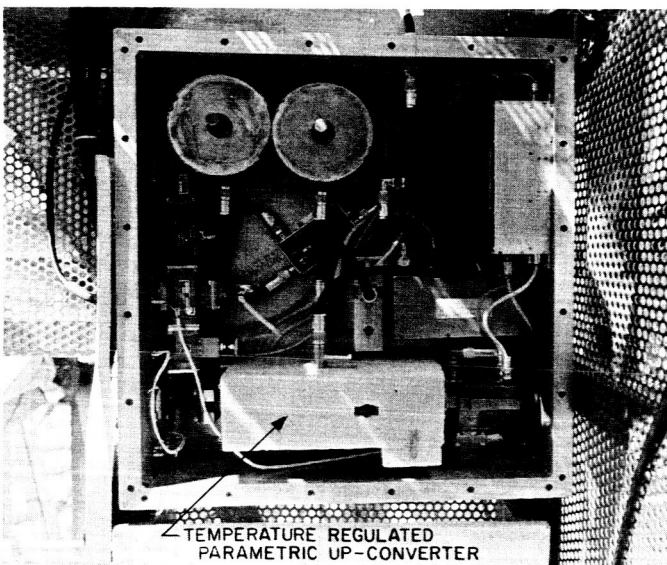


Figure 10. Low-noise 960-mc parametric amplifier with temperature regulating device

Prior to installation of the heater on the Goldstone receiver, temperature tests were conducted in a temperature box using a mockup of the up-converter. The temperature of the varactor mount was maintained between 90 and 100°F for an ambient temperature range of 30 to 90°F.

Closed-path gain curves were taken using the low-noise parametric up-converter following installation of the temperature stabilization equipment at Goldstone. The low-noise receiver was operated from a period early in the afternoon of 16 March 1960 (ambient temperature approximately 65°F) until 11:00 pm that evening (ambient temperature approximately 45°F). The noise figure of the receiver was 2.6 db at 2:30 pm. The gain characteristic is shown in Figure 11. At 11:00 pm, the noise figure was 2.7 db and the gain characteristic was as shown in Figure 11. It will be noted that the change in gain is less than 1 db. No significant detuning of the 960-mc parametric amplifier was observed during the period of test.

The temperature regulator installed as part of the 960-mc low-noise receiver at Goldstone tracking station has provided a significant improvement in the tuning and gain stability of the parametric up-converter. Further evaluation of the 960-mc low-noise parametric amplifier will be made in later Moon-bounce tests.

2. Stable Crystal Oscillator

Since improved oscillator stability can increase sensitivity in a phase coherent receiving system by permit-

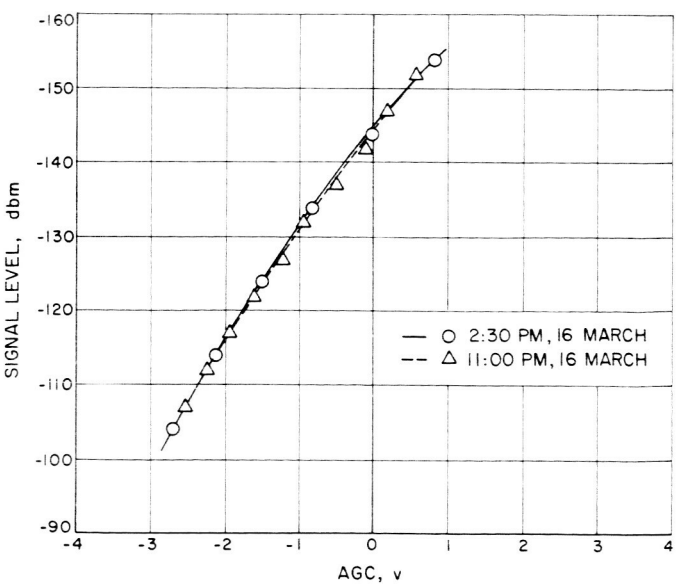


Figure 11. Low-noise 960-mc receiver sensitivity after temperature regulation

ting operation at reduced bandwidths, a continuing research effort has been initiated to develop techniques for generating phase stable sinusoidal signals. One result of this effort has been the development of phase stable solid-state voltage-controlled crystal oscillators (VCO) which have been described in earlier reports (*SPS 4*, pp 69-73, and *SPS 5*, pp 59-61). In the initial investigation of the solid-state VCO, considerable attention was given to the mechanical and electrical design problem to provide good phase stability. In this report, attention is directed toward the problem of thermal stabilization with the aim of greatly reducing variations in average frequency, oscillator control characteristics, and power output with ambient temperature change.

Temperature stabilization of the solid state crystal oscillator has been accomplished in the investigation described herein through use of a relatively simple change-of-state crystal oven. This crystal oven (manufactured by Robertshaw-Fulton Co.) operates in the following manner. Contraction and expansion of a salt (paradichloralbenzine) with a relatively high melting point is transmitted through a diaphragm to a carbon pile that controls heater power to the unit. Power flow to the unit is a continuous function of the thermal requirements for maintaining the salt at a constant temperature; thus there are no switching transients. The specified temperature stability is $\pm 0.0065^{\circ}\text{C}/^{\circ}\text{C}$ ambient. Three oven operating temperatures are available (53, 70, and 87°C) which are established by the composition of the salt. A 53°C operating temperature was chosen for this investigation.

The principal factors which cause variation in performance of the transistorized VCO with ambient temperature change are the frequency vs temperature characteristic of the crystal and the capacity vs temperature characteristic of the capacitive control diode. Additional factors which affect oscillator performance are changes in transistor characteristics, zener diode characteristics

(voltage regulation), and inductance (oscillator tuned circuit) with temperature. In light of these considerations, insertion of all the oscillator components into the oven should provide nearly complete thermal stabilization of the VCO. The low dc power requirements of the transistorized VCO make this possible. Figure 12 shows the transistorized VCO and the change-of-state oven.

In order to maintain the thermal stability of the oven with the VCO circuit inserted, the following steps were taken. (1) The total dc power input to the oscillator was reduced in order to minimize the thermal contribution of the internal heat source. (2) The RF dc and error-control input connections to the oscillator were thermally isolated by using long 22-gage interconnecting wires to the interior of the oven. (3) The mounting structure for the transistorized oscillator was a compromise between a small mass for low thermal inertia and a mass large enough for adequate structural strength.

After taking these precautions, the temperature stability of the oven with the VCO unit inserted checked at $0.006^{\circ}\text{C}/^{\circ}\text{C}$, which approximates the stability figure claimed by the manufacturer. Hence the regulating capability of the oven was not significantly disturbed by the added electronic components. The total dc power requirements of the solid state unit is 300 mw. The input power to the oven varies from 0.5 to 3 watts over a temperature range of 0 to 50°C .

The frequency stability of a 31.0017-mc VCO without temperature control is indicated in Figure 13. Between 0 and 20°C , the frequency variation is of the order of 3 parts in $10^6/^{\circ}\text{C}$. The frequency change with temperature is largely a function of the quartz crystal. The corresponding change in the VCO control characteristics as a function of temperature is shown in Figure 14. This change in slope is mostly due to the capacity-vs-temperature characteristics of the control diode and is about $\pm 20\%$ over the temperature range indicated.

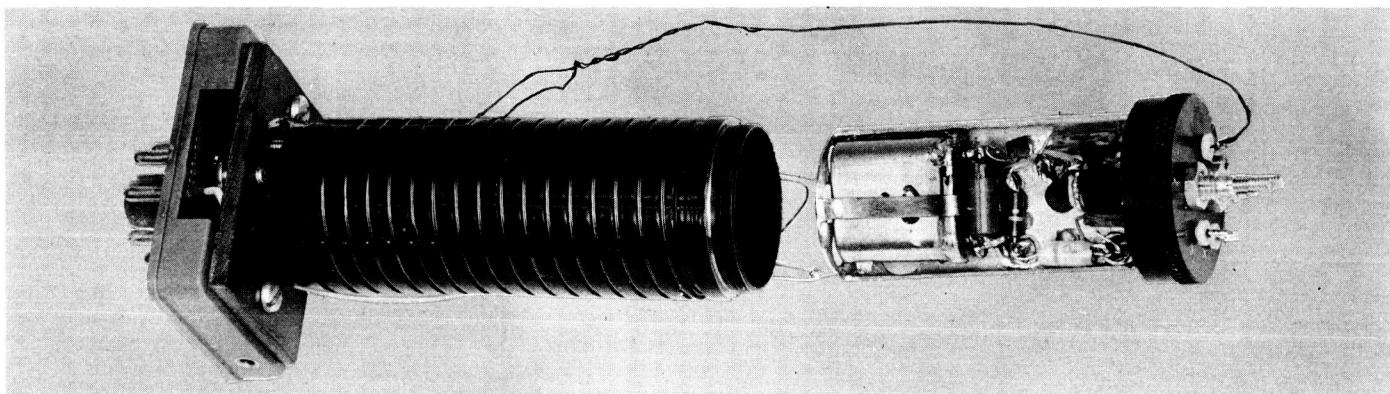


Figure 12. Transistorized VCO and change-of-state oven

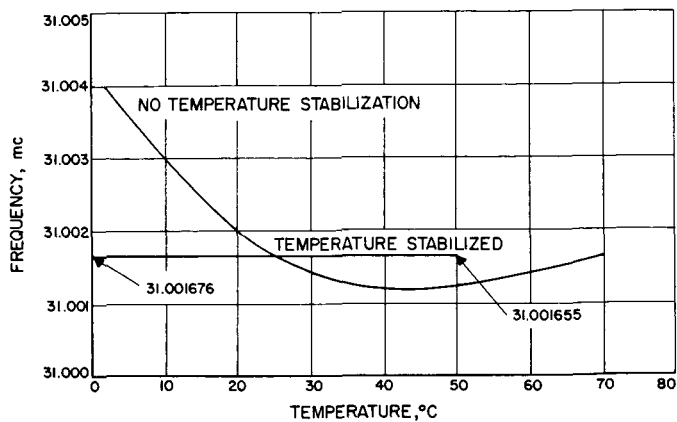


Figure 13. Frequency-vs-temperature characteristics of 31.0017-mc VCO in and out of change-of-state oven

With the VCO inserted into the oven, the frequency stability was improved to approximately 1 part in $10^8/\text{°C}$ over the temperature range indicated in Figure 12. The stability of the Collins 40K-1 frequency standard used to check this performance is rated at better than 1 part in $10^9/\text{hour}$, and the duration of the test was approximately 2 hours. The corresponding variations in the VCO control slope are shown in Figure 15 and can be seen to be less than $\pm 1\%$. Fast or slow changes in ambient temperature, $10^\circ\text{C}/\text{min}$ to $1^\circ\text{C}/\text{min}$, indicated that the oven

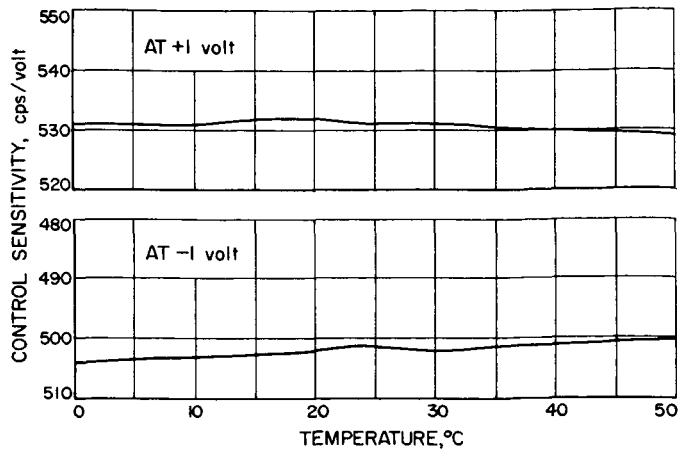


Figure 15. Control characteristics of 31.0017-mc VCO in change-of-state oven

was substantially free from thermal transients as checked by oscillator frequency readings.

The mechanical construction of the oven appears adequate for use in a ground station environment. Ruggedized ovens that will take shock and vibration may be obtained from the manufacturer under special contract.

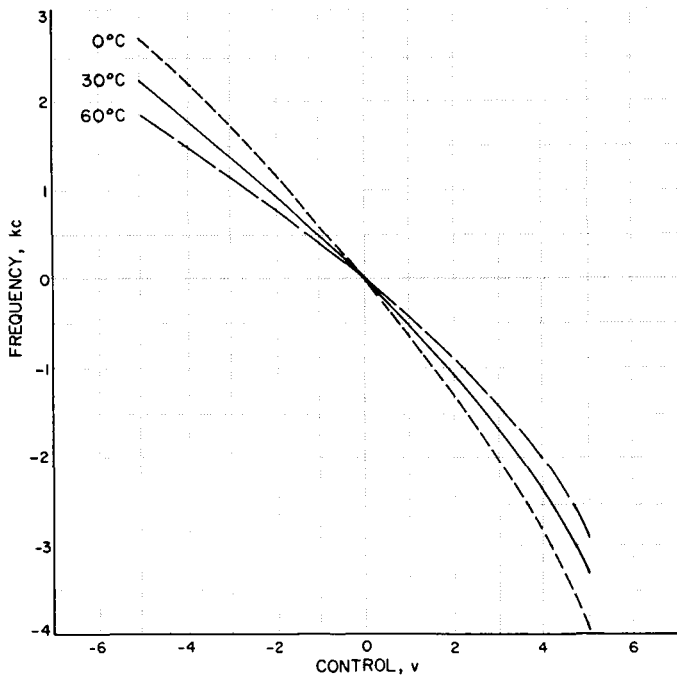


Figure 14. Control characteristics vs temperature of 31.0017-mc VCO

D. Mobile Tracking Stations

1. Mobile Checkout RF VCO

The RF voltage-controlled oscillators (VCO) used in the *Ranger* mobile downrange and launch checkout stations must possess S-curves sufficiently large to track the two-way doppler shift. This corresponds to frequency variations of approximately 1 part in 10^4 for the downrange stations and 7 parts in 10^5 for the launch station.

The 31-mc VCO used for tracking the deep space probes, *Pioneers III* and *IV*, possessed all the desirable characteristics (*JBS 9*) with the exception of the available frequency swing. This VCO was subsequently modified to meet the two-way doppler requirements by (1) incorporating a -150 -volt power supply through a high impedance to the cathode of the reactance modulator, thus obtaining a larger and a more linear S-curve; and (2) reducing the crystal phase slope by operating the crystal 1 part in 10^4 below its series resonant frequency. Figure 16 is a schematic diagram of the completed VCO.

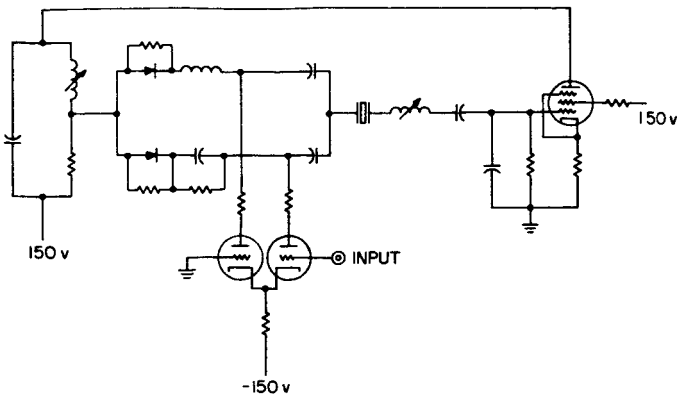


Figure 16. Mobile checkout RF VCO

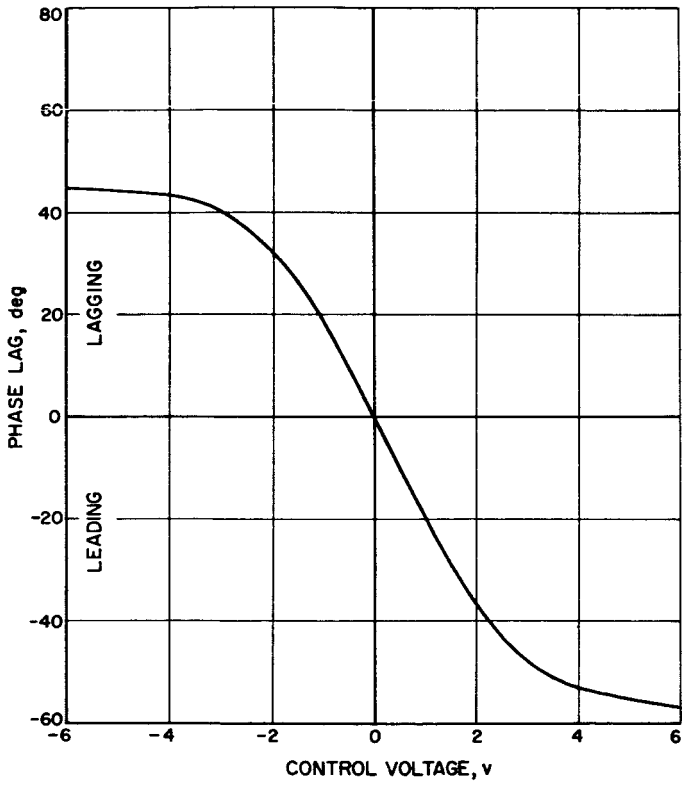


Figure 17. Reactance modulator phase

Figure 17 shows the open-loop phase deviation vs control voltage produced by the reactance modulator. Figure 18 shows both the measured closed-loop S-curve and the open-loop measurement. The open-loop data was obtained with the oscillator operating as an amplifier as shown in Figure 19. The external oscillator frequency was varied, thus producing a phase shift through the crystal. An equal and opposite phase error was introduced in the amplifier by applying a compensating dc voltage to the reactance modulator. The two curves in Figure 18

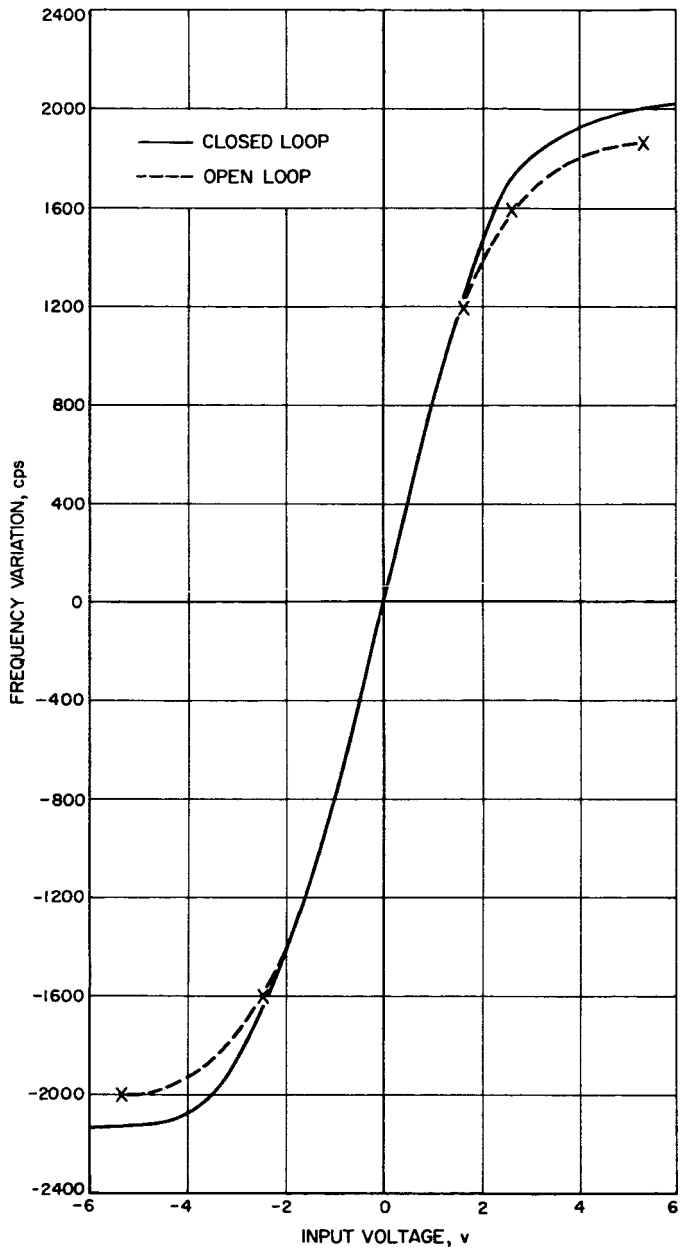


Figure 18. VCO closed-loop and open-loop S-curves

indicate that the VCO characteristics are predictable from open-loop measurements.

The RF VCO was tested using a receiver with a 20-cps bandwidth, and the phase error was measured to be 4 degrees peak as compared to 2.5 degrees for the previous design. This reduction in phase stability will result in less than 0.5-db loss in receiver sensitivity. The redesigned RF VCO is considered satisfactory to meet all the requirements of the mobile launch and downrange stations.

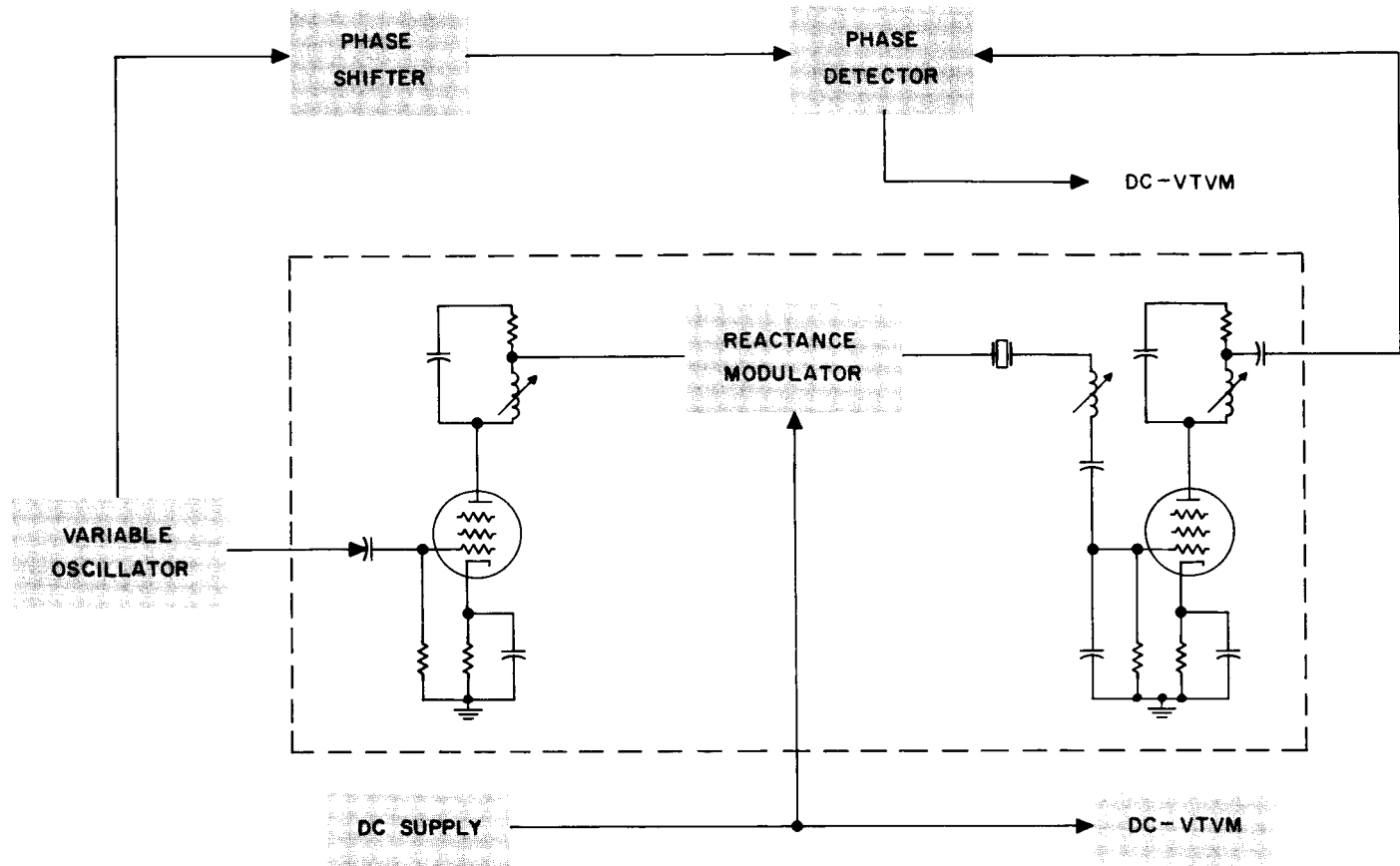


Figure 19. Open-loop phase measurement

II. SPACECRAFT COMMUNICATIONS

A. Communications System Components

The communications system for the first *Ranger* spacecraft will consist of a 250-mw transmitter and a 3-watt transponder. The 250-mw transmitter will telemeter spacecraft engineering and scientific measurements and may be used to provide tracking data with respect to two angles and one-way doppler. The high-power transponder will provide two-way doppler in addition to the angular information, receive commands from the Earth, and also telemeter engineering and scientific data to a significantly greater range.

1. Transponder

In July 1959, a contract was awarded to Motorola Western Military Electronics Center, Phoenix, Arizona, to develop the phase coherent transponder system. The design objective was to develop a transponder with maximum long term reliability, minimum power consumption and minimum weight consistent with the desired electrical performance. The first Motorola production model was delivered on 25 February 1960 and is presently undergoing evaluation tests.

Figure 20 shows a functional block diagram of the transponder. It is noted that the unit consists basically of a double superheterodyne crystal controlled phase coherent receiver and a 960-mc transmitter. Figure 21 shows the top, side, and bottom views of the transponder. The entire circuitry, with the exception of the two UHF tube cavity amplifiers, is contained within this structure. Transistor and solid state devices are used throughout. It may be noted that the mechanical design consists of a casting containing 12 separate shielded compartments. Each compartment contains a module such as a 50-mc IF amplifier, a 10-mc IF amplifier, a phase detector, and a VCO. This technique was used primarily to insure adequate RF isolation between the highly sensitive circuits. All circuits within the compartments are mounted on a removable plate. Therefore, if a component failure occurs, the faulty module can be replaced quickly and easily. Another important feature of this particular mechanical packaging is its vibrational characteristics. Experimental vibrational data indicates that the structure is free of resonances from 20 cps to almost 740 cps. At 740 cps, where the first resonance occurred, the displacement should be small enough to produce a negligible effect on the transponder performance.

Table 4 is a brief list of transponder characteristics. The evaluation program is presently being conducted to ascertain the extent to which it meets the required specifications.

2. UHF Cavity Amplifiers

The spacecraft transponder system for the *Ranger RA-1* includes two cascaded 960-mc cavity amplifiers. The first UHF amplifier increases the transponder 5-mw output to 250 mw, which the second cavity in turn amplifies to 3

watts. The 3-watt signal is then fed directly to the transmitting antenna mounted on the spacecraft.

Three prototype cavities have been fabricated at the Laboratory for test and evaluation. Electrical and environmental characteristics of the 250-mw driver amplifier

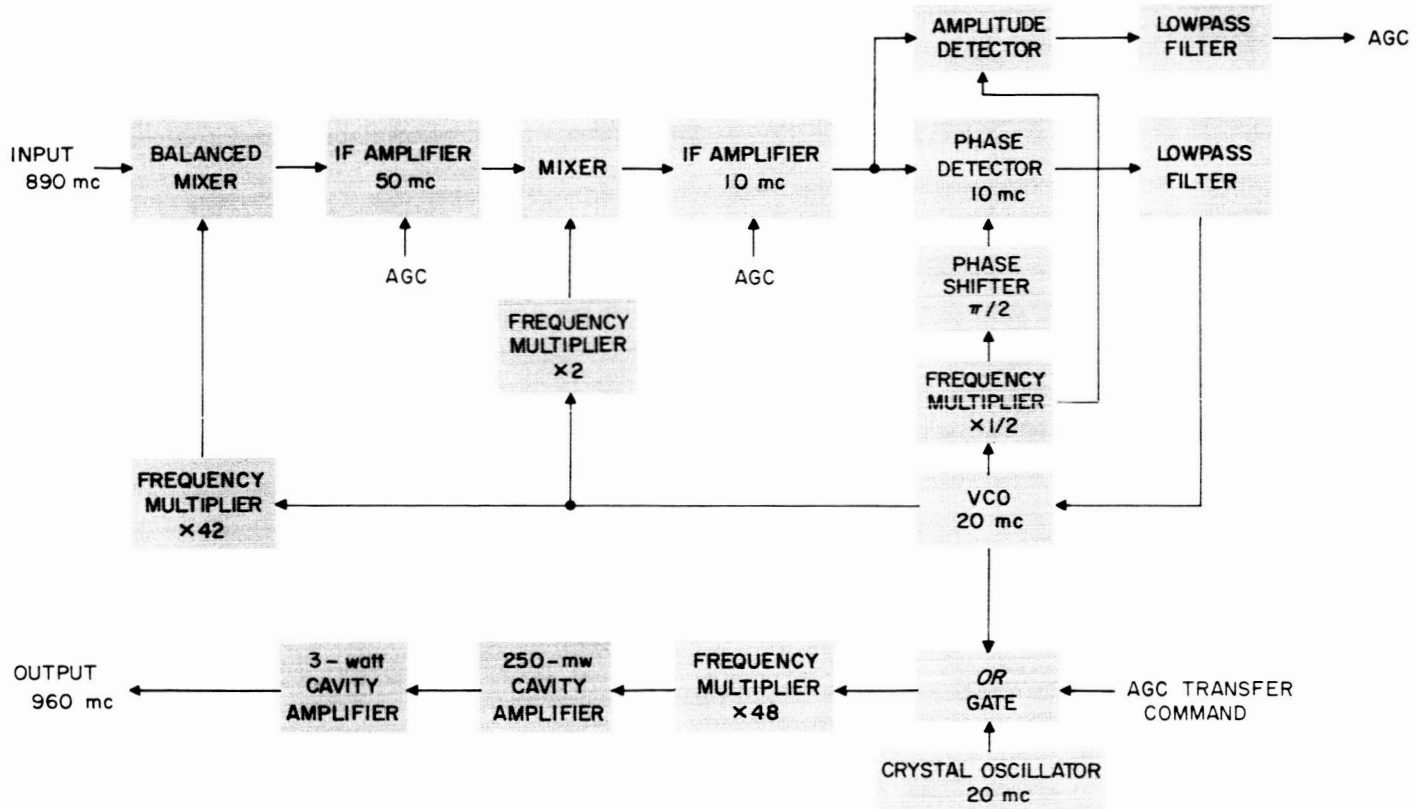


Figure 20. Ranger spacecraft 890/960-mc transponder functional diagram

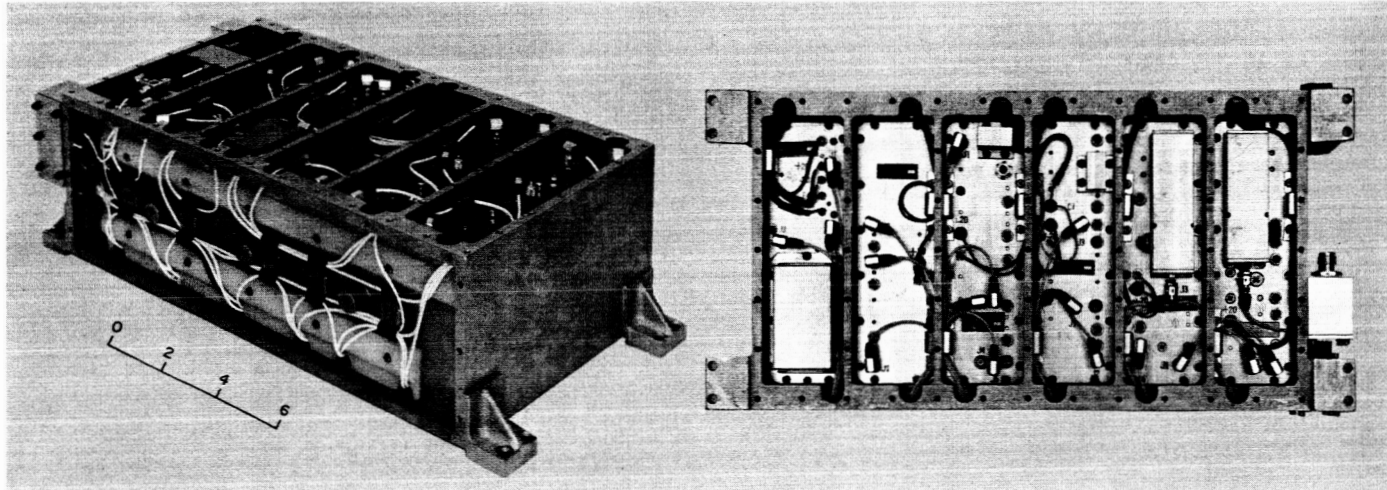


Figure 21. Views of 890/960-mc Mark I transponder

Table 4. Ranger spacecraft transponder characteristics

Characteristic	Value
Receiver input frequency, mc (nominal)	890.046
Receiver noise figure*, db	15
Receiver noise bandwidth ($2B_L$), cps	100
Receiver threshold*, dbm	-139
Receiver AGC loop noise bandwidth ($2B_L$), cps	1
Receiver AGC threshold, dbm	-159
Transmitter frequency, mc (nominal)	960.05
Transmitter power, dbm	+34.7
Transmitter modulation response, mc	0 to 5

*Measured at diplexer input terminal.

were reported previously in SPS 37-1. This unit has successfully met all phases of its design requirements with the possible exception of its thermal characteristics. Temperature compensation methods, now under consideration, are expected to provide improved performance. The 3-watt amplifier is mechanically identical to the 250-mw unit, and is electrically identical with the exception of the bias and supply voltage requirements.

The electrical characteristics of the 3-watt amplifier are shown in Table 5. As expected, the operating efficiency of this unit (38%) is considerably greater than that of the 250-mw driver stage (6%). This is due in part to operating the tube closer to its optimum design power level but mainly to the larger ratio of RF to filament power at this level of output. Additionally, greater bandwidth was obtained in the higher-powered unit. This results from the naturally lower plate impedance loading the output

cavity more heavily than in the small power case. The RF power output vs RF power input of the 3-watt amplifier is given in Figure 22. It will be noted that the unit is operated near saturation for optimum power stability, where a ± 1.0 -db variation in RF input power results in less than ± 0.25 -db change in the output power. Thermal data on the unit is graphed in Figure 23 and indicates a 2-db variation in output power over the temperature range (-10 to +82°C). Due to the mechanical identity of the two units, the output power-vs-temperature characteristics of the 3-watt amplifier are essentially the same as those of the 250-mw unit. Variations of 2 db are presently allowed in the electrical specifications on these units, assuming no temperature compensation.

The electrical performance of the two units operating in cascade is defined in Table 6. The resultant overall efficiency of 25% represents an acceptable performance for a transmitter subsystem using planar tubes at this frequency and power level. Figure 24 shows the over-

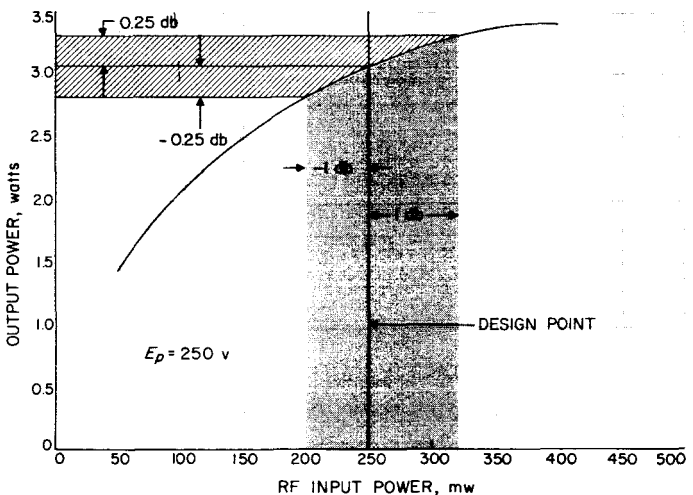


Figure 22. Input-output characteristics D6771-2 cavity amplifier

Table 5. Performance data, D6771-2 cavity amplifier

Characteristic	Value
Power input, watts	0.25
Power output, watts	3.0
Gain, db	10.8
Bandwidth (3 db), mc	13.0
Plate efficiency, %	60.0
Overall efficiency, %	38.0
Input impedance, ohms (nominal)	50.0
Input VSWR	1.5
Output impedance, ohms (nominal)	50.0
Output match ratio	1.05
Plate voltage, volts	250
Plate current, ma	20.0
Filament voltage, volts	4.75
Filament current, amp	0.6
Weight, lb	1.44
Size, in. ³	36

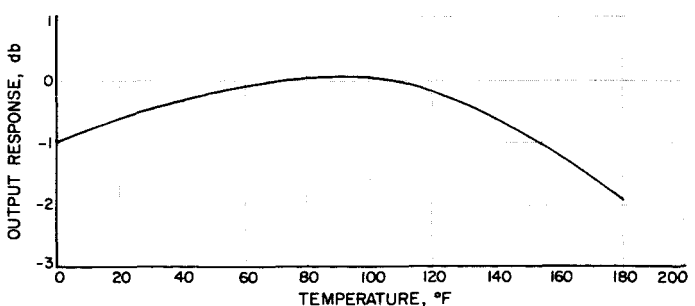


Figure 23. Thermal characteristics D6771-2 cavity amplifier

Table 6. Cascaded performance of the D6771-1 and D6771-2 cavity amplifiers

Function	Driver amplifier	Final amplifier	Total
Plate power dc, watts	1.2	5.0	6.2
Filament power dc, watts	2.85	2.85	5.7
RF drive power 960 mc, watts	0.005	—	0.005
RF output power 960 mc, watts	—	3.0	3.0
Plate efficiency, %	20.8	60.0	48.5
Overall efficiency, %	6.0	38.0	25.2
Input impedance, ohms	50.0	—	50.0
Input VSWR	1.5	—	1.5
Output impedance, ohms	—	50.0	50.0
Output match ratio	—	1.05	1.05
Bandwidth 3 db, mc	8.0	13.2	6.0
Weight, lb	1.44	1.44	2.88
Size, in. ³	36.0	36.0	72.0

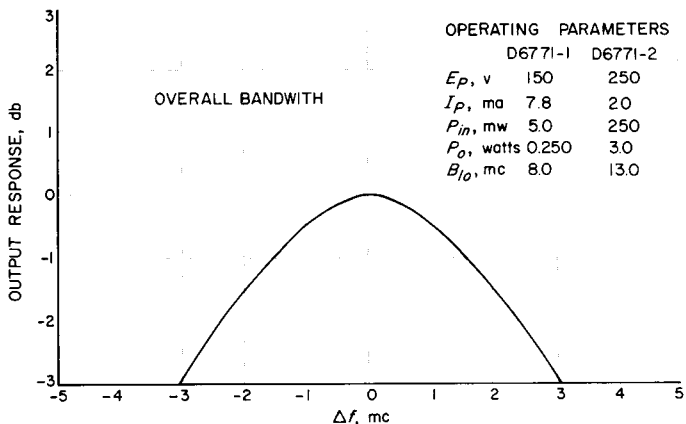


Figure 24. Overall bandwidth D6771-1 and D6771-2 cavity amplifiers

all bandwidth of the two units, measured by phase-modulating the RF signal. A 3-db bandwidth of 6 mc was obtained and is considered adequate in view of the 5-mc system design goal. The input-output characteristics are illustrated in Figure 25 which shows that drive level fluctuations as great as ± 3 db (from the 5-mw design point) will result in an overall output power variation of 0.9 db. The thermal properties of the cascaded units, given in Figure 26, show that variations in output power due to temperature change are similar to those of the individual units. Thermal compensation devices and materials are currently under test and will be incorporated in the cavity design when such techniques prove beneficial.

Invitations to bid on the manufacture of thirty-eight 250-mw and 3.0-watt cavity amplifiers for the *Ranger*

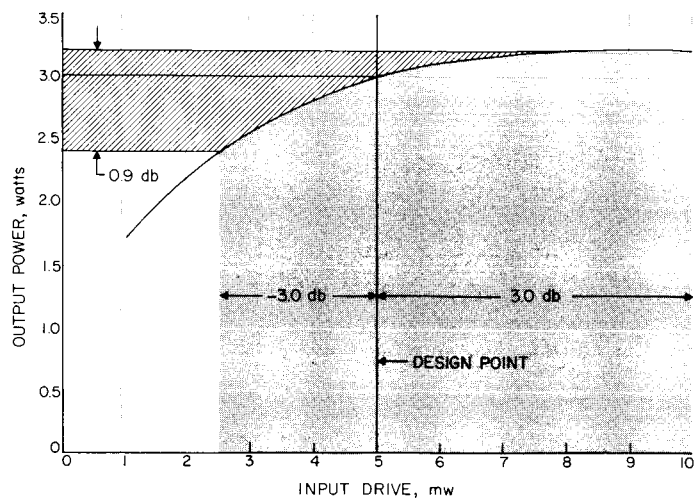


Figure 25. Input-output response cascaded operation D6771-1 and D6771-2 cavity amplifiers

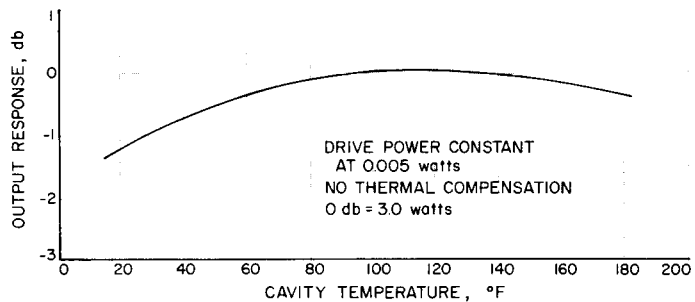


Figure 26. Thermal characteristics cascaded operation D6771-1 and D6771-2 cavity amplifiers

program were submitted to six prospective companies late in February. A manufacturer has been selected and a purchase order is being issued at the present time. It is expected that the first of these units will arrive at the Laboratory early in May.

3. Communications Compartment Packaging

The majority of the *Ranger RA-1* spacecraft instrumentation will be mounted in the electronic equipment compartment. This compartment, as described in SPS 37-1, page 36, consists of six individual cubicles arranged in an annular hexagonal ring.

The design of the radio equipment has progressed to the point where integration into the spacecraft has been considered. The present plan is to mount all the radio frequency subassemblies, with the exception of the transponder power converter and the antenna hardware into one cubicle. A wooden mockup of the RF assembly has been constructed to assist in designing the final configuration. Figure 27a shows the location of the subassem-

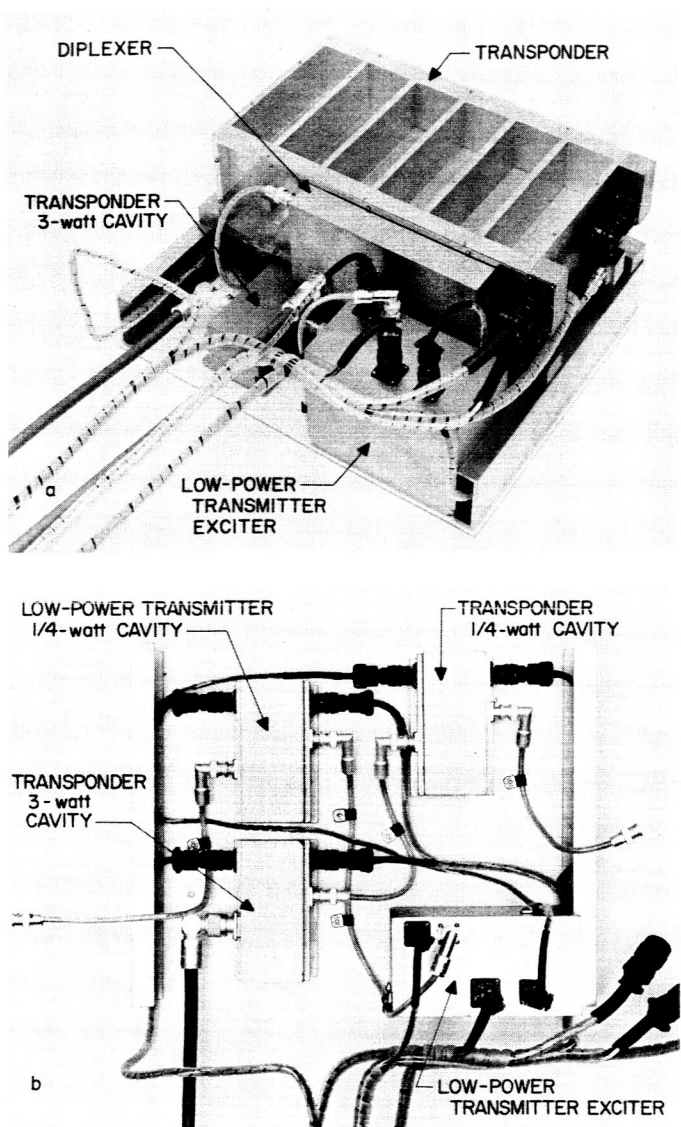


Figure 27. Ranger RF communication assembly

bilities; the transponder was removed in Figure 27b to show the location of otherwise hidden units. The layout is arranged such that the major heat-producing subassemblies, namely the three cavity amplifiers, are mounted firmly to the surface which will radiate out into space. As shown, the transponder is mounted directly above the two 0.25-watt cavities. It is felt that this configuration will tend to minimize the heat disturbance between the various subassemblies.

The mockup as shown was not intended to include every small detail. Instead its intent was to provide information regarding interface problems, subassembly locations, and the cable routing for the final design of the assembly housing.

4. Transponder Test Set

In order to provide a convenient and efficient means for testing and calibrating the spacecraft radio communication equipment, a test set has been designed by the Motorola Western Military Electronics Center to specifications of the Laboratory. The test set (Fig 28) consists of an 890-mc transmitter, a 960-mc receiver, a transponder mount and power supply, and a number of general-purpose test instruments. It is intended to be capable of measuring the following characteristics of the spacecraft communication equipment under static and environmental test conditions: (1) transmitter frequencies, (2) transmitter power output, (3) transmitter phase stability, (4) modulated transmitter output spectral distribution, (5) transponder phase transfer function, (6) receiver threshold sensitivity, (7) receiver automatic gain control response, and (8) receiver phase stability.

The 890-mc test transmitter (Fig 29) provides a test signal for the receiver portion of the Mark I transponder. Means are provided for modulating the amplitude, frequency, or phase of the test signal and for accurately controlling its average power level. The principal design characteristics of the transmitter are summarized in Table 7. As shown in Figure 29 it is assembled in a single instrumentation rack with its power supply and power output monitor.

The 960-mc test receiver (Fig 30) is of the single-conversion superheterodyne type designed for three different modes of operation. In the first mode it is an automatic phase control receiver which may be operated completely independently of the other test set components. In this mode the amplitude and phase detector reference signals are internally generated.

In the second mode it is also an automatic phase control receiver; however, the phase detector reference signal is derived from the precision frequency standard of an electronic frequency counter. With this arrangement the output frequencies of 960-mc transmitters may be conveniently measured by measuring the receiver VCO frequency with the electronic counter when the receiver is synchronized to the transmitter signal.

In the third mode the receiver is operated as a phase detector in conjunction with the test transmitter. Both the phase detector reference and the local oscillator signals are derived from the transmitter VCO signal by means of coherent frequency shifters. With this arrangement the transponder phase transfer function and modulation characteristics may be observed without the distortion introduced when an automatic phase control receiver is used for the measurements.

Table 8 summarizes the principal characteristics of the test receiver, which includes means for both manual and

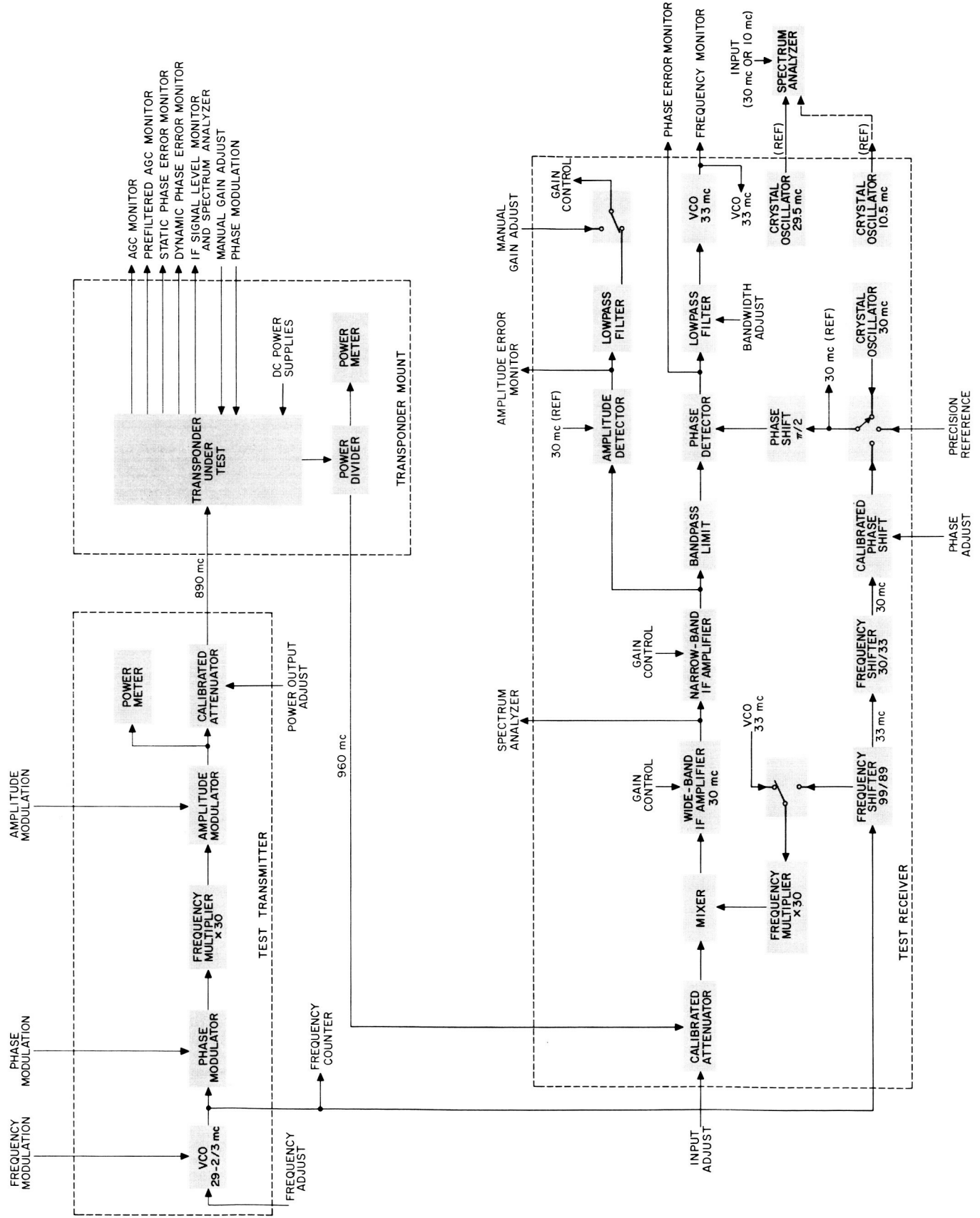


Figure 28. Transponder test set functional diagram

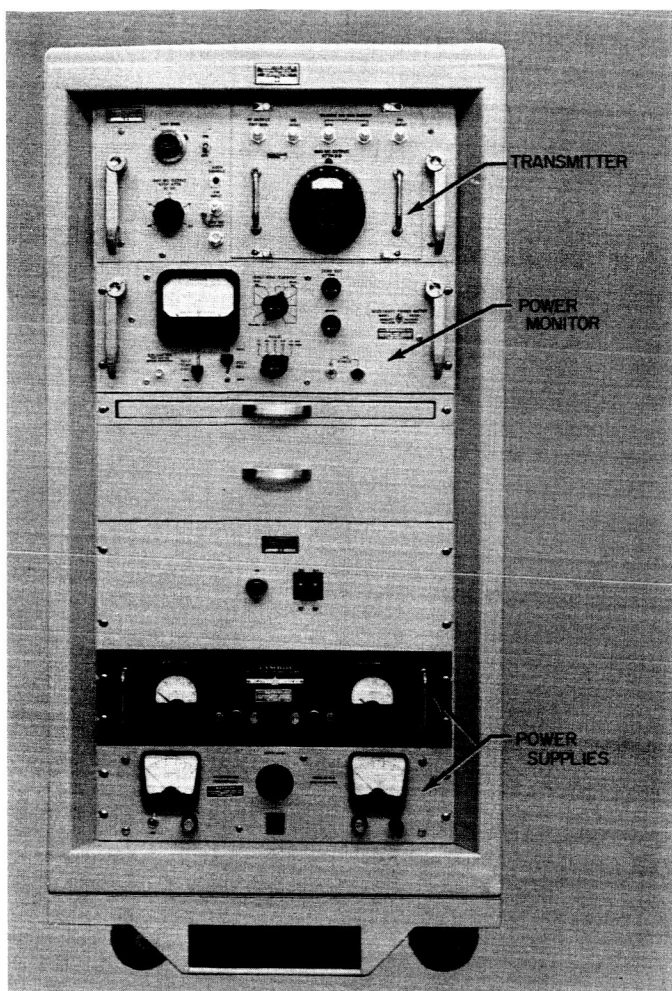


Figure 29. Test transmitter, 890 mc

coherent automatic gain control and for both amplitude and phase modulation monitoring. In addition, the receiver provides either a 29.5-mc or a 10.0-mc reference signal for the panoramic spectrum analyzer which is a part of the test set.

Table 7. Test transmitter characteristics

Characteristic	Value
Frequency, ^a mc	890.046
Tuning range	± 5 parts in 10^5
Power output, dbm down	-30 to -170
Frequency modulation response, kc	0 to 2
Phase modulation response, mc	0 to 5
Amplitude modulation response, kc	0 to 2
Output impedance with VSWR no greater than than 1.2 to 1, resistive ohms	50
Auxiliary VCO signal outputs, mc	29.6682

^aFrequency control by voltage controlled crystal oscillator.

As shown in Figure 30a, the receiver is assembled in a double instrumentation rack with its power supplies, an oscilloscope, a dc vacuum tube voltmeter, and an ac vacuum tube voltmeter. A modular design, illustrated in

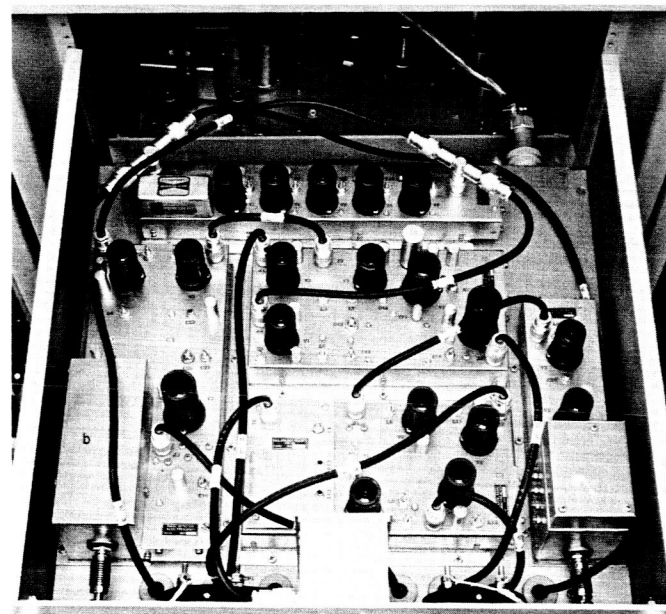
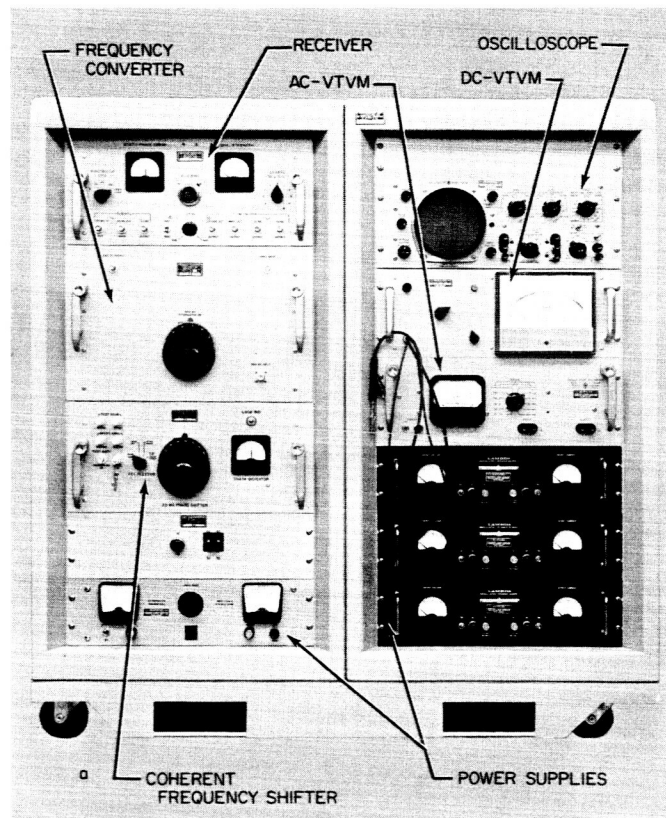


Figure 30. Test receiver, 960 mc

Table 8. Test receiver characteristics

Characteristic	Value
Center frequency, mc	960.050
Tuning range	
By automatic control	± 1 part in 10^5
By manual steps of 1.5 parts in 10^5	± 5.5 parts in 10^5
Selectable APC loop noise bandwidth, cps	5, 10, 20 or 100
Design point signal level, dbm	-50
Dynamic range, dbm down	0 to -100
AGC loop noise bandwidth at design point, cps	10
Amplitude modulation response in manual gain control mode, kc	0 to 5
Phase modulation response when used as phase detector, kc	0 to 5
Input impedance with VSWR no greater than 1.25 to 1, resistive ohms	50

Figure 30b, has been employed in the construction of the RF components with the interconnecting circuits designed to accommodate manipulation of the interconnections, as is often required by special tests for which the test set was not originally designed.

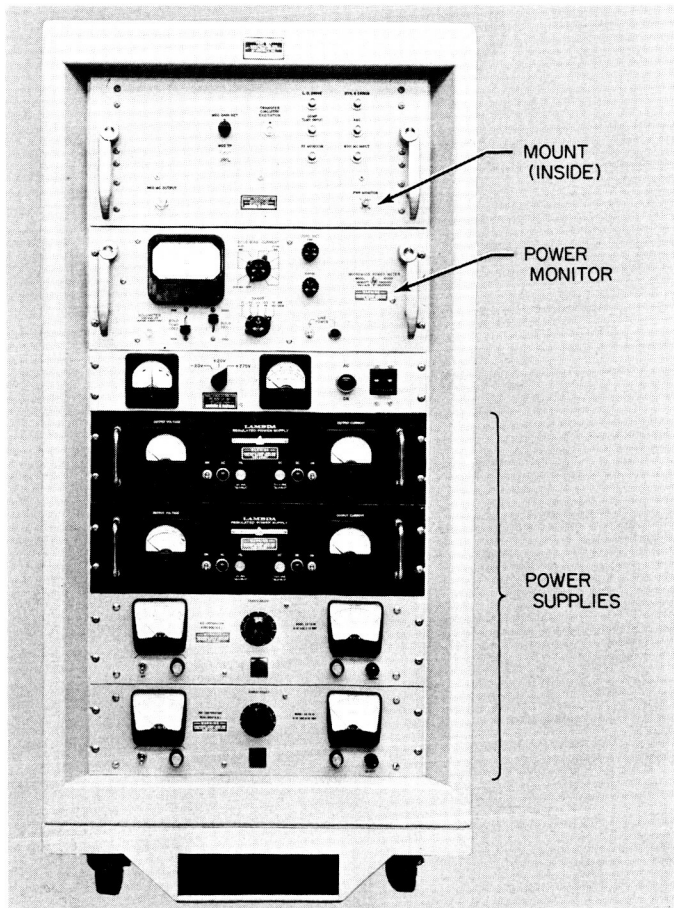


Figure 31. Transponder mount

The transponder mount (Fig 31) provides a convenient means for operating the transponder for test purposes. It includes provisions for powering the transponder and its associated RF cavity amplifiers (up to 25 watts output). RF power dividers, dummy RF loads, and an RF power meter are also provided in the assembly which is shown in Figure 31.

The remaining general-purpose test instruments which complete the test set are: (1) an electronic frequency counter, (2) an ac vacuum tube voltmeter, (3) a dc vacuum tube voltmeter, (4) a cathode ray oscilloscope, (5) a panoramic spectrum analyzer, (6) a telemetering test oscillator, and (7) a low-frequency function generator. These instruments are assembled in another double rack as shown in Figure 32. As with the other assemblies of the test set, the racks are approximately 51 inches high, 28 inches deep, and of standard 19-inch panel width. They are equipped with large rubber castors for ease of handling, and have recessed panels in order to protect the knobs, meters, and terminals.

The first test set has been received from the manufacturer. Inspection and testing has been started to determine the extent to which test set meets the required JPL specifications.

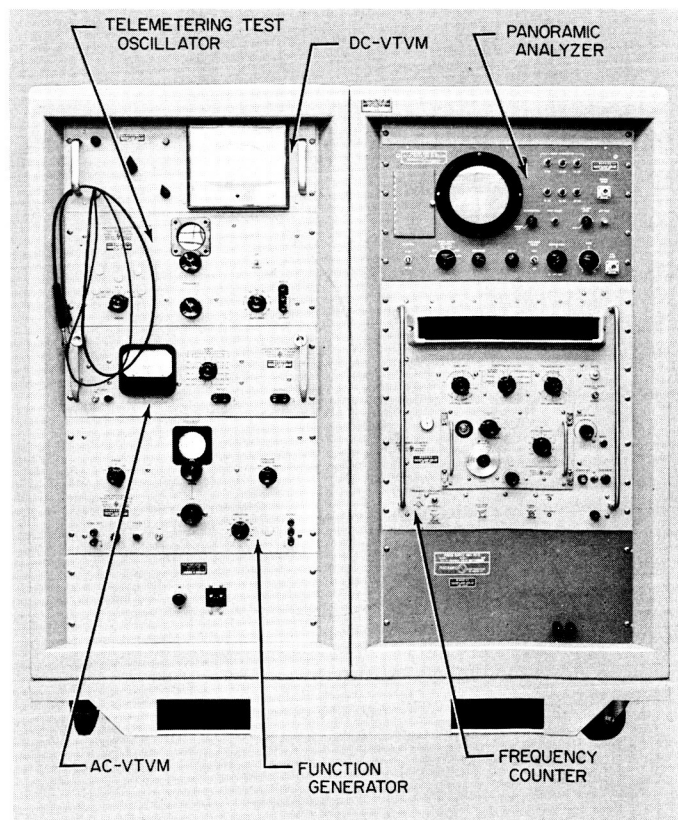


Figure 32. Test instruments

B. Analysis of Coherent Two-Way Doppler Communication System

An analysis of a coherent two-way doppler communication system consisting of a ground transmitter, a spacecraft transponder, and a ground receiver has been performed. Independent noises are assumed to enter both receivers (spacecraft and ground) simultaneously. The effects on the threshold sensitivity of the ground receiver and the measurement of two-way doppler phase are calculated as a function of the noise entering the vehicle spacecraft and the spacecraft receiver bandwidth.

1. System Model

The important features of the system are diagrammed in Figure 33. In this figure, $GH_1(s)$ is the transfer function

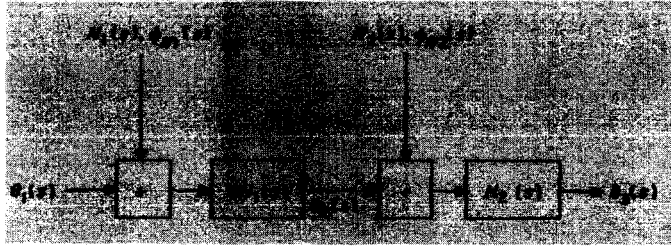


Figure 33. Two-way communication system model

of the transponder relating the output phase to the input phase of the RF carrier; G is the static phase gain and is determined by the ratio of the output frequency to the input frequency, and $H_1(s)$ is

$$H_1(s) = \frac{1 + \frac{3}{4B_1}s}{1 + \frac{3}{4B_1}s + \frac{1}{2} \left(\frac{3}{4B_1} \right)^2 s^2} \quad (1)$$

where B_1 is the effective noise bandwidth of the transponder, defined as

$$2B_1 = \frac{1}{2\pi_j} \int_{-j\infty}^{+j\infty} |H_1(s)|^2 ds \quad (2)$$

The transfer function of the ground tracking receiver is of the same form

$$H_2(s) = \frac{1 + \frac{3}{4B_2}s}{1 + \frac{3}{4B_2}s + \frac{1}{2} \left(\frac{3}{4B_2} \right)^2 s^2} \quad (3)$$

where B_2 is similarly defined

$$2B_2 = \frac{1}{2\pi_j} \int_{-j\infty}^{+j\infty} |H_2(s)|^2 ds \quad (4)$$

Additive Gaussian noises of spectral densities $\phi_{N1}(s)$ and $\phi_{N2}(s)$ are assumed to contaminate the ground-to-spacecraft and spacecraft-to-ground channels, respectively. They are assumed to be uncorrelated and are normalized with respect to the received signal powers.

2. Analysis

a. Ground receiver threshold. The tracking error of the ground receiver is defined as the difference between the receiver output phase and the receiver input phase,

$$\theta_{\epsilon 2}(s) = \theta_3(s) - \theta_2(s) \quad (5)$$

It is important to note that the noise that enters the system at the transponder input must be considered as part of the ground receiver input signal $\theta_2(s)$. Assuming the entire system is distortionless with respect to the original signal $\theta_1(s)$, the ground receiver error spectral density is

$$\phi_{\epsilon}(s) = \phi_{N1}(s) G^2 |H_1(s)|^2 \cdot |H_2(s) - 1|^2 + \phi_{N2}(s) |H_2(s)|^2 \quad (6)$$

From Equation (6) the mean square tracking error due to noise alone may be expressed as

$$\sigma_{\epsilon 2}^2 = \frac{1}{2\pi_j} \int_{-j\infty}^{+j\infty} \phi_{N1}(s) G^2 |H_1(s)| \cdot |H_2(s) - 1|^2 ds + \frac{1}{2\pi_j} \int_{-j\infty}^{+j\infty} \phi_{N2}(s) |H_2(s)|^2 ds \quad (7)$$

If the noise spectral densities are assumed to be flat and B_2 is defined as in Equation (4), the expression can be simplified to a well known form

$$\sigma_{\epsilon 2}^2 = \frac{\phi_{N1}(0) G}{2\pi_j} \int_{-j\infty}^{+j\infty} |H_1(s)|^2 \cdot |H_2(s) - 1|^2 ds + 2\phi_{N2}(0) B_2 \quad (8)$$

The remaining integral in the first term of Equation (8) is of the type solved by Phillips (Ref 1). Its solution is, in terms of B_1 and B_2 :

$$\sigma_{\epsilon 2}^2 = \frac{4}{3} \phi_{N1}(0) G^2 B_1^2 \times \frac{[(B_1 + B_2)^2 - B_1 B_2 - B_1^2/2]}{[(B_1 + B_2)^3 - 2B_1 B_2 (B_1 + B_2)]} + 2\phi_{N2}(0) B_2 \quad (9)$$

This expression may be stated more usefully as

$$\sigma_{\epsilon 2}^2 = 2\phi_{N1}(0) B_1 G^2 K_R(\alpha) + 2\phi_{N2}(0) B_2 \quad (10)$$

where

$$K_R(\alpha) = \frac{2\alpha[(1+\alpha)^2 - \alpha + \alpha^2/2]}{3[(1+\alpha)^3 - 2\alpha(1+\alpha)]} \quad (11a)$$

$$\alpha = \frac{B_1}{B_2} \quad (11b)$$

Values of $K_R(\alpha)$ have been computed and are plotted in Figure 34. For $B_1 \gg B_2$, $K_R(\alpha)$ is seen to be quite close to unity.

Experience has shown that the threshold sensitivity P'_{s2} of a distortionless one-way doppler communications system (spacecraft-to-ground channel only) is determined when the mean square phase noise $(\sigma'_{\varepsilon 2})^2$ is 1 rad²,

$$(\sigma'_{\varepsilon 2})^2 = 2\phi_{N2}(0)B_2 = \frac{2kT_2B_2}{P'_{s2}} = 1 \text{ rad}^2 \quad (12)$$

$$P'_{s2} = 2kT_2B_2 \quad (13)$$

where k is the Boltzmann constant, and T_2 the ground receiver effective noise temperature. If a phase coherent transponder with the same power output is substituted for the fixed transmitter, the new threshold is determined by setting Equation (10) equal to 1 rad².

$$\sigma_{\varepsilon 2}^2 = 1 = 2\phi_{N1}(0)B_1G^2K_R(\alpha) + \frac{2kT_2B_2}{P_{s2}} \quad (14)$$

and the threshold sensitivity of the ground receiver is

$$P_{s2} = \frac{2kT_2B_2}{1 - 2\phi_{N1}(0)B_1G^2K_R(\alpha)} \quad (15)$$

The ratio of P_{s2} to P'_{s2} , which is the ratio of the signal level at threshold for the two-way system to the signal level at threshold for the one-way system, yields an expression for the change in ground receiver threshold as a function of the signal-to-noise ratio in the trans-

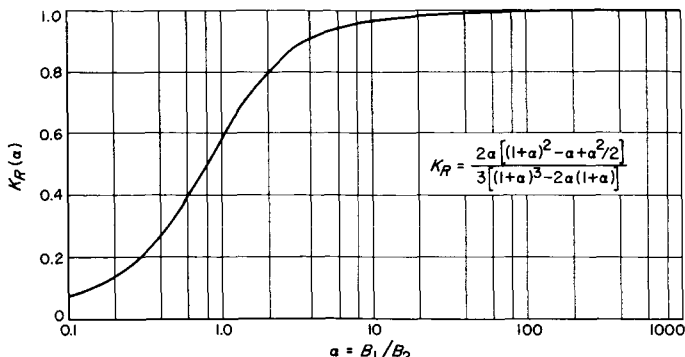


Figure 34. Values of $K_R(\alpha)$ vs α

ponder noise bandwidth $2B_1$. Substituting for $2kT_2B_2$ in (15) from (13), expressing $2\phi_{N1}(0)B_1$ in terms of the transponder input signal and noise,

$$2\phi_{N1}(0)B_1 = \frac{P_{N1}}{P_{s1}} \quad (16)$$

and rearranging

$$\frac{P_{s2}}{P'_{s2}} = \frac{1}{1 - G^2 K_R(\alpha) P_{N1}/P_{s1}} \quad (17)$$

This result is plotted in Figure 35 with $2B_1$ as a parameter and a ground receiver noise bandwidth ($2B_2$) of 20 cps.

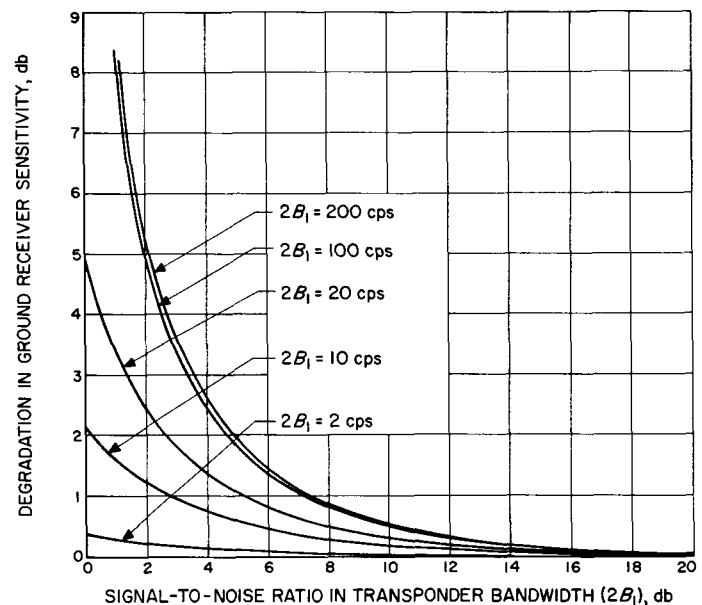


Figure 35. Degradation in ground receiver sensitivity vs signal-to-noise ratio in transponder bandwidth for ground receiver bandwidth of 20 cps

b. Two-way doppler phase error. The two-way doppler phase error is defined by the difference between the ground receiver output and the original signal $\theta_1(s)$ modified by the static gain G of the system

$$\theta_{N2}(s) = \theta_3(s) - G\theta_1(s) \quad (18)$$

Assuming the system is distortionless with respect to the signal $\theta_1(s)$ the spectral density of the error due to noise alone at the ground receiver output is

$$\phi_{N2}(s) = \phi_{N1}(s)G^2|H_1(s)|^2 \cdot |H_2(s)|^2 + \phi_{N2}(s)|H_2(s)|^2 \quad (19)$$

and the mean square output error is

$$\sigma_{N2}^2 = \frac{1}{2\pi_j} \int_{-j\infty}^{+j\infty} \phi_{N1}(s) G^2 |H_1(s) H_2(s)|^2 ds + \frac{1}{2\pi_j} \int_{-j\infty}^{+j\infty} \phi_{N2}(s) |H_2(s)|^2 ds \quad (20)$$

Again assuming flat noise spectral densities and using the procedure presented earlier (Sec II B 2a), the solution for Equation (20) is

$$\sigma_{N2}^2 = 2 \phi_{N1}(0) B_1 G^2 K_D(\alpha) + 2 \phi_{N2}(0) B_2 \quad (21)$$

where

$$K_D(\alpha) = \frac{(1+\alpha)^2 - \alpha/3}{(1+\alpha)^3 - 2\alpha(1+\alpha)} \quad (22a)$$

$$\alpha = \frac{B_1}{B_2} \quad (22b)$$

Values of $K_D(\alpha)$ have been computed and are plotted in Figure 36.

The mean square noise output of a distortionless one-way system at threshold is the same as the mean square receiver tracking error, namely 1 rad^2 (Eq 12). By substituting Equation (15) for P_{s2} in $\phi_{N2}(0)$ and Equation (16) for $\phi_{N1}(0)$ of Equation (21) an expression is obtained for the doppler phase error of a two-way system at ground receiver threshold relative to the doppler phase error of a one-way system of the same transmitter power operating at threshold.

$$\frac{\sigma_{N2}^2}{(\sigma_{N2}^2)_{\text{threshold}}} = \left(\frac{\sigma_{N2}^2}{1} \right)_{\text{threshold}} = 1 + \frac{P_{N1}}{P_{s1}} G^2 [K_D(\alpha) - K_R(\alpha)] \quad (23)$$

Equation (23) is plotted in Figure 37 with $2B_1$ as a parameter and a ground receiver noise bandwidth $2B_2$ of 20 cps.

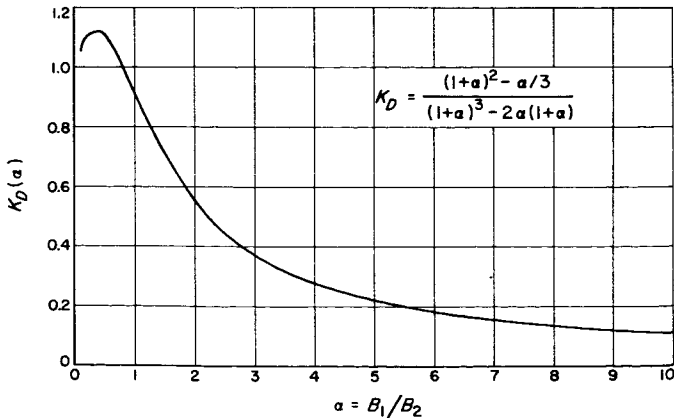


Figure 36. Values of $K_D(\alpha)$ vs α

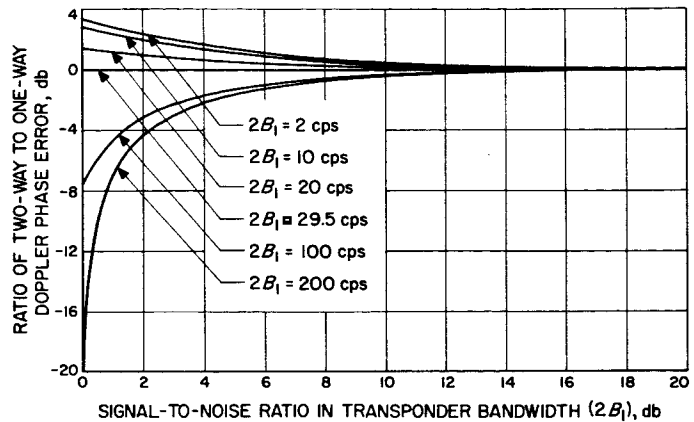


Figure 37. Ratio of two-way to one-way doppler phase error signal-to-noise ratio in transponder bandwidth for ground receiver bandwidth of 20 cps

3. Conclusions

When the signal-to-noise ratio in the transponder bandwidth is large, the ground receiver threshold is unaffected regardless of the size of the transponder bandwidth with respect to the ground receiver bandwidth. When the transponder bandwidth is small with respect to the ground receiver bandwidth, the transponder may be operated near threshold with little deterioration of the ground receiver threshold sensitivity. However, when the bandwidth of the transponder is large with respect to the ground receiver bandwidth, the threshold sensitivity deteriorates quite rapidly as threshold operation of the transponder is approached. Since the bandwidth transponder will, in general, equal or exceed the bandwidth of the ground receiver, this analysis indicates the importance of considering the Earth-to-spacecraft channel in the design of the spacecraft-to-Earth channel. The analysis also demonstrates the importance of utilizing a separate controlled oscillator for the transmitter portion of the transponder when the receiver portion is not interrogated.

The phase variation at the ground receiver output ϕ_{N2} is the noise that would contaminate a doppler velocity measurement. When the transponder bandwidth is 1.48 times the ground receiver bandwidth, and the ground receiver is operating near threshold, the doppler phase error is the same magnitude as that for a one-way system operating near threshold regardless of the transponder input signal-to-noise ratio. When the transponder bandwidth is less than 1.48 times the ground receiver bandwidth, the two-way doppler phase error is somewhat greater than the one-way doppler error. The seriousness of the latter condition depends on the accuracy required for the measurement of radial velocity.

When the transponder bandwidth is greater than 1.48 times the ground receiver bandwidth, the doppler phase error appears to be considerably less than the one-way system noise. However, this region of operation is undesirable as the apparent improvement is obtained at an intolerable expense of ground receiver threshold sensitivity.

Although the analysis has been performed on an idealized model of the coherent two-way communication system, it should be useful for estimating system performance and for selecting the parameters under various operating conditions. The analysis does not take into account the use of limiters in either the spacecraft or ground receivers which automatically widen the bandwidth at signal levels above threshold. Additional analysis is expected to show the effect of the limiters.

oratory investigations have been made to attempt to relate the bandwidth of the required filter to each of the two kinds of noise.

b. Additive noise. When it was decided to investigate the effects of noise on the acquisition procedure, the question of what decision element to use was raised. After some consideration it was concluded that early models of any ranging system would be manually operated and the operator would be the decision element. This inclusion of a poorly defined and certainly non-linear element in the process precludes any but a very qualitative analysis. Therefore laboratory experiments were made to attempt to determine the effect of noise on the acquisition process.

The laboratory experiments with additive noise had three specific objectives; namely, (1) to determine whether a code could be acquired in the presence of noise and if so what was the minimum signal-to-noise ratio that would still allow the code to be acquired, (2) to determine the relationship between the signal-to-noise ratio and the required bandwidth of the filter, and (3) to determine the relationship between the signal-to-noise ratio and the acquisition time.

The demonstration ranging coder reported in RS 36-1, Vol I, was used to generate the two codes and to allow manipulation of the local code during acquisition. In order to simulate the signals which would be used in a system, the codes were converted from a digital form (*ones* and *zeros*) to square waves (plus *ones* and minus *ones*) and fed to a multiplier instead of a Mod 2 adder. A block diagram of the experimental setup is shown in Figure 38. The operational amplifier which precedes the multiplier is used to add the signal and noise and, by means of the capacitor in the feedback, to control the bandwidth of the signal fed to the multiplier. The multiplier is an electronic switch. This is possible since one of its inputs is a square wave. The output of the multiplier passes through the second operational amplifier which is used as a very low-pass filter and to drive the meter.

The experiments performed consisted of acquiring the code with various sweep speeds for the X-component and under various signal-to-noise ratios. The Mode II acquisition procedure (RS 36-1) was used; i.e., in the manipulated code only the X-component was present while acquiring the X-component, only the X- and Y-components were present while acquiring the Y-component, but the entire code was present while acquiring the Z-component.

Some preliminary trials showed that the required time constant for the filter after the multiplier was not very sensitive to the amount of noise added, at least within

C. Deep Space Range Measurement

1. Acquirable Ranging Codes and Noise

a. Introduction. The process of acquiring a ranging code consists of making a series of trial matchings between a locally generated code and the code to be acquired (RS 36-1, Vol I). The correctness of a trial match is tested by multiplying the two signals together and averaging the product over a certain period of time. The correlation properties of the code are such that a reasonable number of trials will assure a correct match between the two codes.

One of the important questions for a system designer who wishes to use such a code is: "Over how long a time must the product be averaged in order to decide whether or not the trial match is correct?" A more practical formulation of this question is: "What is the bandwidth of the filter that should be used between the multiplier and the decision-making device?" The answer to this question depends on two factors, i.e., (1) the amount and kind of noise present with the code to be acquired, and (2) the *self-noise* of the code. The noise to be expected in a communication system using a code is Gaussian with zero mean. However, even if there is no noise added to the signal, there is a minimum bandwidth for the filter. This is because there may be a temporary agreement between the code to be acquired and the locally generated code in the case where the two codes are not matched. Lab-

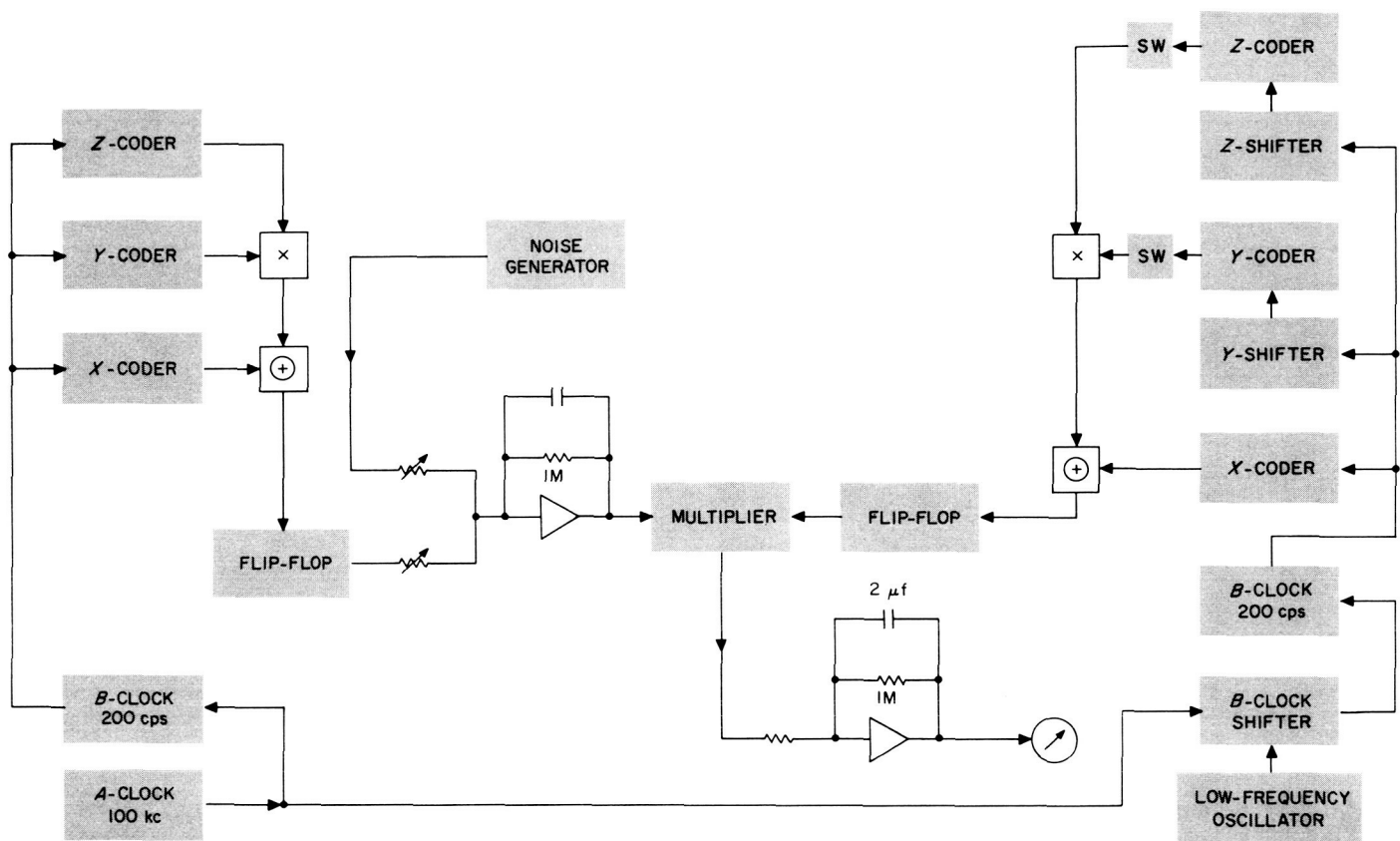


Figure 38. Experimental ranging coder setup for additive noise

the limitations of the experimental setup. It turned out that a noise-to-signal ratio of about 35 db was the largest that the multiplier could handle. With this ratio, the noise peaks were at the breakdown level of the transistors used in the multiplier, and the signal level out was small enough to be troubled by the drift of the multiplier. For any noise-to-signal ratio below 35 db, a 2-second time constant was found to be adequate. This is only 8 times as large as the 0.25-second time constant that was found necessary to smooth the self-noise of the code in previous experiments. This does not imply that the time constant does all of the filtering; the observer does a great deal. This is shown by Figure 39 which gives the average time per step of acquisition for various signal-to-noise ratios. The rather wide scattering of the points is a reflection of the effect on the acquisition time of the alertness of the operator.

An even more startling result was that the X-component of the code could be acquired at a noise-to-signal ratio of 20 db with a sweep speed only twice as slow as that previously found desirable for no added noise. The results of these experiments are therefore mostly qualitative. With respect to the specific objectives, the test results may be stated as follows: (1) It is possible to acquire

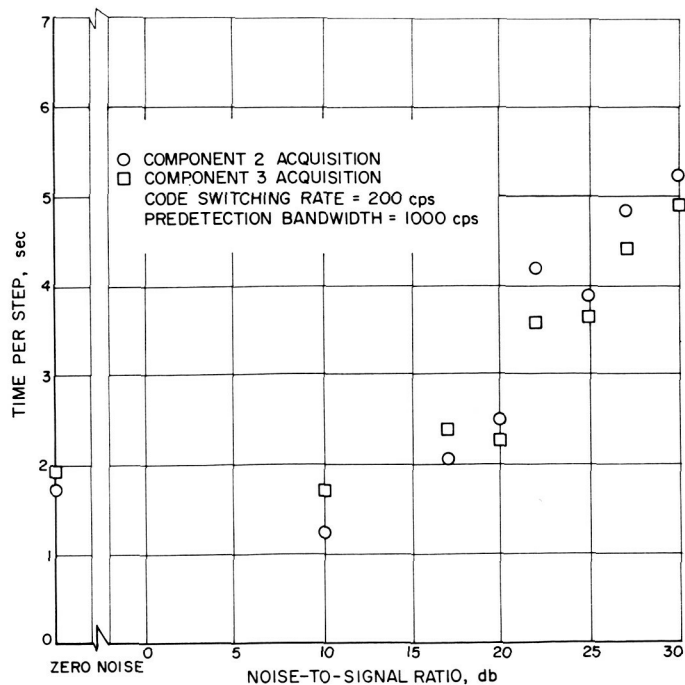


Figure 39. Average time per step for acquisition under various noise-to-signal conditions

the code in the presence of noise exceeding the signal by 35 db; this limit was due to the specific equipment used and is not an inherent limit. (2) No explicit relationship between the required bandwidth of the filter and the signal-to-noise ratio was found; this was because of the limitations of the equipment and because of the tremendous filtering ability of the human operator. (3) An explicit relationship between the acquisition time and signal-to-noise relationship could not be obtained because of the wide variations in the performance of the human operator.

c. Self-noise. In the acquisition procedure described in the previous section, each correlation function is two-valued as long as the entire w_n sequence is observed. However, when only part of the sequence is observed, the value of the correlation function may vary widely. As an example, consider $x_m \oplus x_n$ where $m \neq n$. (In this section, sequences will be considered as consisting of *ones* and *zeros*, and Mod 2 addition will be used instead of multiplication in the correlation process.) By the delay-

and-add properties of a pseudonoise (p-n) sequence, this process forms a new p-n sequence x_c . The average value of this sequence over a whole period is approximately 0.5. However, if less than a whole period is averaged, the value may be somewhat different. In particular, if only $r - 1$ successive digits are averaged, where the length of x_n is $2^r - 1$, the average value may be as low as 0 or as high as 1. This follows from the fact that x_n contains one sequence of $r - 1$ successive *zeros* and two sequences of $r - 1$ successive *ones*. These extreme values would certainly cause confusion in the acquisition process. As longer and longer sections of the code are averaged, the variations from the expected value decrease. This reduces the confusion but slows down the acquisition process. An optimum compromise should be made in the choice of the filter bandwidth for a given signal-to-noise ratio, clock rate, code, and perhaps even for the particular step in the acquisition procedure. In a low signal-to-noise situation, the properties of the code are probably most important. This section is concerned with these properties.

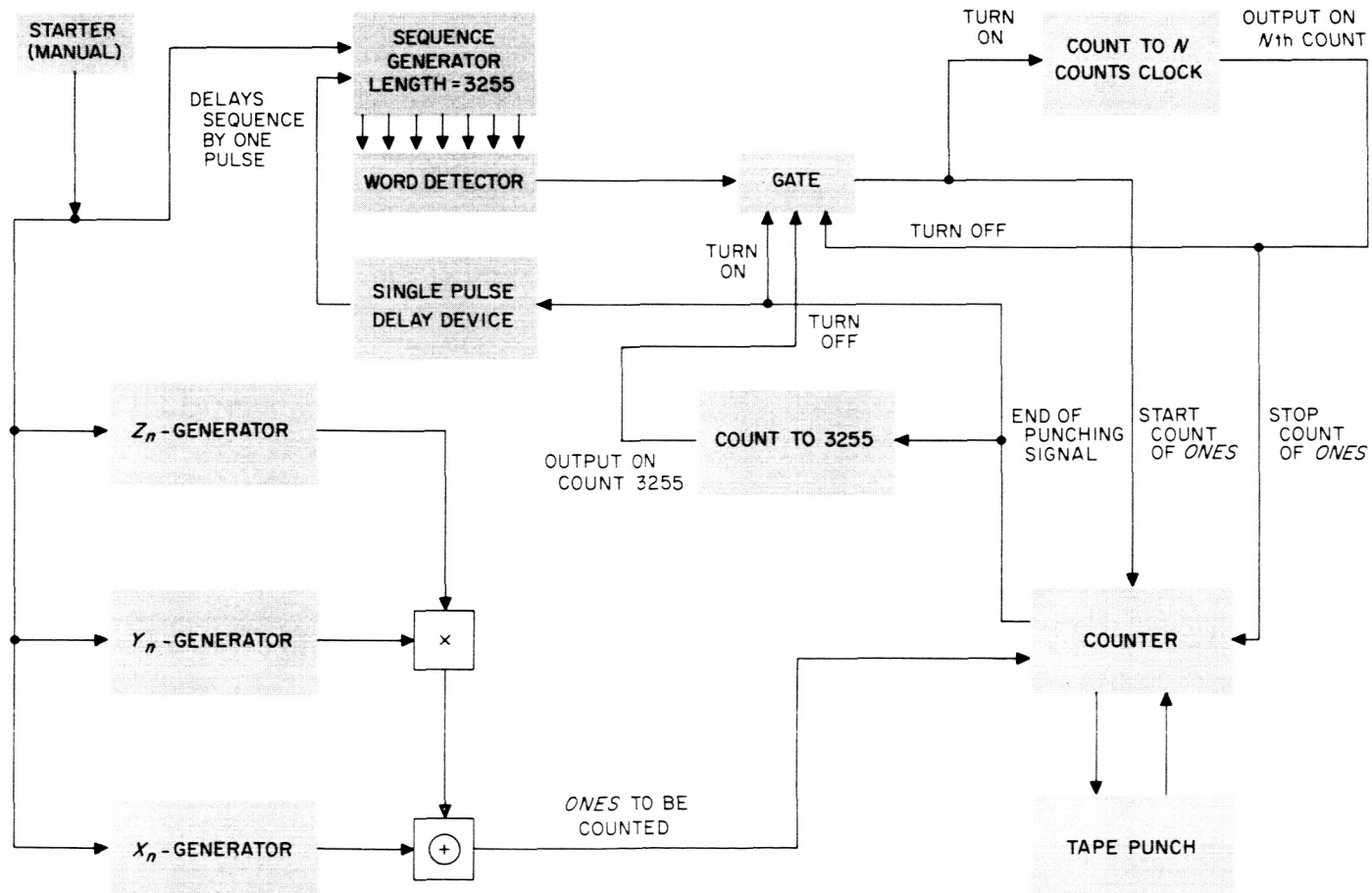


Figure 40. Digital code function w_n generator for counting number of ones in successive words of length n

We will first investigate the results when x_r is correlated with $x_e \oplus y_e z_e$ giving $x_r \oplus x_e = x_n$ for some value n . Thus we have $x_n \oplus y_e z_e$. Further, since the periods of x , y , and z are prime with respect to each other, the total period is the product of the three individual periods. It then follows that the three codes, x , y , and z , will have every possible phase with respect to each other in the complete period, and therefore, so long as $r \neq e$ the correlation will be independent of the relation between r and e .

This function, $w_n = x_n \oplus y_n z_n$, is readily generated with the Computer Control Company digital equipment (Fig 40). All groups of k consecutive digits were examined in the entire code. In the code investigated, x_n had a period of 7, ($x_n = x_{n-1} \oplus x_{n-3}$), y_n a period of 15, ($y_n = y_{n-1} \oplus y_{n-4}$), and z_n a period of 31, ($z_n = z_{n-2} \oplus z_{n-5}$). The length of w_n was of course $7 \cdot 15 \cdot 31 = 3255$. The results of these investigations for $k = 6, 12, 25, 50$, and 100 are shown in Figures 41 and 42. In each case the distribution is compared to the distribution of the number of ones in k consecutive digits of $x_n \oplus x_n \oplus y_n z_n = y_n z_n$, for it is the distinctness of these two distributions that enables one to acquire x_n . It is noticed that for $k = 50$ or less (Fig 41) there is overlap between the correlated and uncorrelated cases. Although in the case of 50 this overlap is small, even a slight amount of external noise might make it exceedingly difficult to distinguish between the two cases. It thus seems evident that a value of k on the order of 100 (Fig 42) is the smallest which allows a fairly sharp distinction between the two cases.

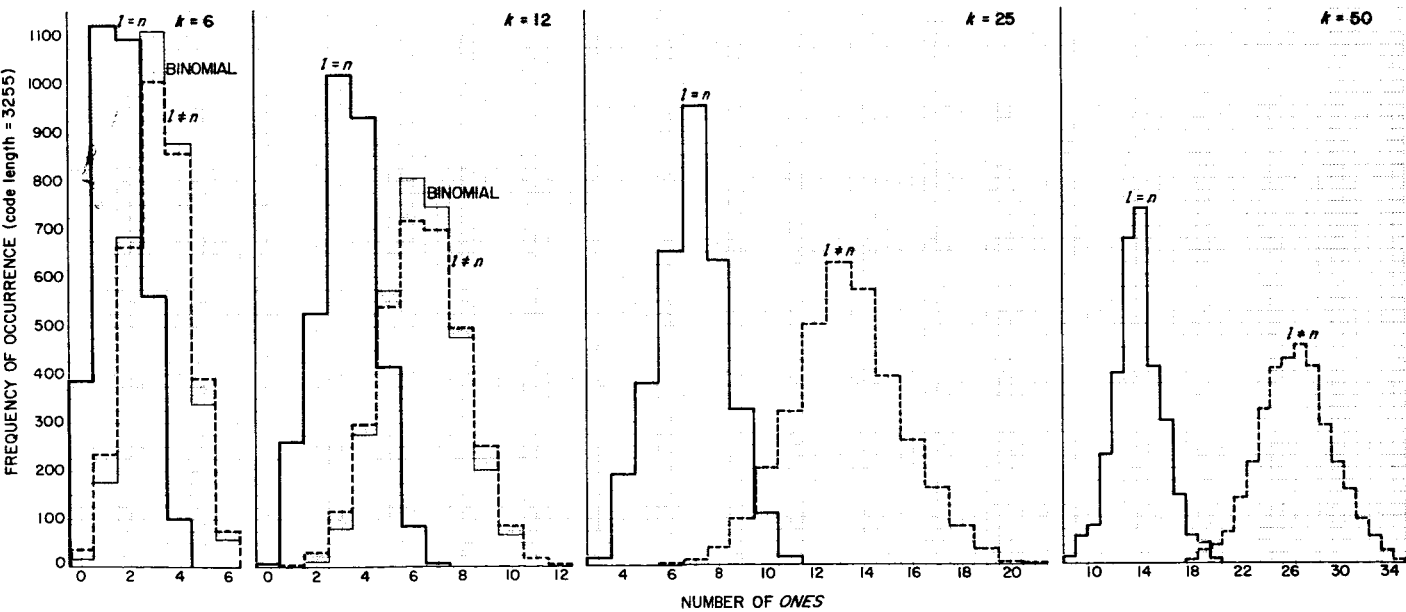


Figure 41. Number of ones in k consecutive digits in the sequence $x_e \oplus x_n \oplus y_n z_n$

In the case of $k = 6$ and 12 (Fig 41), the observed distribution is compared with a binomial distribution where $q = P(w = 0) = P(x = 1, y = 1, z = 1) + P(x = 0, y = 0)$

$$\begin{aligned} &+ P(x = 0, z = 0) - P(x = 0, y = 0, z = 0) \\ &= \frac{4}{7} \cdot \frac{8}{15} \cdot \frac{16}{31} + \frac{3}{7} \cdot \frac{7}{15} + \frac{3}{7} \cdot \frac{15}{31} - \frac{3}{7} \cdot \frac{7}{15} \cdot \frac{15}{31} \\ &= \frac{1523}{3255} \quad P = \frac{1732}{3255} \end{aligned}$$

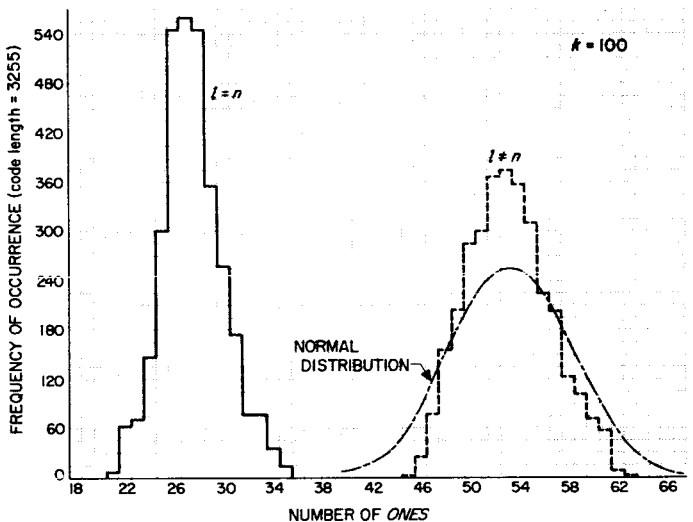


Figure 42. Comparison of distribution of number of ones in code sequence with normal distribution having the same mean and same probability for occurrence of a one

In the case of $k = 100$, the normal approximation to the binomial is used (Fig 42). Note that, in each case, and particularly when $k = 100$, the observed distribution is sharper than the distribution that would be expected if the *ones* and *zeros* were purely random. This sharper curve is not surprising when the sequence is studied more closely. If the sequence were purely random, one would expect to find k consecutive *zeros* with the probability q^k , which is not zero for non-zero q and finite k . However, it is found that a sequence of *zeros* of length 10 occurs with probability 1/3255 rather than the approximately 1/1024 that would be expected for a random sequence, and that the probability of a sequence of *zeros* of length greater than ten is zero. This fact makes it less startling that the curves observed were considerably sharper than would be expected from a random sequence.

It is noted that several other observations may be made concerning the code $x_n + y_n z_n = w_n$. For example, we may write:

$$\begin{aligned} w_n &= w_{n-1} \oplus y_n (z_{n-2} \oplus z_{n-5}) \\ &= (x_{n-1} \oplus y_n z_{n-2}) + (x_{n-3} \oplus y_n z_{n-5}) \\ &= w_{n-1800} \oplus w_{n-780} \end{aligned}$$

where the last step is obtained most easily by applying the Chinese Remainder Theorem. It is obvious that, by grouping the factors of w_n in a different way, or by expanding y_n instead of z_n , different expressions for w_n may be obtained. Thus w_n may be written as a linear (but non-maximal) p-n sequence generated by any of several trinomials, one of which has degree 1800.

Another approach to writing w_n as a linear sequence is to observe that y_n is effectively a switch acting on z_n . Consider one *one* in the y_n sequence. When $y_n = 1$, we have $y_n z_n = z_n$. Hence this particular *one* will pick out every 15th element from the z_n code. But 15 does not divide 31, and it has been shown that when m does not divide the period p of a maximum-length p-n sequence, then selecting every m th element from the sequence generates another maximum length p-n sequence, which may or may not be different from the original. In this case, taking every 15th element from the sequence z_n , we obtain the same sequence, but in reverse order. This sequence would be generated by $z_n = z_{n-3} \oplus z_{n-5}$, which has the characteristic polynomial $1 + v^3 + v^5$. However, since this element occurs every 15th time only, the above polynomial does not describe the new code generated unless we let $v = u^{15}$ so that u_n is not generated by u_n delayed 3 times and u_n delayed 5 times but by u_n delayed 3×15 and 5×15 times. Hence this element may be associated with the polynomial $1 + (u^{15})^3 + (u^{15})^5$. But every sequence obtained by sampling every 15th element of z_n obviously satisfies this expression. Hence this polynomial

certainly holds for $y = 1$. But it trivially holds for $y = 0$ since then all u 's are zero. Hence the polynomial $f(u) = 1 + u^{45} + u^{75}$ is certainly a characteristic polynomial for $y_n z_n$ and it follows that

$$\begin{aligned} F(u) &= (1 + u^{45} + u^{75})(1 + u + u^3) \\ &= 1 + u + u^3 + u^{45} + u^{46} + u^{48} + u^{75} + u^{76} + u^{78} \end{aligned}$$

is the characteristic polynomial for $x_n + y_n z_n$.

Both of these methods show that w_n can be written as a linear sequence. But, in each case, since 3255 is much smaller than the possible maximum length sequence of the order in question, and we are dealing with a very small portion of the total number of possible vectors that could be generated by these shift registers, we gain very little information of interest concerning the nature of the sequence by this process.

The distributions of the number of *ones* in 100 consecutive digits of w_n were determined for the three cases where w_n was altered by reversing one of the sequences x_n , y_n , or z_n . All of these distributions were inferior to that of the original sequence in the sense that the gap between correlation and non-correlation was slightly less. The difference was, however, very slight.

The second and third stages of correlation were also investigated, and typical distributions are shown in Figure 43. Here, although the mean has shifted slightly to the right, the maximum variation is somewhat less, in both cases, than in the first situation. In addition, the mean of the distribution when correlation has been achieved is also shifted to the right, thus providing a net increase in the distance between the correlation and non-correlation distributions:

Case 1: mean = $kp(1) = 100 \times p(y=1, z=1) = 27.5$

Case 2: mean = $kp(1) = 100 \times p(y=0, z=1) = 25.8$

Case 3: mean = $kp(1) = 100 \times p(y=1, z=0) = 24.1$

It is not surprising that the second and third cases do show less variation, since in both these cases the total period is 465, and 100 seems considerably larger with respect to 465 than to 3255 (i.e., we are looking at a much larger percentage of the total code). It is noticed that the distribution is no longer independent of the phase relationship between e and n since y_e and y_n , or z_e and z_n , retain the same phase throughout the code. Figure 43 shows that, indeed, some change in distribution occurs when e is shifted with respect to n .

The block diagram in Figure 40 shows the system used to make all the above measurements. The results were punched out on paper tape, and a Datatron program arranged the data into histogram form. This method involved about 30 minutes to punch out all 3255 words, plus a few minutes processing time on the Datatron. A somewhat more elaborate scheme could eliminate the need for the punch and the Datatron by wiring the com-

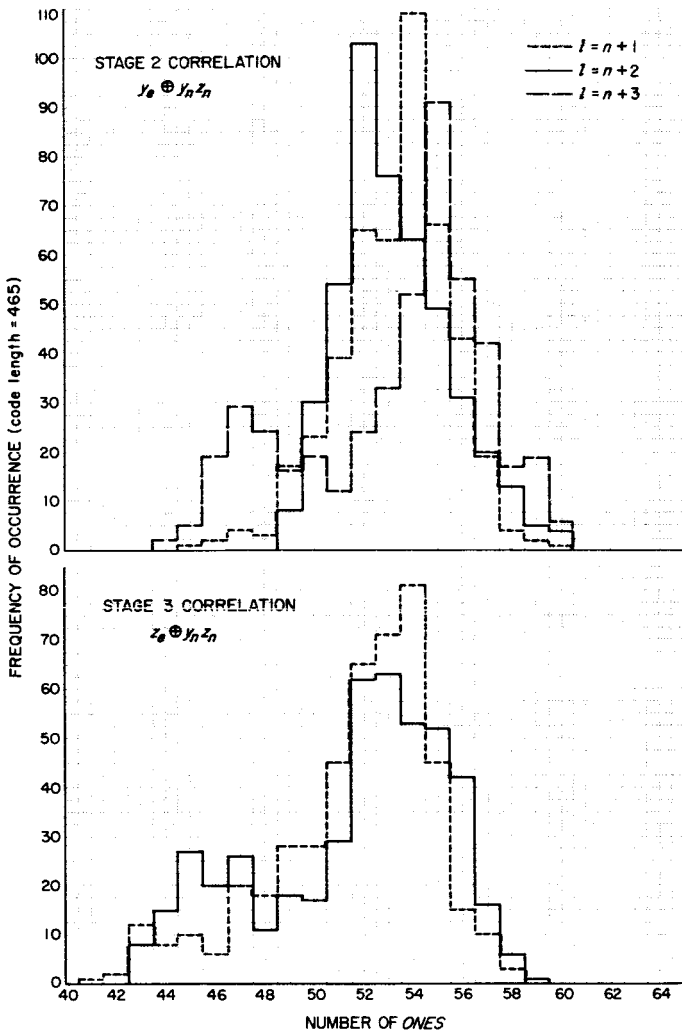


Figure 43. Effect on distribution of number of ones when e is shifted with respect to n in code sequence

puter control equipment to count the number N of words of length k which contain m ones and print out N as a function of m . It could be arranged to advance N by one after every printout. Although considerably more equipment would be involved, this method would be far superior in cases involving longer codes, where the time demanded by the method used here would become prohibitive.

d. Work in progress. For actual field operation, a somewhat different approach to the mechanization of a ranging system has been proposed. In this approach the code will be combined with a subcarrier; the correlation will be done at RF; and the result of matching a component of the local code with a component of the received code will be the detection of a fraction of the subcarrier. Therefore, the amplitude of the subcarrier (relative to the RF carrier) will be a measure of the cross-correlation

of the two codes. The new proposal offers sufficient promise that it has been decided to shift emphasis from the type of work reported earlier to the specific problems raised by the new approach.

2. Ranging Subsystem

a. Introduction. After the demonstration of the acquisition properties of the ranging code (RS 36-1), it was decided to build a system incorporating the code to operate with the transmitter and receiver at Goldstone. A number of systems were proposed which differed mainly in the way they handled three main functions: (1) the recovery of the code at the receiver for comparison with a locally generated code, (2) the determination of range from the phase difference between the transmitted code and the locally generated code, and (3) the interconnection of the Goldstone transmitter and receiver which are 7 miles apart. Finally, a system was evolved which seemed to handle these three functions in a satisfactory way, and the design and construction of a system was begun.

Since the objective of the research effort was to derive new system techniques, as opposed to component techniques, it was decided to use standard digital building blocks in the development of the system. It was believed that such an approach would allow the testing of the system concepts in the field in the shortest possible time and that the experience gained could be applied to the development of a more permanent system at a later date. Furthermore, if the system concepts proved feasible, a more extensive development effort would be justified. This summary report describes the ranging system that is being built.

b. Theory of operation. The ranging system is being developed initially to measure the range to a passive (i.e., reflecting) spacecraft or satellite, but the system concept may be extended to the ranging of a transponding probe. The basic idea is to transmit a radio wave which will be reflected back to a receiver. The range is measured by determining the time required for the wave to travel to the probe and back. The method used to measure the travel time is the key part of the system concept. The transmitted wave is modulated by a ranging code. The code which has made the round trip to the probe is acquired at the receiver; i.e., a locally generated code is matched to the received code. The clock frequency of the transmitted code is known precisely so that the number of clock periods by which the local code lags the transmitted code is a measure of the round trip time of the radio wave. The system is shown schematically in Figure 44.

It is desirable that the code generator associated with the receiver stay locked to the received code once the

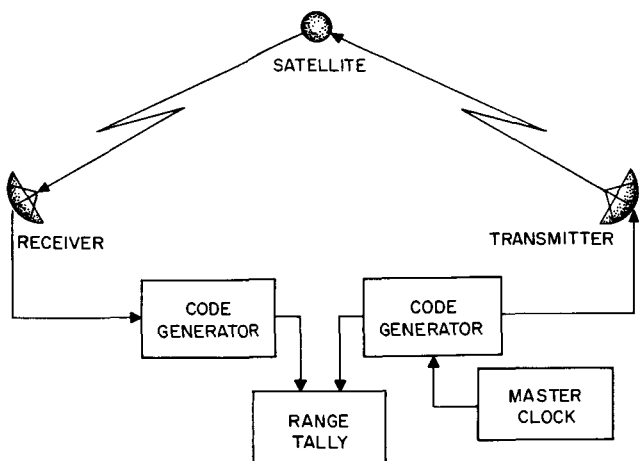


Figure 44. Ranging system for measuring round trip time of coded radio signals

received code is acquired. This is accomplished by transmitting the code times its clock and using a double loop in the receiver. The form of the double loop (omitting the RF and IF frequencies and carriers) is shown in Figure 45. The output of the first multiplier has a component at the clock frequency if, and only if, at least the x -components of the two codes are in phase. If there is a component at the clock frequency, the inner loop (which is a conventional phase-locked-loop) will lock to this component and track it. Since the output of the VCO then stays matched to the incoming clock, the local code which it controls stays matched to the incoming code.

A typical acquisition procedure for a ranging code of the form $w_n = x_n + y_n z_n$ would be as follows: (1) Assuming that no component of the local code was in phase with the received code and that the VCO frequency was different from the received clock frequency, the local code would sweep past the received code until the two x -components were in phase. At that time the phase-locked-loop would lock up and the sweeping would stop. Note that the y - or z -components coming into phase would have no effect on the phase-locked-loop unless the

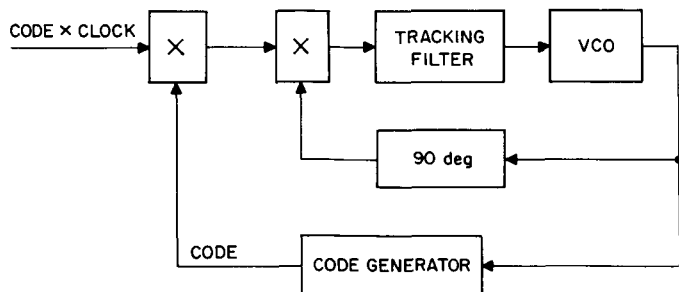


Figure 45. Double loop receiver

x -component were to come into phase simultaneously. The acquisition of the x -component is detected by a lock indicator which fits into the system as shown in Figure 46. (2) When the phase-locked-loop is locked, the two codes will run at the same rate. The y -components then have one of p_y possible phases with respect to each other, where p_y is the length of the y -component. The y -component of the received code may be acquired by stepping the y -component of the local code one clock period at a time (either progressively forward or progressively backward) and observing the lock indicator. The indicator will show an increase when the y -components are in phase; in RS 36-1, the theory of ranging code acquisition is described. (3) The z -component of the received code would be acquired in a manner identical to that used for the y -component.

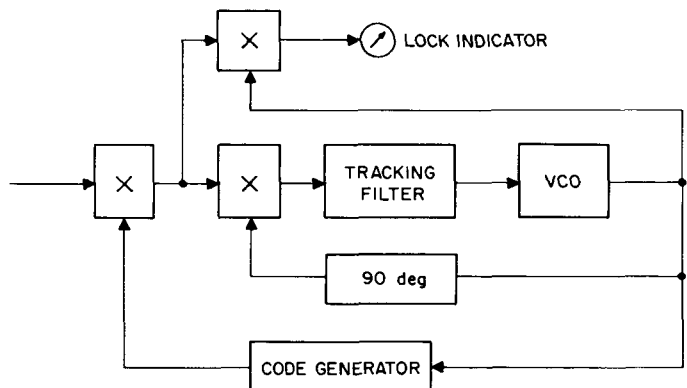


Figure 46. Receiver with lock indicator

The two-loop system described above provides a means for acquiring and tracking the code which has been reflected from the probe. Furthermore, the displacement of the local code with respect to the transmitted code in terms of code clock periods is a measure of the travel time to and from the probe and hence of the range. It remains to be shown how to determine the displacement between the transmitted code and the local code.

Assume first that the displacement between the two codes is known at some instant and that it is exactly some integral multiple of the clock period. Then at that instant the output of the master clock used for the transmitted code and the output of the VCO are in phase. Suppose that the probe recedes so that the round trip distance to the probe increases by one clock period. The clocks for the two codes are again in phase. Moreover, the phase of the VCO output has changed by -2π radians with respect to the master clock output. Therefore, if a device were used to measure the phase between the two clocks, the knowledge of the displacement between the two

codes could be kept up to date by adding or subtracting one clock period to the record each time the phase of the VCO output changed by 2π radians with respect to the master clock output.

This approach suggests a solution to the whole problem. If prior to the acquisition procedure the local code were synchronized with the transmitted code, and if the incremental displacements of the local code at each step of the acquisition procedure were tallied, the total displacement would be known at the end of the acquisition procedure. The record of the displacement could then be kept up to date by the method described in the preceding paragraph. A method has been found for keeping track of (tallying) the incremental displacements; it will be described in a later section.

A ranging system such as that described has a resolution (and accuracy) of plus-or-minus one clock period. Since round trip time is being measured, this amounts to one-half the clock wavelength in range. Since available digital equipment for generating the codes has a limited operating frequency, there is a limit to the resolution that may be obtained. Small increases in resolution may be obtained by making the increments fractions of a clock period; quarter clock periods can be tallied unambiguously even in the presence of noise. However, any attempt to cut the clock period into smaller pieces does run into trouble in the presence of noise. A method that can be used, with certain limitations, is to transmit along with the code and the clock a higher frequency which is coherent with the clock. This signal then acts as a vernier on the clock. The phase of this signal at the receiver with

respect to its counterpart at the transmitter changes n times as fast as the phase of the VCO relative to the master clock, where n is the ratio of the frequencies. In the noiseless case, the problem is simple. After acquisition, the range record is being kept up to date by tallying clock periods. At an appropriate time, the tallying of clock periods is stopped and the tallying of periods of the higher frequency is started. The appropriate time to make the change is immediately after a clock period is tallied. The situation is shown in Figure 47 for a case where the spacecraft is approaching; i.e., the range is decreasing. A ratio of frequencies of only 6 is used in the figure for clarity.

If there is noise on the received code-times-clock signal, there will be phase noise on the output of the VCO. Assume that there is no noise on the high-frequency signal (an assumption which will be justified later). Then if we restrict our attention to the instants at which the phase angles of the two signals are zero, the situation is as shown in Figure 48. In this figure the frequency ratio is considered to be high, perhaps 50. Note that, due to the noise, we cannot say when the clock signal will have zero phase. All that can be said is that there is a probability distribution of times when the phase is zero. If an occurrence of zero phase is selected to start tallying high-frequency periods, it will in general occur at the wrong time. If it occurs too soon, then too many high frequency periods will be tallied, and vice versa. Fortunately, it turns out that the mean of the distribution occurs at the correct time. Therefore, a statistical estimation procedure can be devised which gives a good estimate for the error

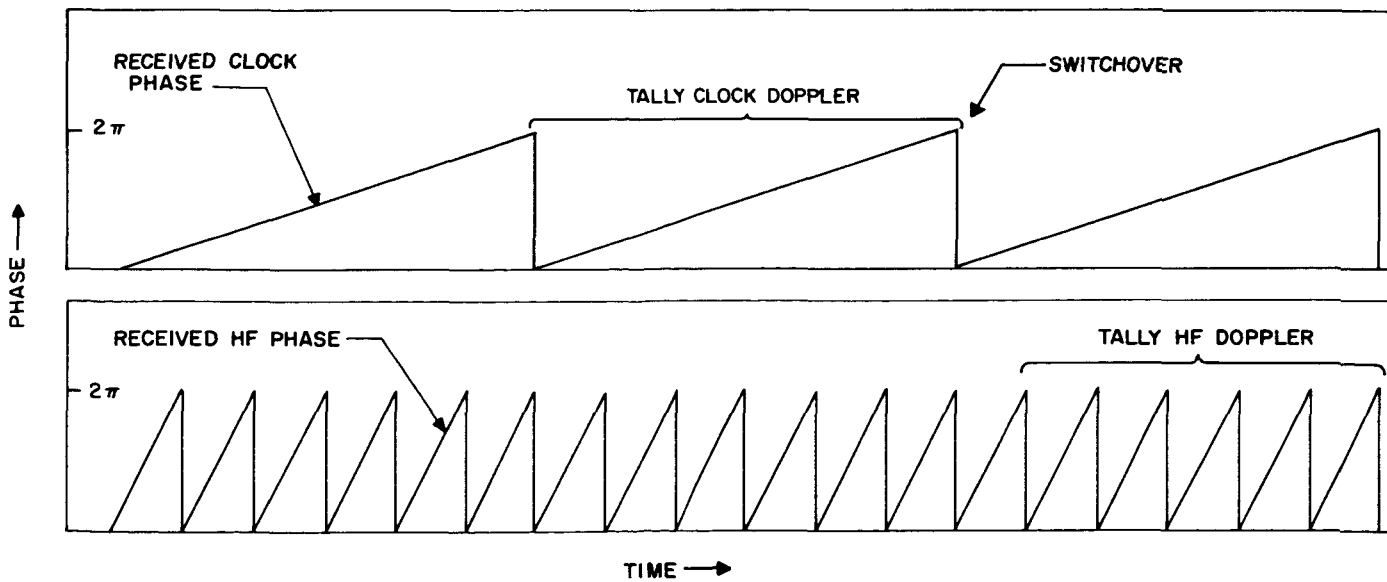


Figure 47. Phases of received clock and received high-frequency with no noise present

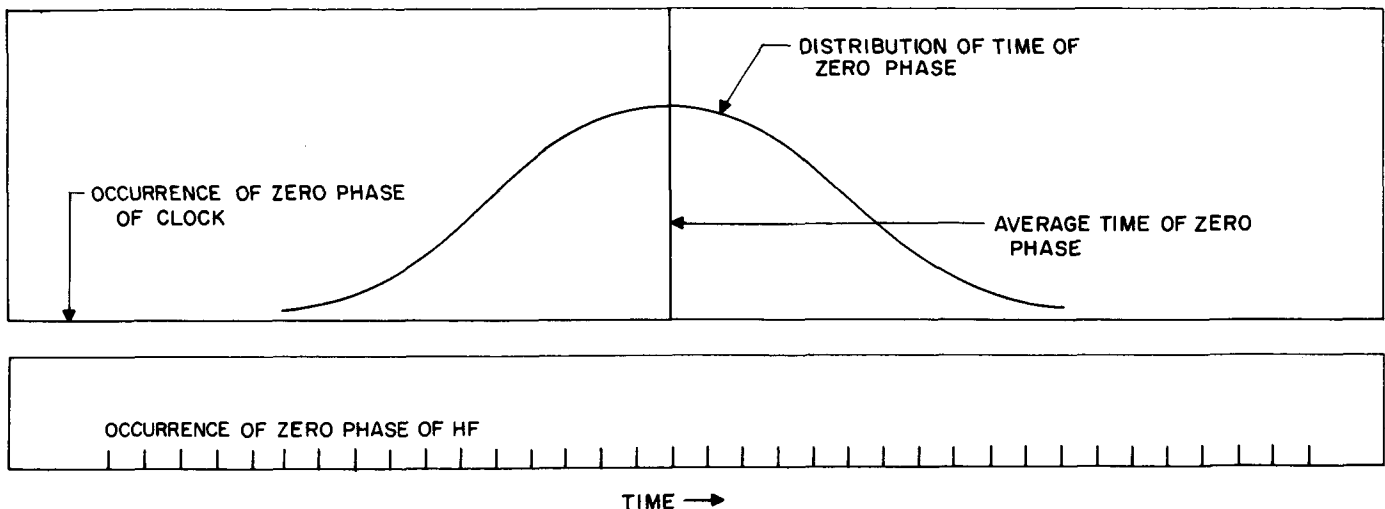


Figure 48. Occurrence of zero phase of received signals with noise present

that is made when the switchover from tallying clock periods to high-frequency periods occurs. This estimate of the error can then be used to correct the displacements as tallied.

In the ranging system which is being built, the RF carrier and the transmitter code clock are both derived from the same master oscillator. For various reasons, the code clock was selected to be 500 kc. In the mechanization of the receiver, it turned out that a divided-down version of the RF was available at approximately 30 mc. This signal was chosen for use as a vernier on the clock. Because the 30-mc signal was obtained by dividing the RF by approximately 80, it has essentially no noise. At threshold, the RF signal has an rms noise of 1 radian; so the 30-mc signal has at most an rms phase noise of about 0.75 degree. This justifies the assumption of no noise on the high frequency made earlier. The use of this 30-mc signal allows the resolution of the ranging system to be increased by approximately 60 (the actual ratio of the frequencies is 59 $\frac{1}{4}$). The restriction on this resolution is that a statistical estimation must be made to determine the error introduced at the switchover time. This estimation requires time to make; so the higher resolution is not available immediately upon starting to tally the higher frequency periods. However, the estimation applies to the original error made at switchover; so the correction is applicable retroactively to all data that might be taken after the switchover. A description of the estimation process and its mechanization is given in a later section.

After considering many ways to interconnect the Goldstone transmitter and receiver, which are located 7 miles apart, it was concluded that the simplest way was to provide a broadband link between the two so that the code and clock to be transmitted could be generated at the

receiver and sent to the transmitter. One broadband channel on the intersite microwave link between the receiver and the transmitter was therefore reserved for the ranging system. This approach obviated the need for methods of synchronizing code generators separated physically. The additional time required for the transmission of the code over the link is a constant which can be measured and subtracted from the measured round trip time of the signal. The whole problem of calibration is one which will be discussed in detail in a later section.

The approaches to the several problems of a ranging system which have been discussed led to a system which has the form given in Figure 49. The purpose of this figure is to show how all of the signals involved in the ranging system are generated and related. In this figure, no attempt is made to show the full form of the transmitter and the receiver. In particular, all of the IF portions have been omitted, and the entire RF tracking system has been reduced to one block.

Perhaps the best way to explain the interrelations between the parts of the block diagram is to describe the acquisition and subsequent operation of the system. There is a master oscillator associated with the transmitter system which sets the standard of time for the entire system. At the beginning of a tracking mission, an unmodulated component of the RF (derived from the master oscillator) is transmitted. This RF signal is acquired and tracked by the RF loop in the receiver. The output of this loop provides a model of the unmodulated component of the received signal.

In order that a time standard may be available at the receiver site to operate the transmitter coder, the master oscillator frequency is divided down and sent over the microwave link. This frequency (500 kc) is used as the

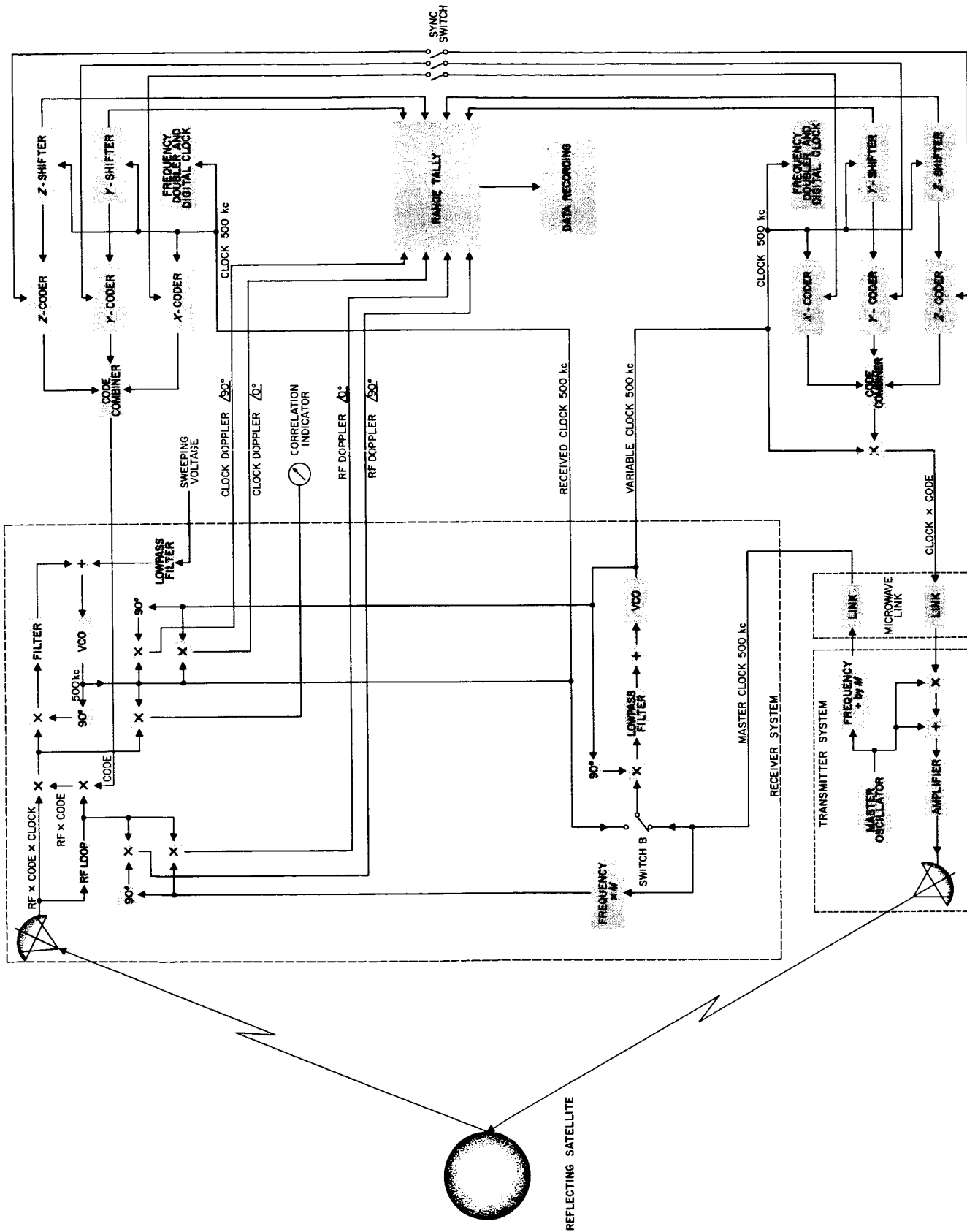


Figure 49. Passive satellite ranging system

master clock at the receiver site. It was not feasible to separate the transmitter coders and the receiver coders, so the transmitter coder could not be placed at the transmitter site.

c. Mechanization and calibration. The first step in acquiring the ranging code is to synchronize the two coders. In order to do this the two coders must be operated from the same clock. Since in normal operation the transmitter coder operates from the master clock and the receiver coder operates from the receiver VCO, some means must be provided to switch the clock to one of the coders. The *switch* is the phase-locked-loop in the center of the diagram. When the switch is moved from the upper to the lower position, the output of the VCO will change slowly (due to the lowpass filter) from the frequency of the receiver VCO to the frequency of the master oscillator. This signal will always be a clean sine wave, even during the switching. In order to synchronize, then, the switch is put in the upper position. Both coders are then driven by the free-running receiver VCO. The two coders are synchronized, and the range tally is reset to zero to indicate no displacement between the two codes. When the switch is thrown to the lower position, the frequency of the clock for the transmitter coder will change slowly to the frequency of the master clock. As soon as this frequency shift starts, the two codes will start to drift out of synchronism. The range tally must be able to keep track of all shifts including this one. This shift is *interpreted* by the range tally as a doppler shift, since it has the same effect in shifting the two codes with respect to each other. In the system the transmitter code is always taken as the reference even though it may be

the code that is actually shifting. This *pseudo doppler* is detected by means of the two detectors whose outputs are labeled *clock doppler*. The two detectors are required in order to give a sign to the shift.

After the transmitter coder is operating from the master clock and the code at this frequency has propagated to the probe and back to the receiver, the received code will generally be at a different frequency (and phase) from the receiver coder code. It may be necessary to inject a sweeping or bias voltage into the receiver phase-locked-loop to assure this. At any rate, because of this difference in the two frequencies, the two codes will sweep past each other until the *x*-components match and the receiver phase-locked-loop locks up. All of the shifts up to this time will be tallied by counting the *pseudo doppler*. After this time, any doppler cycles will be due to actual change in range of the vehicle, because the transmit and receive clocks will be locked to the transmitted and received signals, respectively.

The acquisition procedure continues with the *y*- and *z*-components being stepped into synchronism with the received code. The range tally accumulates the shifts step by step. After the received code is acquired, the range tally indicates the range, and the tally is kept up to date by counting the clock doppler. At the time, the mode of operation of the range tally is changed to count the RF doppler. After this change, the range is measured in the smaller increments of the 30-mc half-wavelength.

The many necessary details omitted in this preliminary description of the system will be supplied in later *Summaries*.

III. SYSTEMS ANALYSIS

A. Trajectory Analysis

1. Interplanetary Trajectories

a. Launch dates. A study has been completed to determine typical Mars and Venus trajectories for 1964 launching dates. These trajectories were computed using the five-body interplanetary program. The criteria for selection of the Mars trajectories was that the communication distance from Earth be in the vicinity of 100 million miles at encounter. For Venus, the selection criteria was that

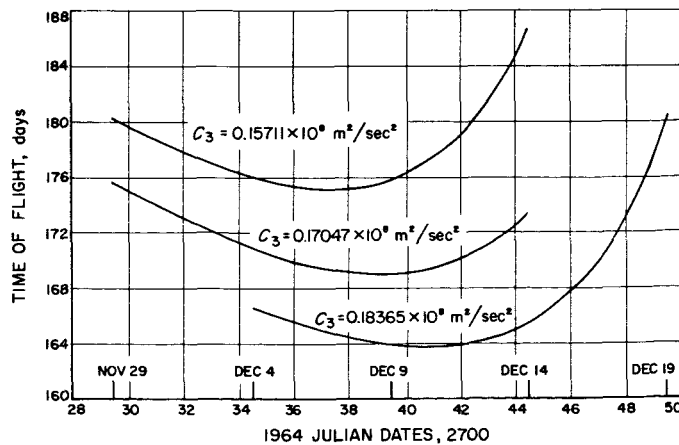


Figure 50. Spacecraft time of flight to Mars vs 1964 launch date

the trajectories have nearly the minimum energy of escape for the 1964 era of Venus launchings. Figures 50 and 51 show Mars flight times and communication distances as a function of launch date for three energies, C_3 . Here, C_3 is the energy per unit mass of the spacecraft near the Earth. It is interesting to note that the minimum-energy Mars launch dates for 100 million mile communication distance trajectories for 1960, 1962, and 1964 advance by about 1 month and 5 days each launching era. For example, in 1960, these launchings occur from 1 to 5 October; in 1962 they occur from 5 to 10 November; and in 1964 from 8 to 15 December.

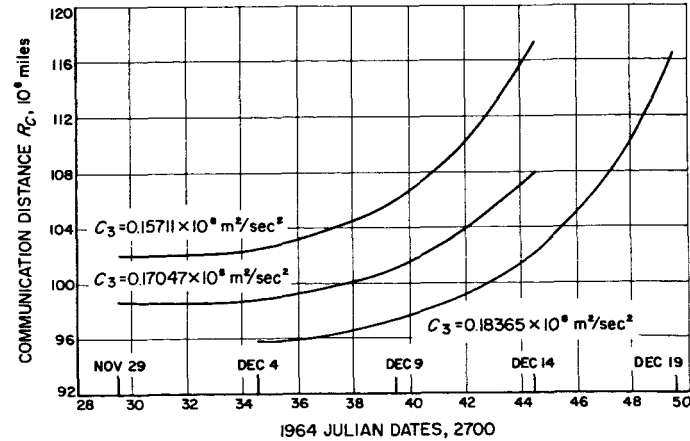
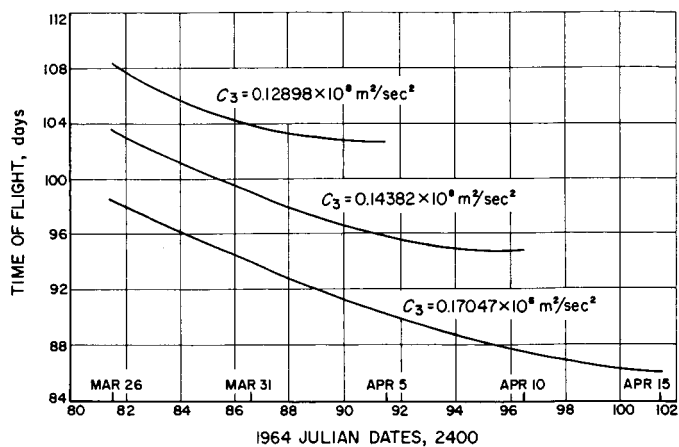


Figure 51. Communication distance to Mars spacecraft vs 1964 launch date



**Figure 52. Spacecraft time of flight to Venus
vs 1964 launch date**

Figures 52 and 53 show the variation of flight time and communications distance for 1964 Venus launchings.

b. Injection locations. For purposes of range tracking and telemetry, it is of interest to know the approximate

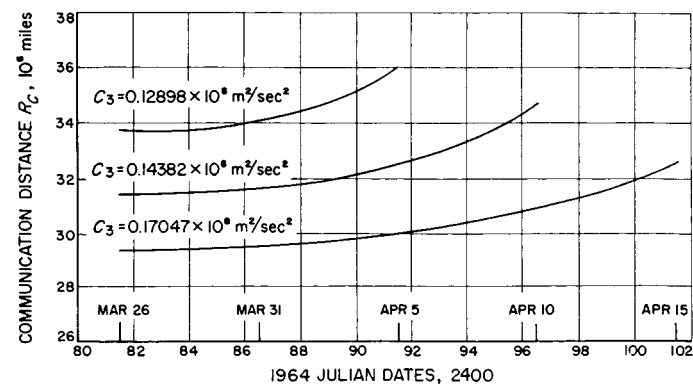


Figure 53. Communication distance to Venus spacecraft vs 1964 launch date

locations of the injection points of lunar and interplanetary trajectories. These locations are strongly dependent on the declination of the outgoing asymptote of the near-Earth escape hyperbola. Generally, it is found that asymptotes with increasingly positive declinations require longer parking orbits. Asymptotes with increasing

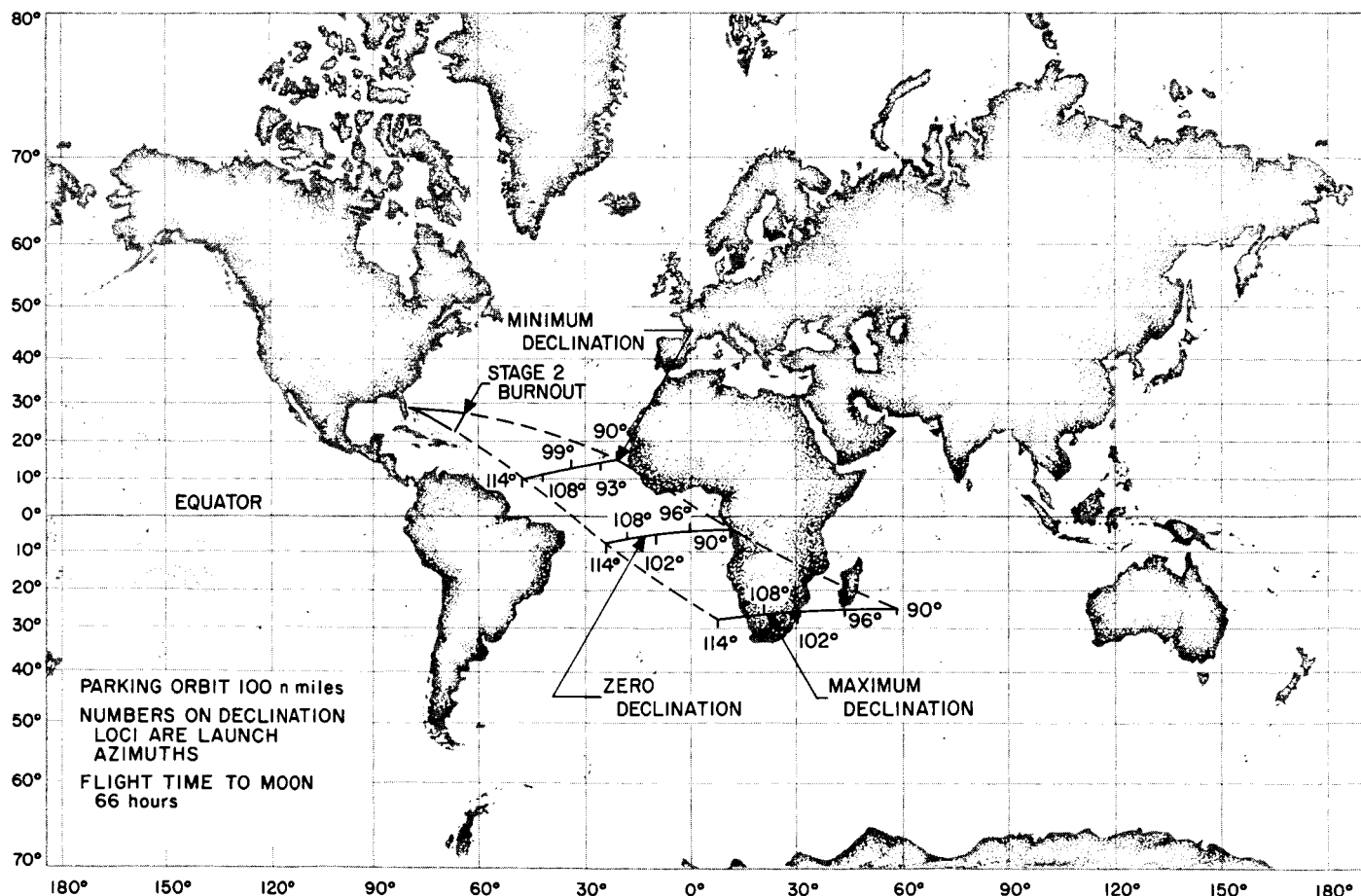


Figure 54. Lunar injection loci

ingly negative declinations require shorter parking orbits. Thus, when the Moon is at maximum positive declination, the parking orbit is longest. When the Moon is at maximum negative declination, the parking orbit is shortest. This phenomenon is illustrated in Figure 54. It is noted that the length of the parking orbit is also dependent upon the chosen launch azimuth. These statements are true for the Moon even though the near-Earth conic is an ellipse.

For Mars trajectories in 1962, the declination of the asymptote is about 34 degrees, and injection points for southeast launchings occur in the Indian Ocean, as shown in Figure 55. For northeast launchings, they occur between Australia and New Zealand.

In 1964, the shape and character of the Mars injection loci (Fig 56) change considerably from 1962; both southeast and northeast launchings yield injection points in the Indian Ocean as well as across the whole Pacific Ocean. In comparing 1964 Mars injection loci to 1962, one marked difference is noted. This difference is the ability to fire due east in 1964 but not in 1962. In fact, the maximum

permissible northeast launch-azimuth is about 68.72 degrees and minimum permissible southeast azimuth is 111.28 degrees. These limits are somewhat dependent on flight time, but most strongly dependent on the declination of the asymptote. The reason that due east firings are permissible in 1964 and not in 1962 is that the asymptote declination falls to about 18 degrees in 1964. It is true that for asymptote declinations greater than the launch latitude, no due east firings are permissible; whereas for asymptote declinations below the launch latitude, not only are due east firings permissible, but the shape and character of the injection loci change considerably.

2. Differential Corrections

Differential corrections for the impact parameter \bar{B} have been determined for a 176.7-day flight-time Mars trajectory. The impact parameter B is a vector originating at the center of the target planet and oriented perpendicular to the incoming asymptote of the hyperbola near

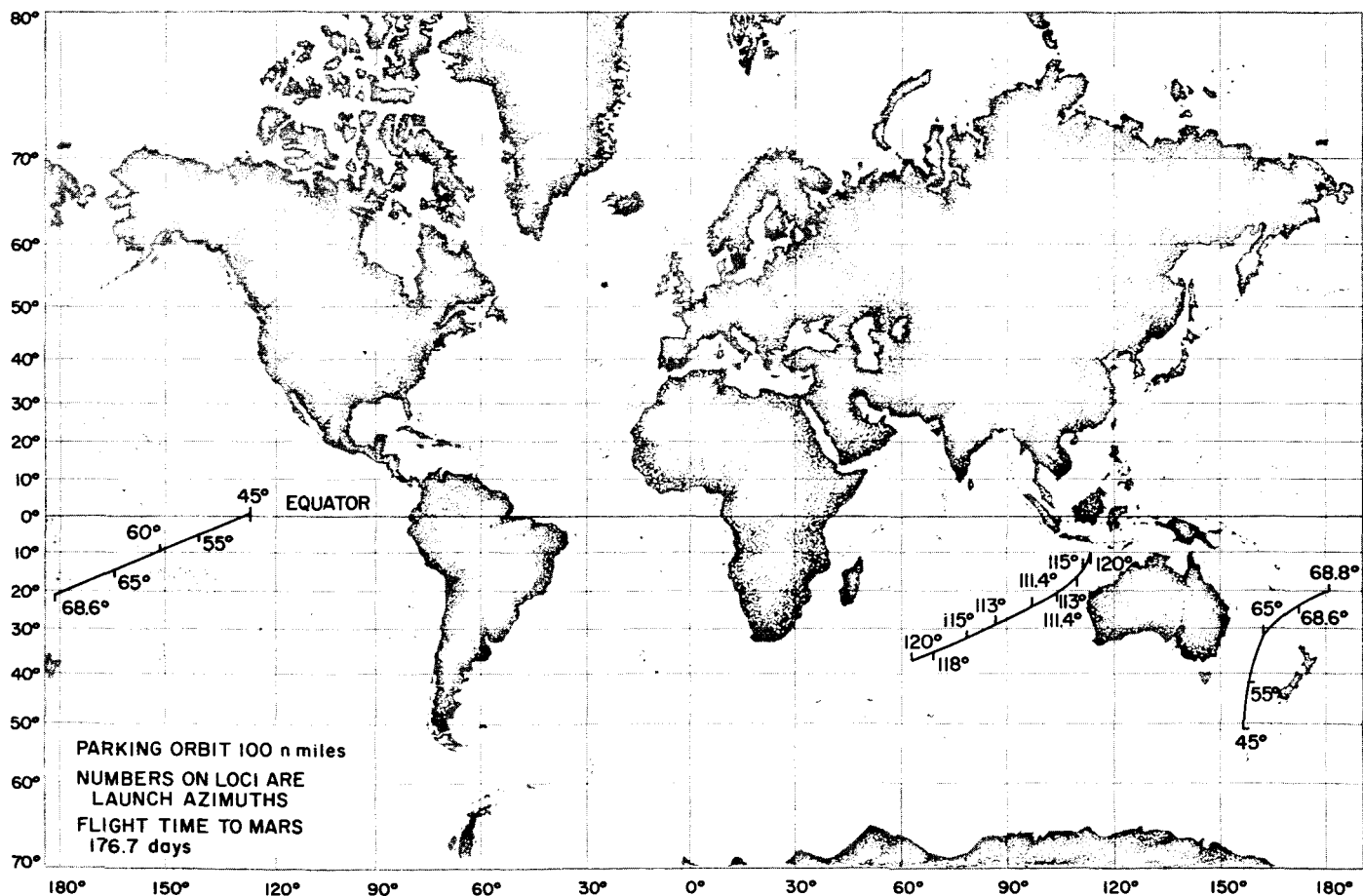


Figure 55. Mars 1962 injection loci

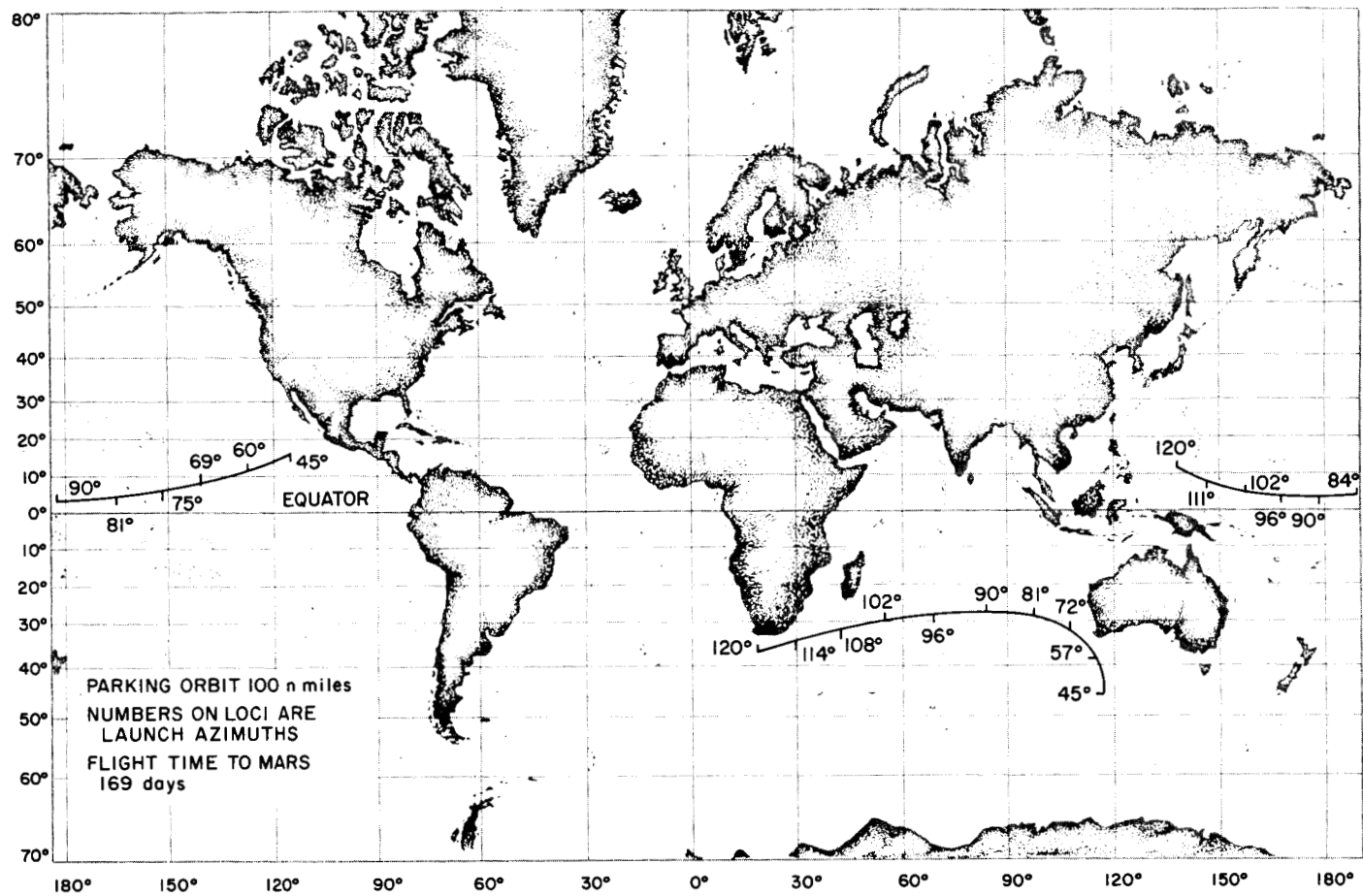


Figure 56. Mars 1964 injection loci

the target body. The differential coefficients of \bar{B} are given in Table 9.

3. Moon-to-Earth Trajectories

An interesting problem under study is that of how to return to the Earth after landing on the Moon. At first glance it might be thought that one could simply depart vertically (with the appropriate speed) from the place of impact on the Moon. However, though this may be true for some impact locations, it is not generally true for departure from impact locations arising from simple vertically descending Earth-to-Moon trajectories. The impact locations of these simple trajectories all occur on the left side of the Moon as seen by an Earth observer in the northern hemisphere. Vertical departure from these locations would result in the vehicle orbiting the Earth in a trajectory similar to the Moon's orbit. The reason for this is that the speed of the departure vehicle adds to the Moon's orbital speed. To return to Earth, it is necessary that the speed of the departure vehicle subtract from the Moon's orbital speed about the Earth.

Thus, to depart from the Moon at the simple impact locations, it is necessary to rise, tilt to the right, and fly

Table 9. Differential coefficient for impact parameter, \bar{B} | Mars trajectory, 176.7 days

Differential coefficient ^a	Value	Units
$\frac{\partial \bar{B}}{\partial R}$	6.172×10^4	Meters/meter
$\frac{\partial \bar{B}}{\partial V}$	6.917×10^7	Seconds
$\frac{\partial \bar{B}}{\partial \Gamma}$	2.045×10^9	Meters/deg
$\frac{\partial \bar{B}}{\partial \theta}$	1.195×10^9	Meters/deg
$\frac{\partial \bar{B}}{\partial z}$	2.592×10^3	Meters/meter
$\frac{\partial \bar{B}}{\partial \dot{z}}$	1.441×10^6	Seconds

^aThe symbol R represents the distance from Earth's center, V the speed relative to Earth, Γ the path angle of velocity vector \bar{V} , z the cross-range, \dot{z} the cross-range rate, and θ the downrange angle subtended at Earth's center.

across the face of the Moon to the right, relative to the Earth observer; alternately, one might tilt to the left and go all the way around the back side of the Moon.

Some preliminary results have been obtained for the lunar injection velocity vector assuming launch from the impact location of a 66-hour Earth-to-Moon trajectory. It was found that a lunar injection speed of about 2450 meters/sec and a path angle (relative to the lunar local horizontal) of 10 degrees is required to return to the vicinity of Earth. Further, the plane of motion lies nearly in the plane of the Moon's motion about the Earth. The position vector (relative to the Moon) sweeps out an angle of about 130 degrees from time of launch to the time when the probe is 35,000 miles from the Moon.

4. Selenographic Coordinates

The two lunar missions likely to occur in the future are the orbiting of an instrumented spacecraft (satellite) around the Moon and the landing (soft impact) of a spacecraft on the Moon's surface. The proximity of the spacecraft to the Moon makes it advantageous to compute the craft's motion in a coordinate system centered at the Moon. A convenient system (x, y, z) is shown in Figure 57. The origin is located at the center of mass of the Moon, the x axis always points toward the vernal equinox, and the z axis remains parallel to the spin axis of the Earth. Having computed the motion of the spacecraft in this system, it would then be desirable to express this motion in terms of a coordinate system rigidly attached to the Moon—especially if a soft landing were the planned mission.

A choice of this Moon-fixed system is suggested by the gravitational potential V of the Moon, which appears in the equations of motion of the spacecraft. Observations of the lunar body over the past 100 years indicate that the Moon is a triaxial ellipsoid; i.e., the Moon has only three principal axes of inertia (the Moon is an ellipsoid, but not one of revolution). Now, the complexity of V , resulting from this configuration, can be minimized if V is expressed in a rectangular coordinate system, centered at the Moon, whose axes coincide with the Moon's principal axes. In Figure 57, x' , y' , z' represent the Moon's principal axes of inertia. The origin of this system is at the Moon's center of mass, the x' axis always (except for small variations) points toward the center of the Earth, and the z' axis lies along the rotation axis of the Moon. The potential V is therefore written $V(x', y', z')$, rather than $V(x, y, z)$, and x', y', z' is employed to describe the motion of the probe.

The transformation from x, y, z , to x', y', z' is accomplished by the three Euler angles Ω, Λ, i (Fig 57) and Ω' is measured in the Earth's equatorial plane and Λ ,

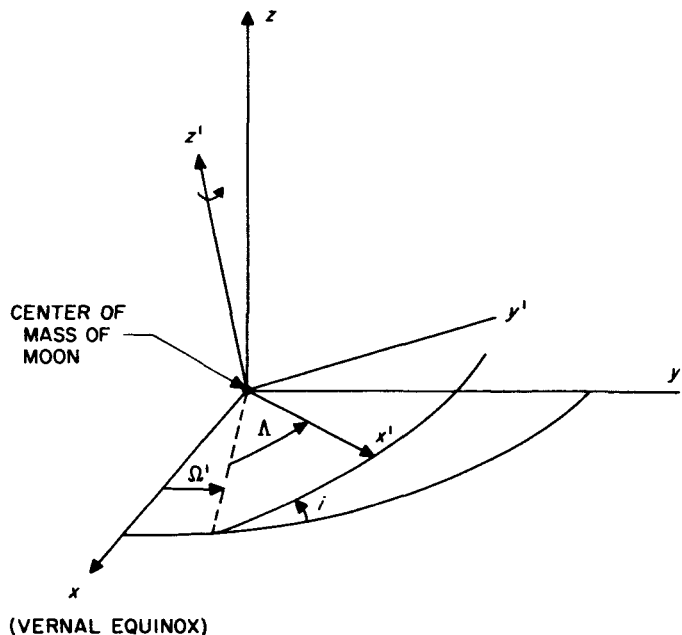


Figure 57. Definition of lunar spacecraft Euler angles Ω, Λ, i

in the Moon's. These angles are functions of analogous quantities Ω, Λ, I , defined in Figure 58. Here, the origin of the X, Y, Z system coincides with that of x', y', z' , the X axis points toward the vernal equinox and the XY plane is parallel to the ecliptic (orbital plane of the Earth). Since the (constant) angle I is small (~ 1.5 deg), Λ is measured continuously in the ecliptic and the Moon's

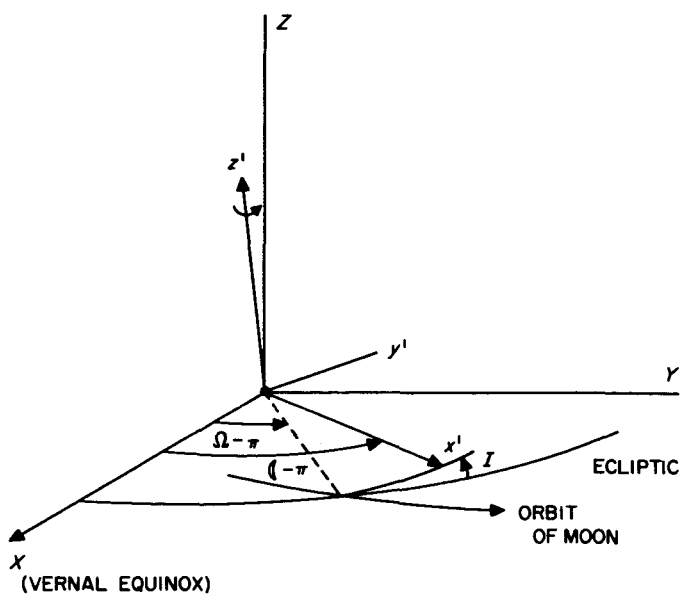


Figure 58. Definition of lunar inertial angles $\Omega', \Lambda', I (\sim 1.5$ deg)

equatorial plane. The angles ζ and ω are polynomials in time, t . A consequence of the Moon's distorted shape is that it *librates*; i.e., the x' axis does not point directly toward the center of the Earth but describes the surface of a narrow (~ 5 deg) cone in a period of a month. The angles ω , ζ , I are consequently perturbed and hence must be written $\omega + \sigma$, $\zeta + \tau$, $I + \rho$, where $\sigma(t)$, $\tau(t)$, $\rho(t)$ are the librations. The quantities σ , τ , ρ are known, periodic functions of time, where

$$|\sigma| < 1.63 \text{ degree}$$

$$|\rho| < 0.043 \text{ degree}$$

$$|\tau| < 0.025 \text{ degree}$$

Contained in the Moon's potential V are the principal moments of inertia A , B , C , about the x' , y' , z' axes, respectively. The values assigned to A , B , C can be computed from observations made of the Moon's motion. Thus, the magnitude of $(C - A)/C$ depends on the behavior of the Moon's rotation axis, $(3/2)(B - A)/Ma^2$ is a measure of the Moon's orbital motion, and $(3/2)(C/Ma^2)$ is a measure of the Moon's homogeneity. Here, M is the mass of the Moon, and a the mean radius of the Moon. From the literature:

$$\frac{C - A}{C} = 0.000629$$

$$\frac{3}{2} \frac{B - A}{Ma^2} = 0.000059$$

$$\frac{3}{2} \frac{C}{Ma^2} = 0.5956$$

Since Ma^2 is known, the above three equations can be solved for A , B , C , yielding

$$A = 8.798702364 (10^{34}) \text{ kilogram-meters}^2$$

$$B = 8.799574510 (10^{34}) \text{ kilogram-meters}^2$$

$$C = 8.804240232 (10^{34}) \text{ kilogram-meters}^2$$

Note that the two extreme values, A and C , differ by only 0.063%.

Selenographic coordinates, as described above, will be programmed on the IBM 704 digital computer, in order to compute trajectories for the lunar satellite and lunar soft impact missions.

B. Orbit Determination

Radio tracking data is used to determine the direction and magnitude of the correcting impulse for a spacecraft midcourse maneuver, and possibly for computing retro or terminal maneuvers and in interpreting scientific experiments. The radio tracking data is contaminated by random noise from many sources; for example, angle tracking data is subject to random errors caused by mechanical deformation of the tracking antennas and by receiver noise which causes jitter in the antenna servos. A digital computer program, such as the one described in SPS 2, can be used to determine the injection conditions for the orbit which fits the measured data with the least square error. These estimates of the injection conditions will differ from the injection conditions on the standard trajectory because of errors in the injection guidance. The estimates of the injection errors can be used to determine the midcourse correction. Therefore, for error analysis, it is necessary to know how accurately the space-craft orbit can be determined from measured data. A method of finding the error in orbit determination due to radio tracking errors was described in SPS 5. Some results were presented in SPS 6 and SPS 37-1. Additional results for interplanetary trajectories are described herein. Also, several related problems are discussed.

The interplanetary studies use a 114-day Venus trajectory launched in August 1962 and a 170-day Mars trajectory launched in October 1962. On the Venus trajectory, last stage burnout occurs over the South Atlantic Ocean. On the Mars trajectory, injection occurs over the Indian Ocean near the coast of Australia.

It is assumed that while the probe is on these trajectories it is tracked by a JPL (downrange-type) station at Johannesburg, South Africa, and by the Deep-Space Instrumentation Facilities receiver at Goldstone. Table 10 shows the assumed characteristics of the noise for each station. (Here, σ^2 is the mean-square value of a particular kind of noise, and T is the time interval in minutes over which the noise is assumed to be perfectly correlated.) The assumptions concerning the characteristics of the noise components are explained in more detail in SPS 6. For both stations, the high-frequency angle noise ($T < \frac{1}{6}$) is due to servo jitter. The component with $T = \frac{1}{2}$ is due to uncertainties in the atmospheric refraction correction. The very low-frequency error is due to structural deflections of the antennas. The accuracies assumed in Table 10 represent a conservative estimate of performance. It is assumed that each type of data is sampled once every 10 seconds.

Figure 59 shows the uncertainty in the miss at Venus due to radio tracking errors. The abscissa t is tracking

Table 10. Assumed noise characteristics

Station	Maximum range, miles	Type of data	σ	T, minutes
Johannesburg	50,000	Elevation angle, deg	0.1	< 0.16
			0.01	0.5
			0.1	60
		Azimuth angle, deg	Same as elevation	
		Range rate, meters/sec	1	< 0.16
		Declination, deg	0.03	< 0.16
Goldstone	$> 2 \times 10^6$	0.01	0.5	
		0.01	300	
		Hour angle, deg	Same as declination	
		Range rate, meters/sec	1	< 0.16

time measured from injection. The ordinate λ is the length of the semimajor axis of the 40% probability ellipse of miss components at closest approach to Venus. In Figure 59, Johannesburg is assumed to track from shortly after injection until the probe goes out of range at $t = 6$ hours. The data from Johannesburg reduces λ to 8600 km. Goldstone acquires the signal at $t = 11$ hours, and data taken during the first pass reduces λ to 3300 km. Data taken during the second pass over Goldstone reduces λ to 2600 km. If a midcourse maneuver is made at some time $t = t_g$, the radio tracking errors will contribute an error $\lambda(t_g)$ to the overall miss at the target. Figure 60 shows the uncertainty in the miss at Mars due to radio tracking errors. At injection on the Mars trajectory, the probe is below the horizon at Johannesburg. By the time the

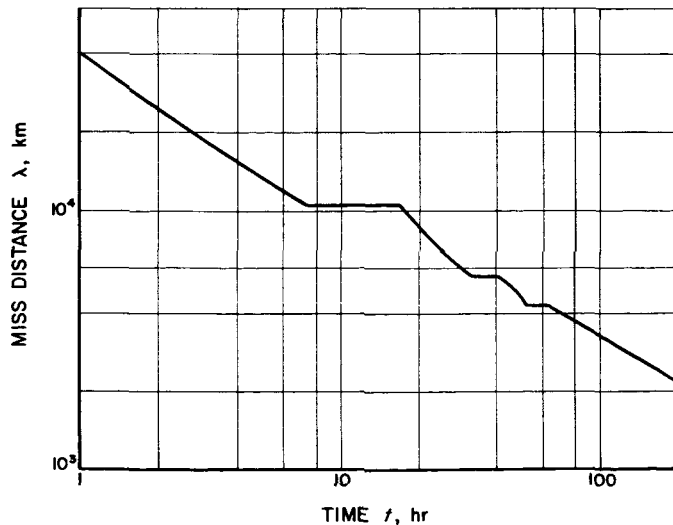


Figure 59. Miss at Venus due to radio tracking errors

probe rises above the horizon at Johannesburg, it exceeds the assumed maximum range of the downrange site. The orbit is determined entirely by Goldstone which acquires at $t = 0.5$ hour. It is likely that range data of reasonable accuracy (i.e., $\sigma = 200$ meters, $T < 0.16$ minute) may be available from Goldstone in 1962. Range data would reduce λ considerably in Figures 59 and 60. Since the midcourse maneuver will probably be made within the first few days, the curves in Figures 59 and 60 are not drawn beyond several hundred hours.

It should be noted that λ in Figures 59 and 60 represents only that part of the miss which is due to radio tracking errors. In the *Ephemeris*, the positions of the planets are tabulated in terms of astronomical units. At the present time, there is an uncertainty of 1 part in 2000 in the conversion factor from astronomical units to ordinary length units such as meters. This results in an uncertainty of 21,000 km in the miss at Venus and an uncertainty of 25,000 km in the miss at Mars when the orbit is computed from injection conditions expressed in ordinary length units. Thus, for interplanetary trajectories, the accuracy of midcourse guidance may be limited by the uncertainty in the size of the astronomical unit and not by radio tracking errors. However, it is anticipated that the uncertainty in the astronomical unit will be reduced in the near future by tracking of spacecraft and radar ranging to planets.

In performing the least-squares fit to the measured data, the computing machine will carry a limited number of significant figures. This limited precision of computation may cause the least-squares fit to deteriorate if a very large number of data points is used. In addition, for a fixed precision and machine size, the computing time

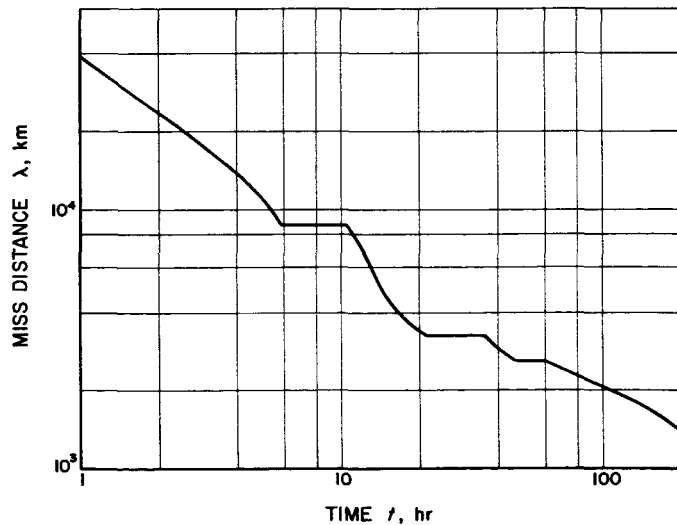


Figure 60. Miss at Mars due to radio tracking errors

interval required for a fit with a large number of data points may become inconveniently long. The total number of measurements and their spacing have a powerful effect upon the orbit determination; it is planned to investigate these effects.

It is evident from the above discussion that there are several different error sources which contribute to the overall accuracy of orbit determination. There are errors in the radio measurements, uncertainties in converting the *Ephemeris* to ordinary length units, limited accuracy in the machine computations and assumptions in the mathematical model used for the trajectory program.

and

$$\frac{V_c \cos(\gamma + \theta)}{\sin \theta} = \frac{V_h}{2} \left\{ 1 - \left[1 + \left(\frac{2a}{-R} \right) \sec^2 \frac{\theta}{2} \right]^{\frac{1}{2}} \right\} \quad (3)$$

where R is the magnitude of the position vector of the vehicle, $-a$ is the desired semimajor axis of the hyperbola, and V_h is the desired hyperbolic excess velocity of the vehicle

$$V_h = \left(\frac{GM}{-a} \right)^{\frac{1}{2}} \quad (4)$$

In order to determine the properties of the correlated velocity vector field, first the derivatives of the components of the vector field are taken with respect to the variables X , Y , Z . Omitting the details of the differentiation, the following nine derivatives are found:

$$\frac{\partial V_{cx}}{\partial X} = \frac{V_1}{R} (R_1 + S_1)(R_1 + S_1) + \frac{V_2}{R} (1 - R_1^2) \quad (5a)$$

$$\frac{\partial V_{cx}}{\partial Y} = \frac{V_1}{R} (R_1 + S_1)(R_2 + S_2) + \frac{V_2}{R} (-R_1 R_2) \quad (5b)$$

$$\frac{\partial V_{cx}}{\partial Z} = \frac{V_1}{R} (R_1 + S_1)(R_3 + S_3) + \frac{V_2}{R} (-R_1 R_3) \quad (5c)$$

$$\frac{\partial V_{cy}}{\partial X} = \frac{V_1}{R} (R_2 + S_2)(R_1 + S_1) + \frac{V_2}{R} (-R_2 R_1) \quad (5d)$$

$$\frac{\partial V_{cy}}{\partial Y} = \frac{V_1}{R} (R_2 + S_2)(R_2 + S_2) + \frac{V_2}{R} (1 - R_2^2) \quad (5e)$$

C. Systems Analysis Research

1. Interplanetary Injection Guidance

As discussed previously (SPS 3 and 5), the injection requirements of an interplanetary spacecraft may be satisfied by keeping the energy and the direction in space of the outgoing asymptote of the escape hyperbola fixed. In the analysis of injection guidance systems for space missions, it is desirable to consider a correlated velocity vector V_c as the velocity vector which would be required by the spacecraft along the powered portion of the trajectory such that if the thrust of the rocket engines were terminated at that instant, the vehicle would be capable of performing its intended mission.

a. Correlated velocity vector field. The correlated velocity vector \bar{V}_c may be thought of as a vector velocity field with components V_{cx} , V_{cy} , V_{cz} in a geocentric space-fixed, Cartesian coordinate system with unit vector \bar{I} , \bar{J} , \bar{K} having the directions of the positive X , Y , Z axes, respectively. The correlated velocity vector can be written (SPS 5) as

$$\bar{V}_c = \left[\frac{V_c \cos \gamma}{\sin \theta} \right] \bar{S} - \left[\frac{V_c \cos(\gamma + \theta)}{\sin \theta} \right] \bar{R} \quad (1)$$

where, as shown in Figure 61, \bar{S} is a unit vector in the direction of the outgoing asymptote of the desired hyperbola, \bar{R} is a unit vector in the direction of the position of the vehicle, γ is the path angle of the correlated velocity vector above the local horizontal, and θ is the angle between \bar{R} and \bar{S} .

The components of \bar{V}_c multiplying \bar{R} and \bar{S} may be expressed alternately as

$$\frac{V_c \cos \gamma}{\sin \theta} = \frac{V_h}{2} \left\{ 1 + \left[1 + \left(\frac{2a}{-R} \right) \sec^2 \frac{\theta}{2} \right]^{\frac{1}{2}} \right\} \quad (2)$$

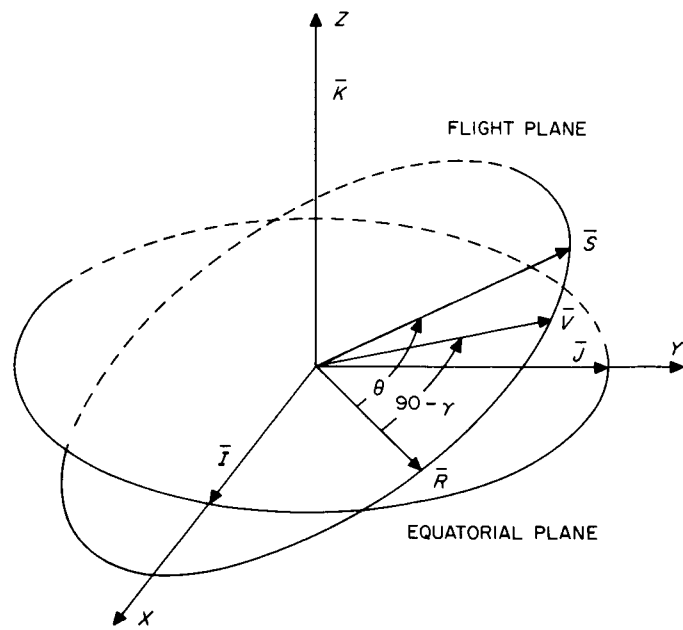


Figure 61. Orientation of unit vectors

$$\frac{\partial V_{cy}}{\partial Z} = \frac{V_1}{R} (R_2 + S_2) (R_3 + S_3) + \frac{V_2}{R} (-R_2 R_3) \quad (5f)$$

$$\frac{\partial V_{cz}}{\partial X} = \frac{V_1}{R} (R_3 + S_3) (R_1 + S_1) + \frac{V_2}{R} (-R_3 R_1) \quad (5g)$$

$$\frac{\partial V_{cz}}{\partial Y} = \frac{V_1}{R} (R_3 + S_3) (R_2 + S_2) + \frac{V_2}{R} (-R_3 R_2) \quad (5h)$$

$$\frac{\partial V_{cz}}{\partial Z} = \frac{V_1}{R} (R_3 + S_3) (R_3 + S_3) + \frac{V_2}{R} (1 - R_3^2) \quad (5i)$$

where R_1, R_2, R_3 and S_1, S_2, S_3 are the direction cosines of the unit vectors \bar{R} and \bar{S} in the X, Y, Z directions, respectively, and V_1 and V_2 are given by the following:

$$V_1 = -\frac{V_h}{2} \left\{ \frac{\left(\frac{2a}{-R}\right) \sec^4 \frac{\theta}{2}}{\left[1 + \left(\frac{2a}{-R}\right) \sec^2 \frac{\theta}{2}\right]^{\frac{1}{2}}} \right\} \quad (6a)$$

and

$$V_2 = -\frac{V_h}{2} \left\{ 1 - \left[1 + \left(\frac{2a}{-R}\right) \sec^2 \frac{\theta}{2} \right]^{\frac{1}{2}} \right\} \quad (6b)$$

Now the curl of the correlated velocity vector field is given by

$$\begin{aligned} \text{curl } \bar{V}_c &= \nabla \times \bar{V}_c = \left(\frac{\partial V_{cz}}{\partial Y} - \frac{\partial V_{cy}}{\partial Z} \right) \bar{I} + \left(\frac{\partial V_{cx}}{\partial Z} - \frac{\partial V_{cz}}{\partial X} \right) \bar{J} \\ &\quad + \left(\frac{\partial V_{cy}}{\partial X} - \frac{\partial V_{cx}}{\partial Y} \right) \bar{K} \end{aligned} \quad (7)$$

An observation of Equations (5a) to (5i) reveals the following identities

$$\frac{\partial V_{cz}}{\partial Y} = \frac{\partial V_{cy}}{\partial Z} \quad (8a)$$

$$\frac{\partial V_{cx}}{\partial Z} = \frac{\partial V_{cz}}{\partial X} \quad (8b)$$

$$\frac{\partial V_{cy}}{\partial X} = \frac{\partial V_{cx}}{\partial Y} \quad (8c)$$

such that

$$\text{curl } \bar{V}_c = \nabla \times \bar{V}_c = 0 \quad (9)$$

The curl of \bar{V}_c being zero implies a conservative field and suggests the rather interesting possibility that the correlated velocity vector can be represented as the gradient of a scalar potential function Φ ,

$$\bar{V}_c = \text{grad } \Phi = \frac{\partial \Phi}{\partial X} \bar{I} + \frac{\partial \Phi}{\partial Y} \bar{J} + \frac{\partial \Phi}{\partial Z} \bar{K} \quad (10)$$

Omitting the detailed derivation of Φ , the scalar potential function was found to be

$$\Phi = R V_h \left\{ -1 + \cos^2 \frac{\theta}{2} \left[1 + \left(1 + \left\{ \frac{2a}{-R} \right\} \sec^2 \frac{\theta}{2} \right)^{\frac{1}{2}} \right] \right. \\ \left. + \left[\frac{2a}{-R} \right] \log_e \left[\frac{1 + \left(1 + \left\{ \frac{2a}{-R} \right\} \sec^2 \frac{\theta}{2} \right)^{\frac{1}{2}}}{\left(\left\{ \frac{2a}{-R} \right\} \sec^2 \frac{\theta}{2} \right)^{\frac{1}{2}}} \right] \right\} \quad (11)$$

A graph of the equipotentials, $\Phi = \text{constant}$, are shown as dashed lines in Figure 62 as a function of R and θ . The dimensions associated with R have been normalized so that one radial unit equals $[-R/2a]$, the dimensions associated with the equipotentials being in units of $V_h (-2a)$. Several streamlines representing the paths the vehicle would follow after thrust termination are also shown as solid lines in Figure 62.

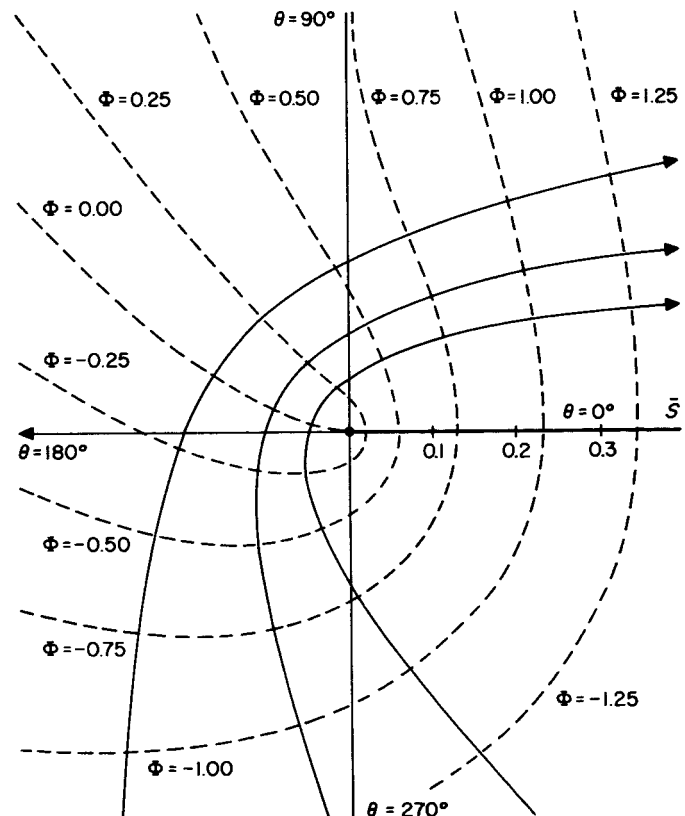


Figure 62. Lines of equipotential

The divergence of the vector field is given by

$$\operatorname{div} \vec{V}_c = \nabla^2 \Phi = \nabla \cdot \vec{V}_c = \frac{\partial V_{cx}}{\partial X} + \frac{\partial V_{cy}}{\partial Y} + \frac{\partial V_{cz}}{\partial Z} \quad (12)$$

or

$$\nabla^2 \Phi = \frac{V_h}{2R} \frac{\left\{ 1 - \left[1 + \left(\frac{2a}{-R} \right) \sec^2 \frac{\theta}{2} \right]^{\frac{1}{2}} \right\}^2}{\left[1 + \left(\frac{2a}{-R} \right) \sec^2 \frac{\theta}{2} \right]^{\frac{3}{2}}} \quad (13)$$

resulting in Poisson's equation.

D. Space Flight Studies

1. Midcourse Guidance

Midcourse guidance studies have been continuing with reference to *Agena* injected spacecraft on lunar missions. For these missions, a 66-hour trajectory has been under consideration for several reasons; (1) the vehicle would be directly over Goldstone at the time it impacts the Moon, (2) nearly-maximum payload could be attained with this trajectory, and (3) the unretarded impact speed would be near minimum.

Figure 63 shows curves of the rms magnitude of the midcourse correction vs time of application on the 66-hour trajectory for *Agena* guidance system Models I, II, and III (SPS 37-2). These curves assume that only the miss components have been adjusted and that the correction has been made in the most efficient manner; i.e., the correction has been made in the critical plane. It will be noted that these curves differ in character from those published in SPS 37-1 for the *Vega* injection guidance system (VIGS).

This change in character can be understood by examining the effect of six independent injection guidance errors on the magnitude of the midcourse correction. The results of such a study are presented graphically in Figure 64. For the *Agena* injection guidance system, the curves in Figure 63 have been determined primarily by the height y and velocity v errors at injection. The curves in Figure 64 for individual height and velocity error are increasing approximately linearly over the range considered. For the VIGS, however, there was a large contribution from the pitch angle (γ) error in addition to the height and velocity error. The curves for pitch angle in Figure 64 show a minimum, thus the magnitude of

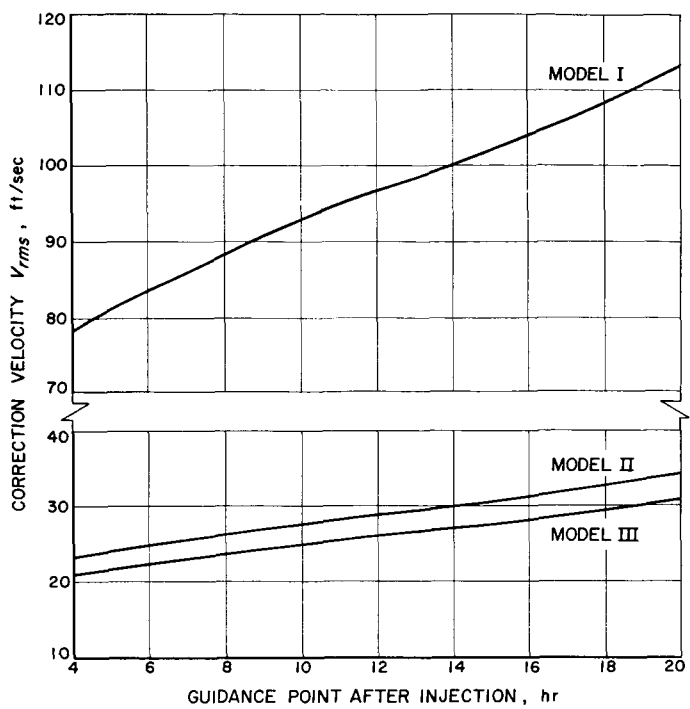


Figure 63. RMS magnitude of correction for adjusting miss-components only

the midcourse correction as a function of guidance point is approximately linear over the range presented here for the *Agena* guidance system but shows a minimum for the VIGS.

Some midcourse guidance system design figures are now available for the *Ranger III*, *IV*, and *V* lunar-impact missions. The figures given assume a midcourse maneuver 16 hours after injection on a 66-hour lunar impact trajectory. It has been determined that the *Agena* Model II guidance system will be used and that the attitude control system will have the ability to point the midcourse rocket in any desired direction. If only the miss components are adjusted and the maneuver is made in the critical plane, the minimum required speed capability to cope with 99% of the nonstandard trajectories resulting from errors in the injection guidance system is 80 ft/sec. For this case, the rms flight time variation after a midcourse maneuver is 0.27 hour. If the time of flight variation is adjusted in addition to the miss components, the minimum required speed capability is 99 ft/sec. Since the attitude control system will be able to handle both of these cases with equal effectiveness, it has been recommended that both the miss components and time of flight be adjusted with the midcourse maneuver.

Another related problem, which arises from the requirement that the biologically unsterilized *Agena* vehicle must not hit the Moon, has been studied. Two possible

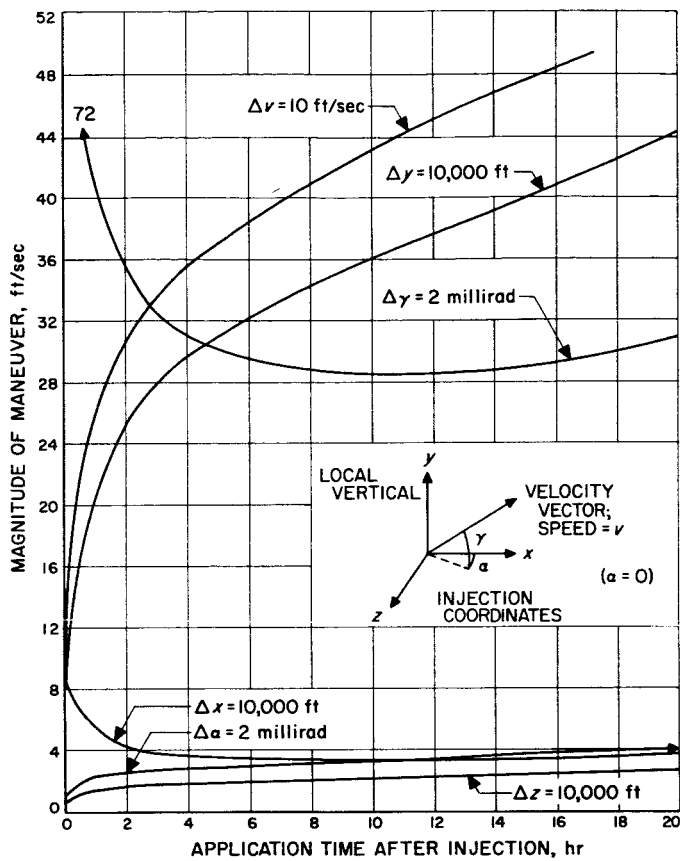


Figure 64. Midcourse maneuver to correct individual injection errors in 66-hour lunar impact trajectory

solutions have been considered. First, the standard trajectory can be designed to miss the Moon by an amount sufficient to insure that the last stage will also miss the Moon. The spacecraft is then brought back to a trajectory which impacts the desired area of the Moon by an impulse applied with the midcourse rocket. In order to avoid restarting the midcourse rocket motor, it is anticipated that this standard correction would be combined with the regular midcourse maneuver which compensates for random injection errors. The minimum required speed capability is 160 ft/sec on the 66-hour trajectory. This copes with 99% of the injection guidance errors and insures that the probability of the separated last stage hitting the Moon is less than 1%. Alternatively, the last stage and spacecraft could be injected on an impact trajectory, and after separation, the last stage could be diverted from the Moon by a small impulse. The minimum impulse which could be applied to the last stage is 30 ft/sec along the velocity vector at injection. This would give a probability of less than 1% of the last stage striking the Moon.

2. Circumlunar Navigation

Attention is being given to the problem of a circumlunar navigation vehicle, with possibility of recovery within a determinable area. Some study has been devoted to the trajectory mentioned in SPS 6, page 69, a retrograde path with closest approach approximately 1000 km above the lunar surface at latitude -7° and longitude -173° selenographic (in the SW quadrant of the unseen disk). A conceivable method of guidance would consist of two maneuvers, the first near the peak of the initial Goldstone visibility period (approximately 16 hr after injection), and the second on the Earthbound stretch and outside the appreciable lunar sphere of influence (approximately 80 hr after injection). Current investigation is concentrated at determination of computer integration step-size interval which would provide reasonable accuracy for the calculation of miss coefficients of geographic latitude and longitude with respect to conditions at first maneuver termination.

3. Self-Contained Terminal Guidance

In performing the terminal guidance function, it is anticipated that velocity corrections would be made at discrete, predetermined distances from the destination planet. Each required velocity correction vector would be determined by the spaceborne computer on the basis of a combination of celestial, timer, accelerometer and prior radar (deep space net) data, all of which serve to establish the approach trajectory of the spacecraft relative to the destination planet prior to the correction. The celestial data is obtained from a series of fixes which involve sightings of the angle between lines to the destination planet and each of two other reference stars (one of which could conceivably be the Sun). A measurement of the planetary angular diameter is also made. Since these fixes are all performed at predetermined instants, timer information enters the picture as well. From the above data, plus knowledge of any previous maneuvers and possibly supplementary tracking data, predictions of the dispersion in the terminal miss components can be made.

In making the computation of the velocity correction, each of the various measurements or predictions above is expressed as the difference between the measured and standard value of the quantity concerned. The estimated terminal dispersion can then be expressed as a weighted sum of these different terms, through the use of a smoothing process involving the maximum-likelihood principle. The velocity correction is then computed as that required to null out this dispersion.

Recent attention has centered on developing the equations (for use in designing the spaceborne computer) that will express the velocity components of the maneuvers directly in terms of the measured data.

To obtain a preliminary estimate of what terminal guidance accuracy might eventually be expected, a simplified case was investigated involving two velocity corrections, with one celestial fix per correction. Each fix involved the measurement of three angles. These consisted of the angles between lines to the destination planet and each of two reference stars plus the measurement of the planetary angular diameter. The results for approaches to Mars and Venus are given in Table 11. An initial rms asymptote dispersion of 5000 miles was assumed for Mars in each of the two directions of miss and 4000 miles for Venus. A relative approach velocity of 23,000 ft/sec was assumed in each case. It was assumed that half the fuel would be used in making each correction and that there would be sufficient fuel on board to cope with 95% of all cases. In the table, μ stands for the fraction of total vehicle weight allotted for fuel in making corrections, r_k for the distance from the destination planet at which each of the two corrections was made, $\sigma \theta_f$ for the rms accuracy of angular measurement for each of

the two fixes (the accuracy of all three angular measurements was assumed equal for any one fix), and σr_{ay} for the rms dispersion of the asymptote in one of the two directions of miss after each correction. The dispersions were assumed equal in each of the two directions.

Table 11. Estimates of terminal guidance accuracy

Planet	μ	$r_k, \text{miles} \times 10^4$	$\sigma \theta_f, \text{radians} \times 10^{-4}$	$\sigma r_{ay}, \text{miles}$
Mars	0.025	320 110	3.3 3.3	1650 390
	0.05	160 27	3.3 7.5	820 210
	0.10	82 7.7	3.7 10	470 77
	0.20	41 3.2	6.1 13	390 42
	0.025	260 64	3.3 4.3	970 280
	0.05	130 16	3.3 9.0	480 140
	0.10	66 5.4	4.4 14	330 77
	0.20	33 1.8	6.6 43	220 77

E. Powered Flight Studies

1. Elementary Injection Guidance Systems

In SPS 37-1, the *Vega* guidance system analysis was terminated with a discussion of errors at the Moon which result from various perturbations. A subsequent study was made for other more elementary guidance methods in order to evaluate their accuracy. These results have been compared with VIGS. In making this comparison, two lunar trajectories with significantly different flight times were selected. The *fast* lunar trajectory was a 36-hour direct-ascent trajectory having a 5-second coasting period between second-stage burnout and third-stage ignition, whereas the *slow* lunar was a 63-hour trajectory with a 619.56-second coasting period before third-stage ignition.

The following basic guidance schemes, beginning with the least sophisticated and extending to a more inclusive guidance system, were simulated on the two-dimensional JPL guidance study program: (1) Sustainer shut off at standard measured axial velocity by body-fixed accelerometer; second and/or third stages shut off by fuel depletion. (2) Sustainer, second, and third stages shut off at standard measured axial velocity by body-fixed accelerometer. (3) Radio monitoring system which mechanizes target miss components in order to shut off sustainer at the optimum time, but which cannot command angular changes about the missile cg; second and third stages are shut off as in (2). (4) Radio command guidance system which can monitor and control flight parameters sufficiently well so that only small deviations from the equivalent of a standard trajectory exist at second-stage ignition; second and third stages are shut off as in (2). (5) The last guidance scheme is the former *Vega* injection guidance system, described in SPS 37-1.

All stages are flown on autopilot to control missile attitude in Schemes (1) to (3) and, in the radio guidance case, there is the facility to send commands to the missile autopilot so that control of motion about the cg may be accomplished during the *Atlas* portion of flight. In all of the above schemes, the *Atlas* booster is shut off when a predetermined acceleration level is reached. Note that System (5) uses an autopilot programmer to send turning commands to the vehicle autopilot.

For the elementary guidance Systems (1) to (4), integrators were not cleared for either the fast or slow lunar trajectories. This would be acceptable for direct ascent and short-coast trajectories; however, for the longer coasting type, integrators would probably be cleared so that component errors do not build up large coordinate deviations.

2. Perturbations

Variations in propellant flow rate, specific impulse, and thrust attitude were applied during the powered flight portions of the fast and slow lunar standard trajectories to test the various guidance methods. On all perturbed trajectories, second and third stages were ignited at the standard master time from launch as it was discovered that local time ignition (ignition of given stage at a fixed time after burnout of the previous stage) gave rise to much larger miss components at the Moon.

The following assumptions were made: Fuel depletion was interpreted as a shutoff when the standard propellant weight had been consumed. For this reason, Schemes (1) and (2) shut stages off at the same time when the perturbations are propellant flow rate errors which follow a standard booster. It was assumed that radio monitoring could, in fact, mechanize miss components at the Moon so that the optimum time to shut off the sustainer could be chosen. Finally, it was assumed that the radio command guidance scheme was able to maintain the missile essentially along the equivalent of a standard trajectory through sustainer burnout.

Variations in specific impulse cause large velocity errors when the perturbed stage is shut off by fuel depletion. Specific impulse variations in second stage of the fast lunar trajectory, with second stage shutoff by fuel depletion and velocity shutoff of the third stage, do not produce nearly as large a lunar miss as would be caused by specific impulse variations in third stage, with shutoff caused by fuel depletion of the third stage. For lunar trajectories with long coasts between second and third stages and, if integrators are cleared, specific impulse variations in second stage with fuel depletion shutoff would perpetuate through third stage and cause very large deviations.

Guidance Scheme (2) should be thought of as the representative elementary guidance method and, as such, it is interesting to note its ability to handle various perturbations as compared with Scheme (5). Table 12 gives the $|B|$ for several perturbations for both fast and slow lunar trajectories. Note that B is analogous to the impact parameter vector used in the Rutherford scattering theory. It therefore really indicates miss distance at a massless Moon.

In general, a given perturbation produces a greater miss at the Moon when applied to the slow lunar trajectory, since the differential miss coefficients are larger for lower-energy trajectories. According to calculations made for the *Vega* injection guidance system, it is very interesting and relevant to note that component errors alone produce very large deviations; for a 36-hour lunar

trajectory the approximate 1σ miss at the Moon is 1500 kilometers and, for trajectories having flight times near 60 to 70 hours, the 1σ miss is 15,000 kilometers.

3. Conclusions

Component errors can produce injection deviations and lunar misses which significantly dwarf those produced by the perturbations considered in this study.

Assuming that elementary guidance system component errors cause coordinate deviations of approximately the same magnitude as those caused by component errors of the VIGS, it would then appear acceptable to employ a simpler guidance scheme, such as System (2), in combination with a midcourse maneuver, for lunar trajectories, until such time as more advanced guidance systems have been incorporated into future vehicles.

Table 12. Comparison of Systems 2 and 5

Trajectory	Standard booster, sustainer, and 3rd stage; 3σ propellant flow rate variation in 2nd stage of 2%		Standard 2nd and 3rd stages; 3σ propellant flow rate variations in booster and sustainer of 2%		Standard booster and sustainer; 3σ specific impulse variation 1.5% in 2nd stage engine (slow lunar); 1.3% in 3rd stage engine (fast lunar)		Standard booster and sustainer; 3σ thrust attitude errors in both 2nd and 3rd stages of 0.5%	
	System 2	System 5	System 2	System 5	System 2	System 5	System 2	System 5
Fast lunar $ \vec{\delta} $, km	680	510	3230	1400	310	45	2630	160
Slow lunar $ \vec{\delta} $, km	1835	1065	7765	1370	960	550	8335	6060

IV. SPACECRAFT GUIDANCE AND CONTROL TECHNIQUES

A. Spacecraft Attitude Sensing Techniques

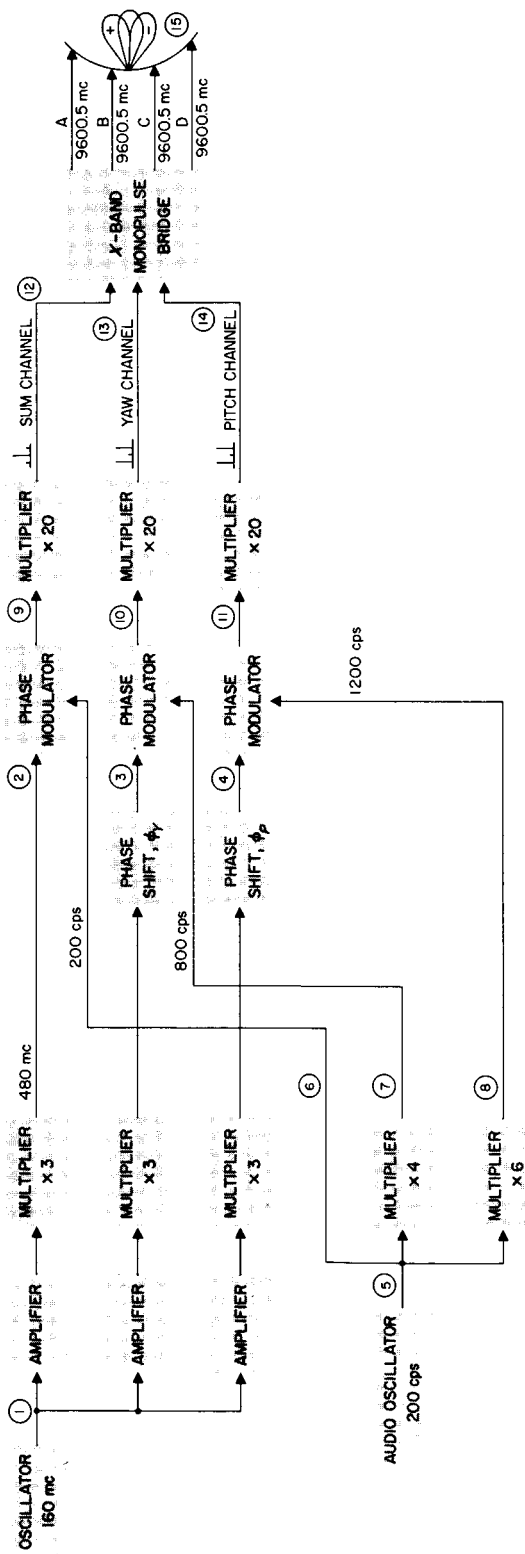
As described in *RS 36-1*, an experimental research effort is in progress to study and to test in the laboratory advanced techniques for attitude sensing of a spacecraft. This effort will supply concepts and techniques which may, in the future, apply to the development of specific spacecraft attitude control systems. The general category of attitude sensing systems being studied is that in which radio frequency signals are used for sensing. The specific system currently under investigation utilizes a transmitting monopulse antenna with modulation coded beams. The model, or vehicle simulator, which will support the antenna and transmitter electronics was described in *RS 36-1*. The simulator has dimensions on the order of 2 feet, weighs about 50 pounds, and is supported on an extremely low friction spherical gas bearing.

1. Electronic System

The simulated spacecraft and ground station electronic system block diagrams are shown in Figures 65 and 66, respectively. The individual components making up the system were described in detail in *RS 36-1*.

As shown in Figure 65, the transmitter has three phase-coherent outputs at 9600.5-mc frequency. The RF signal is independently adjustable in phase and amplitude in each channel. In addition, each channel is independently phase modulated by coherently related audio signals, the phase and amplitude of which are adjustable. The three transmitter signals are fed into the sum and two error outputs of a conventional amplitude-comparison monopulse type of parabolic antenna. Each of this antenna's three beams is distinctive by virtue of its particular audio modulation. The vehicle signal waveforms at various points in the transmitter are shown in Figure 65.

The receiving (ground) system is shown in Figure 66. The receiver is a double-superheterodyne phase-lock-loop receiver, described in *RS 36-1*. The receiver phase detector provides the audio modulation signals which after amplification are fed into the audio angle detector. The relative amplitude of the error channel audio modulation signals (800 and 1200 cps) is proportional to the pointing error, or attitude, of the monopulse antenna. The plus-or-minus error ambiguity is resolved by the phase relationship between the received sum and error channel audio signals. As shown in Figure 66, the relative modulation outputs are compared by means of an audio lock loop for the sum channel and two phase-coherent amplitude detectors for the error channels. The final audio angle detector outputs are fed into a filtering and display



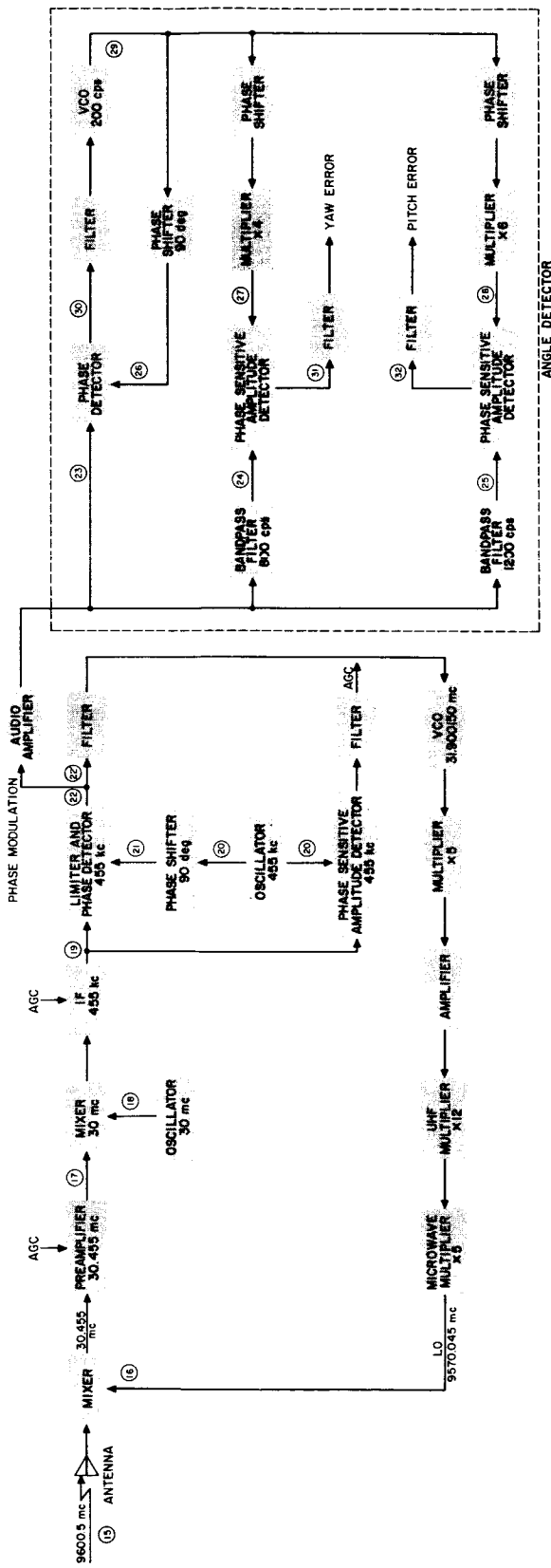
Nominal system equations
for transmitter

- (1) $\cos \omega_0 t$
- (2) $\cos 2 \omega_0 t$
- (3) $\alpha r \cos (3 \omega_0 t + \phi_r)$
- (4) $\alpha p \cos (3 \omega_0 t + \phi_p)$
- (5) $\sin \omega_m t$
- (6) $\sin \omega_m t$
- (7) $\sin n_r (\omega_m t + \phi_{m,r})$
- (8) $\sin n_p (\omega_m t + \phi_{m,p})$
- (9) $\cos [3 \omega_0 t + \beta_s \sin \omega_m t]$
- (10) $\alpha r \cos [3 \omega_0 t + \phi_r + \beta_r \sin n_r (\omega_m t + \phi_{m,r})]$
- (11) $\alpha p \cos [3 \omega_0 t + \phi_p + \beta_p \sin n_p (\omega_m t + \phi_{m,p})]$
- (12) $\cos [60 \omega_0 t + 20 \beta_s \sin n_s \omega_m t]$
- (13) $\alpha r \cos [60 \omega_0 t + 20 \phi_r + 20 \beta_r \sin n_r (\omega_m t + \phi_{m,r})]$
 $\times \cos [60 \omega_0 t + 20 \phi_p + 20 \beta_p \sin n_p (\omega_m t + \phi_{m,p})]$
- (14) $\alpha r \cos [60 \omega_0 t + 20 \beta_s \sin \omega_m t] + \alpha r \eta_r \sin \frac{\pi}{2} \left(\frac{\theta_r}{\theta_{0r}} \right)$
 $+ \alpha p \eta_p \sin \frac{\pi}{2} \left(\frac{\theta_p}{\theta_{0p}} \right) \cos [60 \omega_0 t + 20 \theta_p]$
 $+ 20 \beta_p \sin n_p (\omega_m t + \phi_{m,p})]$

Definition of symbols used in transmitter equations

Symbol	Definition	Definition	Nominal value
ω_0	Angular frequency, RF oscillator, rad/sec		$2\pi \times 1.6 \times 10^8$
ω_m	Angular frequency, audio oscillator, rad/sec		$2\pi \times 2.0 \times 10^2$
α_r	Yaw channel voltage relative to sum channel		0.50
α_p	Pitch channel voltage relative to sum channel		0.50
ϕ_r	Yaw channel RF static phase relative to sum channel		0
ϕ_p	Pitch channel RF static phase relative to sum channel		0
$\phi_{m,r}$	Yaw channel audio phase relative to sum channel		0
$\phi_{m,p}$	Pitch channel audio phase relative to sum channel		0
n_r	Yaw channel multiplication factor		4
n_p	Pitch channel multiplication factor		6
$20 \beta_s$	Sum channel phase modulation index, rad (approx)		0.5
$20 \beta_y$	Yaw channel phase modulation index, rad		2.4
$20 \beta_p$	Pitch channel phase modulation index, rad		2.4
η_r	Yaw channel pattern maximum relative to sum		0.7
η_p	Pitch channel pattern maximum relative to sum		0.7
$2 \theta_{0y}$	Yaw channel error peak separation, deg		18
$2 \theta_{0p}$	Pitch channel error peak separation, deg		18
θ_r	Yaw pointing error, deg		< 0.3
θ_p	Pitch pointing error, deg		< 0.3

Figure 65. Transmitter for simulated spacecraft attitude sensor signals


Nominal system equations for receiver

$$\begin{aligned}
 & \textcircled{15} \cos [60 \omega_{st} + \Phi_s^*(t)] + \delta (\theta_P) \cos [60 \omega_{st} + \Phi_Y(t)] \\
 & + \delta (\theta_P) \cos [60 \omega_{st} + \Phi^*(t)] \\
 & \textcircled{16} \cos [\omega_{LI} t + \Phi^*(t)] \\
 & + \cos [\omega_{LI} t + \Phi_S(t) - \Phi^*(t)] \\
 & + \delta (\theta_Y) \cos [\omega_{LI} t + \Phi_Y(t) - \Phi^*(t)] \\
 & + \delta (\theta_P) \cos [\omega_{LI} t + \Phi_P(t) - \Phi^*(t)] \\
 & \textcircled{17} \cos \omega_{st} \\
 & \textcircled{18} \cos [\omega_{st} + \Phi_S(t) - \Phi^*(t)] \\
 & + \delta (\theta_Y) \cos [\omega_{st} + \Phi_Y(t) - \Phi^*(t)] \\
 & + \delta (\theta_P) \cos [\omega_{st} + \Phi_P(t) - \Phi^*(t)] \\
 & \textcircled{19} \cos \omega_{st} \\
 & \textcircled{20} \sin [\Phi^*(t) - \Phi_Y(t)] + \delta (\theta_Y) \sin [\Phi^*(t) - \Phi_Y(t)] \\
 & + \delta (\theta_P) \sin [\Phi^*(t) - \Phi_P(t)] \\
 & \textcircled{21} J_0 (20 \beta_s) \sin \Phi^*(t) \\
 & + J_0 (20 \beta_Y) \delta (\theta_Y) \sin [\Phi^*(t) + 20 \phi_Y] \\
 & + J_0 (20 \beta_P) \delta (\theta_P) \sin [\Phi^*(t) + 20 \phi_P] \\
 & \text{(audio components not included)} \\
 & \textcircled{22} J_1 (20 \beta_s) \cos [\Phi^*(t)] \sin \omega_{st} \\
 & J_1 (20 \beta_Y) \cos [\Phi^*(t) + 20 \phi_Y] \sin n_Y (\omega_{st} + \phi_{mY}) \\
 & J_1 (20 \beta_P) \cos [\Phi^*(t) + 20 \phi_P] \times \sin n_P (\omega_{st} + \phi_{mP}) \delta (\theta_P) \\
 & \textcircled{23} \cos [\omega_{st} + \Phi_A^*(t)] \\
 & \textcircled{24} \sin n_Y [\omega_{st} + \phi_{mY} + \Phi_A^*(t)] \\
 & \textcircled{25} \sin n_P [\omega_{st} + \phi_{mP} + \Phi_A^*(t)] \\
 & \textcircled{26} \sin [\omega_{st} + \Phi_A^*(t)] \\
 & - J_1 (20 \beta_s) \cos \Phi^*(t) \sin \Phi_A^*(t) \\
 & \textcircled{27} J_1 (20 \beta_Y) \cos [\Phi^*(t) + \phi_Y] \cos n_Y \Phi_A^*(t) \delta (\theta_Y) \\
 & \textcircled{28} J_1 (20 \beta_P) \cos [\Phi^*(t) + \phi_P] \cos n_P \Phi_A^*(t) \delta (\theta_P)
 \end{aligned}$$
Definition of symbols used in receiver equations

Symbol	Definition	Nominal value
$\delta (\theta_Y)$	Yaw error voltage $\equiv \alpha_Y n_Y \sin \frac{\pi}{2} \left(\frac{\theta_Y}{\theta_{oy}} \right)$	< 0.01
$\delta (\theta_P)$	Pitch error voltage $\equiv \alpha_P n_P \sin \frac{\pi}{2} \left(\frac{\theta_P}{\theta_{op}} \right)$	< 0.01
$\Phi_s(t)$	$20 \beta_s \sin \omega_{st}$	
$\Phi_Y(t)$	$20 \theta_Y + 20 \beta_Y \sin \dot{\theta}_Y (\omega_{st} + \phi_{mY})$	
$\Phi_P(t)$	$20 \phi_P + 20 \beta_P \sin \eta_P (\omega_{st} + \phi_{mP})$	
$\Phi^*(t)$	RF loop response, rad	0
$\Phi_A(t)$	Audio loop response, rad	0
ω_{L1}	1st LO angular frequency, rad/sec	$2\pi \times 9.5705 \times 10^9$
ω_{L2}	2nd LO angular frequency, rad/sec	$2\pi \times 2.9545 \times 10^9$
ω_{I1}	1st IF angular frequency, rad/sec	$2\pi \times 3.000 \times 10^7$
ω_{I2}	2nd IF angular frequency, rad/sec	$2\pi \times 4.55 \times 10^5$
$J_0 (20 \beta_s)$	Zero-order Bessel function of 20 β_s	0.9
$J_0 (20 \beta_Y)$	Zero-order Bessel function of 20 β_Y	0
$J_0 (20 \beta_P)$	Zero-order Bessel function of 20 β_P	0
$J_1 (20 \beta_s)$	First-order Bessel function of 20 β_s	0.3
$J_1 (20 \beta_Y)$	First-order Bessel function of 20 β_Y	0.5
$J_1 (20 \beta_P)$	First-order Bessel function of 20 β_P	0.5
ϕ'_{mY}	Yaw channel audio phase shifter error	0
ϕ'_{mP}	Pitch channel audio phase shifter error	0

Figure 66. Ground receiver for simulated spacecraft attitude sensor signals

system which, by means of meters, displays angle error and angle error rate. The error rate is obtained by differentiating the error signals. Adjustments are provided for varying the filtering time constant.

The complete system depicted in Figures 65 and 66, plus display unit, has been assembled and is presently undergoing system tests. In general, system performance is satisfactory. The monopulse antenna being used has an error peak separation of about 15 degrees. The system design goal was to maintain a sensing accuracy of 0.2 to 0.3 degree. This is presently being achieved in system tests, only however, by maintaining the error channel signal strength comparable to that in the sum channel. Since high error channel power is wasteful from a communications standpoint, tracking performance is presently being worked on with the objective of reducing the error channel power while maintaining the desired tracking accuracy. In addition, tests will be performed to determine the tracking accuracy sensitivity to various system misalignments.

2. Mechanical Component Development

A description of the spacecraft simulator with a mass-transfer actuator for attitude control has been given in the preceding *Research Summary* (Vol I). Photographs of this simulator on which some preliminary experiments were carried out are shown in Figure 67.

a. Gas-lubricated spherical bearing. The 4-inch-diameter sphere used as a support for the cast aluminum platform (Fig 67) was made from 410 stainless steel, chrome plated, and lapped to a high polish. The socket for the sphere was made from the same material but was not chrome plated. The flow rates for the unloaded platform were measured with a Fisher and Porter Tri-flat flowmeter; the results are shown plotted in Figure 68. It may be mentioned here that the feed orifice diameter is 0.0045 inch. The gap height or film thickness was measured, with a Johannsen Minikater dial gage, as a function of the plenum pressure (Fig 69).

The closure load was obtained by loading the platform with lead billets and reducing the plenum pressure until electrical contact was made between the ball and socket. Figure 70 shows a plot of the load-carrying capacity as a function of the plenum pressure and also the load per square inch of projected area of the effective spherical surface carrying the load. The results are in good agreement with the predicted performance.

b. Moment of inertia. In order to study the effects of an applied torque to the platform, it is necessary to

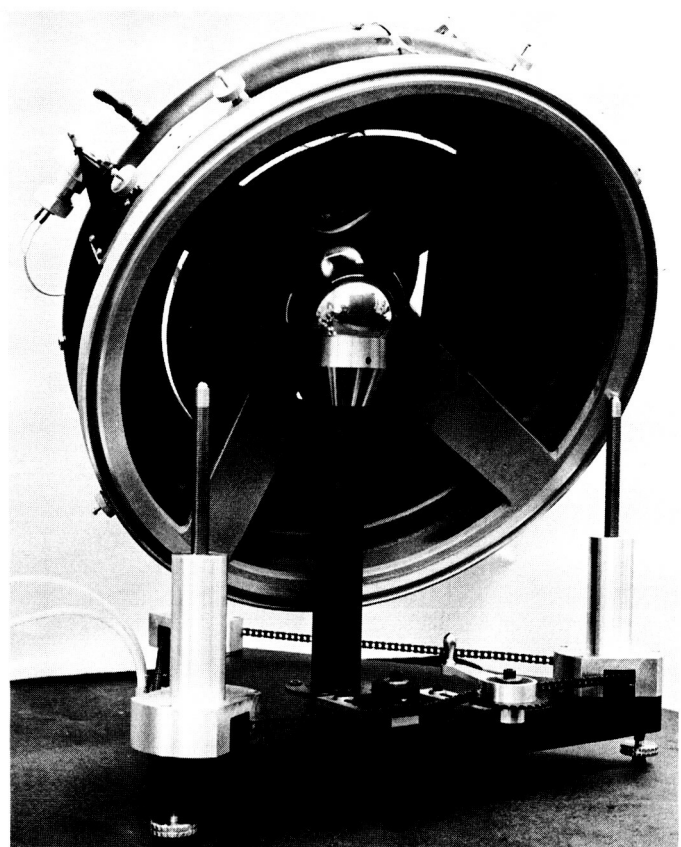
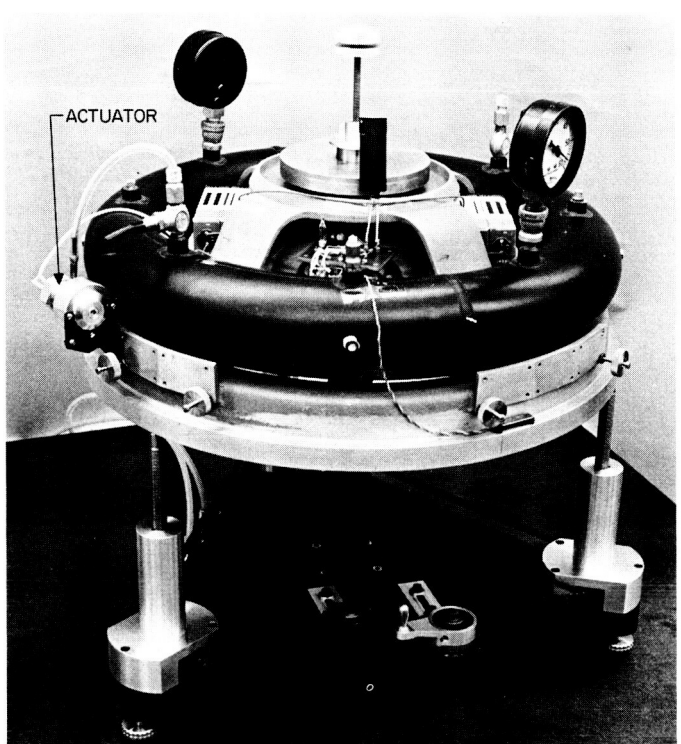


Figure 67. Spacecraft attitude-sensing simulator supported on spherical gas bearing

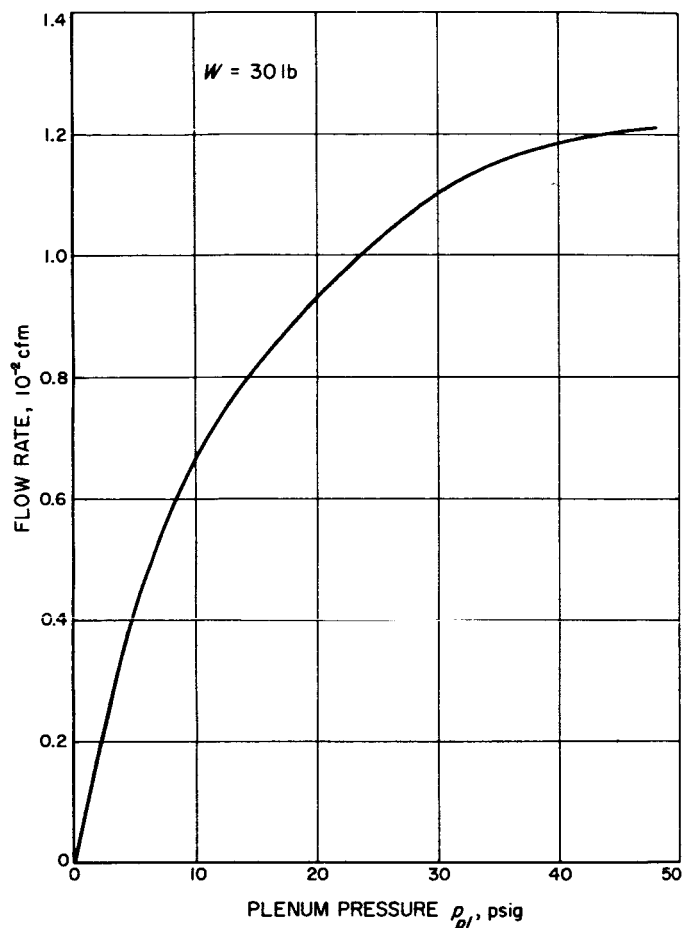


Figure 68. Flow rate of 4-inch spherical bearing vs plenum pressure

determine the moment of inertia of the movable system. With the platform in a horizontal plane, the moment of inertia was determined about the vertical axis and about the horizontal axis. The method used was to attach to the platform, on the axis, a torsion element of known spring constant, apply a torque, and time the period of oscillation.

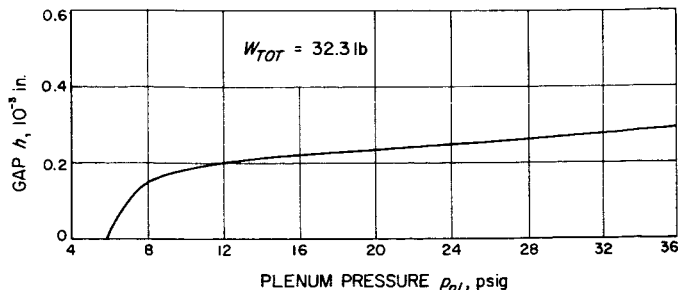


Figure 69. Gap height of 4-inch spherical bearing vs plenum pressure

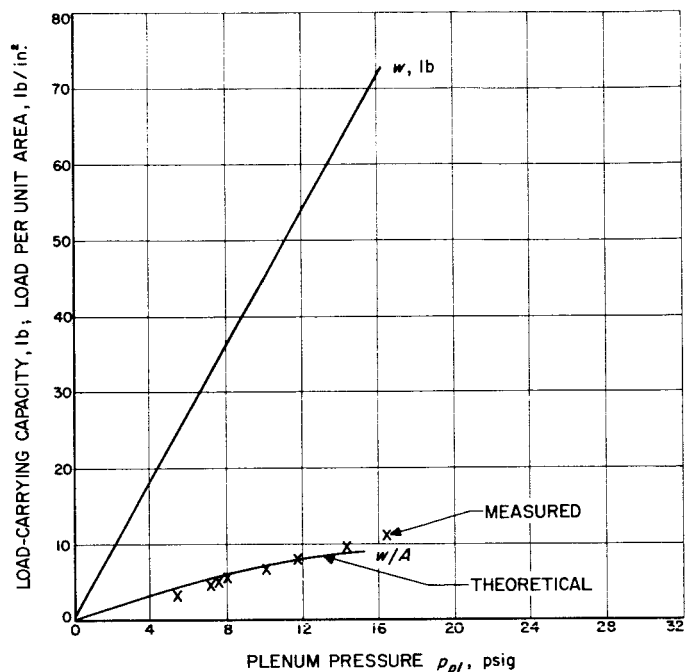


Figure 70. Load-carrying capacity of 4-inch spherical bearing vs plenum pressure

tion. The moment of inertia I can then be calculated from the equation:

$$I = \frac{K T^2}{4 \pi^2}$$

where T is the time in seconds, and K the spring constant in torsion of the torsion element. The measured moment of inertia for the unloaded platform is 2600 gm-cm^2 about the vertical axis and 1650 gm-cm^2 about a horizontal axis.

c. **Turbine torque.** In order to measure the inherent bearing torque, which is an unwanted torque produced by machining imperfections, the platform must be balanced carefully. It was noticed that, from a position at rest, the platform had a tendency to oscillate slowly. This was proven to be caused by an imbalance. To eliminate the effects of imbalance, the platform was given a spin of about 0.7 rad/sec and the rate of decay measured. The same procedure was followed again with the platform given a counterspin. The results were plotted as shown in Figure 71. Inasmuch as the aerodynamic drag of the platform and the viscous shear of the gaseous lubricant are the same in both directions, the deviation of the two curves is proportional to the turbine torque. Further tests are now in progress; the turbine torque appears slight. The lubricant scavenging system incorporated in the design of the bearing proved to be quite satisfactory.

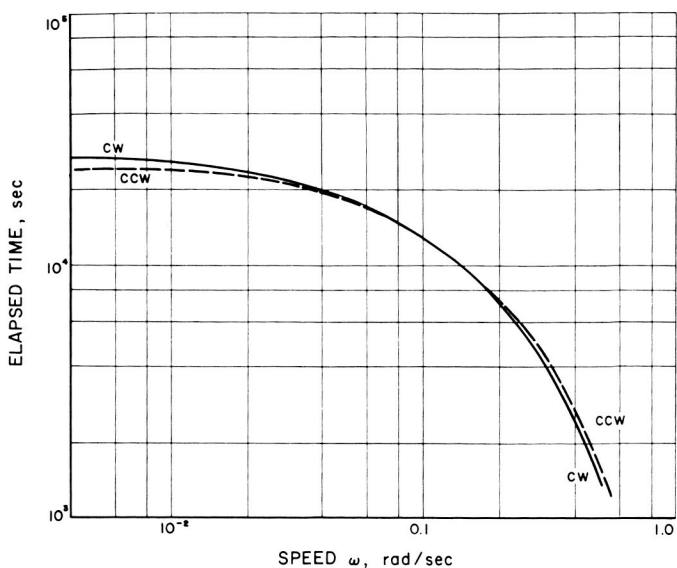


Figure 71. Decay rate of 4-inch spherical bearing

Even without a vacuum pump, the system removed 97% of the exhaust gas.

d. Mass transfer valve. The pulse type actuator previously described in RS 36-1 has now been assembled and is operating satisfactorily within the pressure range of 30 to 70 psig. The actual thrust delivered by the nozzle has not yet been determined. The energy required to operate the solenoid of the valve is approximately 0.1 watt-sec.

B. Low-Noise Amplifier Studies

1. Parametric Amplifier

A cavity type negative resistance parametric amplifier has been constructed to operate at 960 mc. The amplifier is operated in the degenerate mode; i.e., the signal and idle frequencies are nearly identical. The pump frequency is 1920 mc.

A drawing of the amplifier is shown in Figure 72. The low-impedance cavity allows the Hughes Diode 2810, which has a static capacity of about $10 \mu\mu f$ (depending on the bias), to be connected directly across the cavity.

The system noise figure was measured as shown in Figure 73 with an accuracy of about ± 0.25 db. The bias

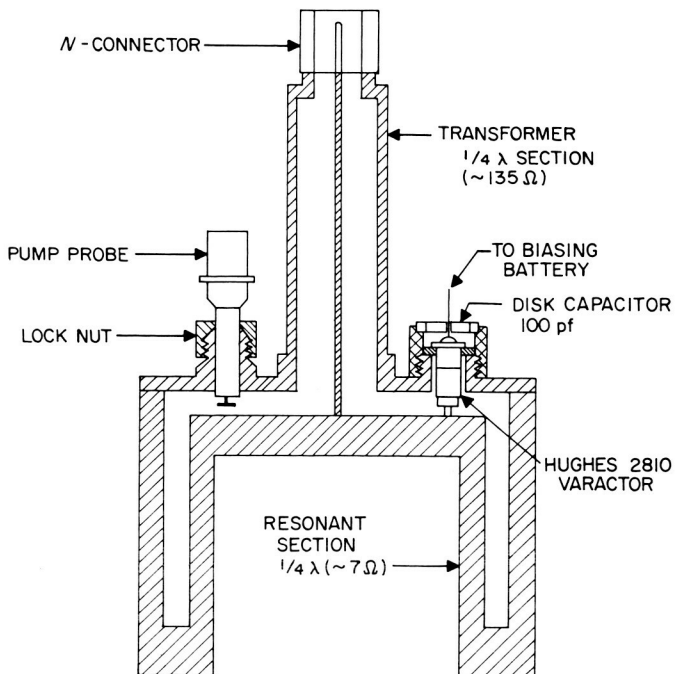


Figure 72. Construction details of 960-mc negative resistance parametric amplifier

is adjusted for minimum noise figure (approx 0.5 volt). The parametric amplifier was cooled with liquid nitrogen, and the noise figure vs temperature measured as shown in Figure 74. The 1-db noise figure measured at $-196^\circ C$ is equivalent to a noise temperature of $77^\circ K$. The RF amplifier following the parametric amplifier has a noise figure of 7 db. The parametric amplifier was operated with a gain of 18 db for the noise figure measurements

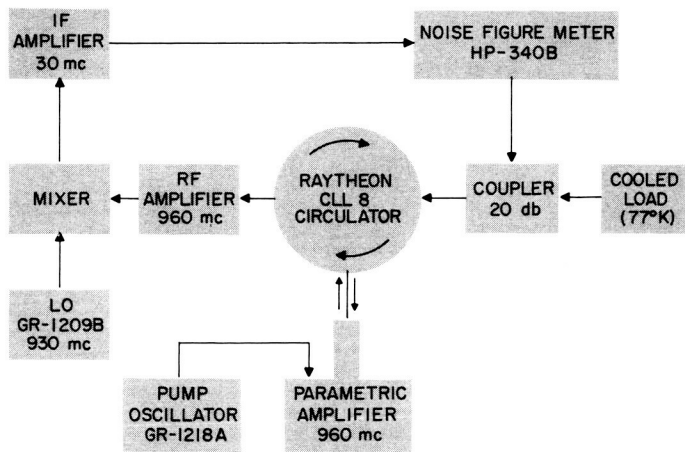


Figure 73. Parametric amplifier and associated equipment used in noise figure measurement

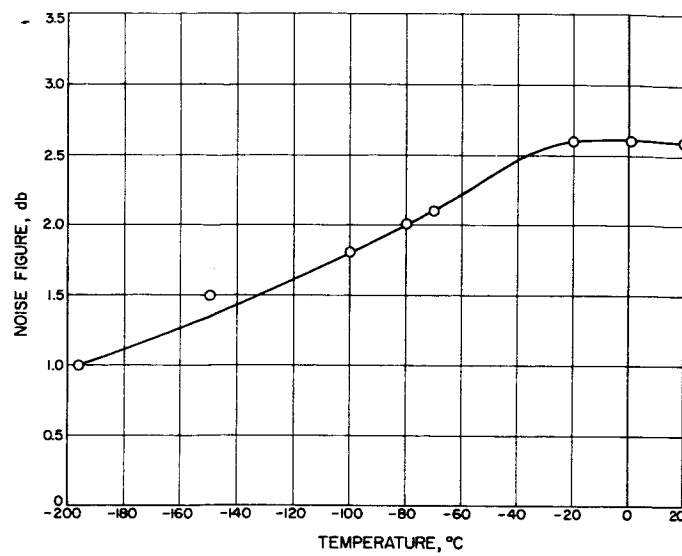


Figure 74. Parametric amplifier system noise figure vs amplifier temperature

so that the temperature of only the circulator and parametric amplifier should be approximately

$$290 \left[\left(1.26 - \frac{5.1}{63} \right) - 1 \right] = 58^{\circ}\text{K}$$

Since losses in the circulator contribute about 11°K , the noise temperature of the parametric amplifier alone is indicated to be $58^{\circ} - 11^{\circ} = 47^{\circ}\text{K}$.

Since the parametric amplifier is operated in the degenerate mode, the overall system noise temperature for normal coherent signal operation with an antenna temperature of 40°K would be $2(40 + 77) = 234^{\circ}\text{K}$. For radio astronomy use, the overall system noise temperature would be $77 + 40 = 117^{\circ}\text{K}$. With 18 db gain, the bandwidth is 5 mc.

2. Solid State Maser

Preliminary design of a maser for the Goldstone antenna has been completed and tested. The design is unique in its extreme simplicity and lends itself to ruggedization.

As shown in Figure 75, the ruby maser consists of a quarter-wave resonant cavity at the end of a coaxial transmission line. The coupling between the cavity and the coaxial cable is adjustable by means of linear motion of the center conductor; moreover, this will be the only motion allowed in the structure. This adjustment allows one to control the gain and bandwidth of the amplifier as well as the frequency center of amplification. Actu-

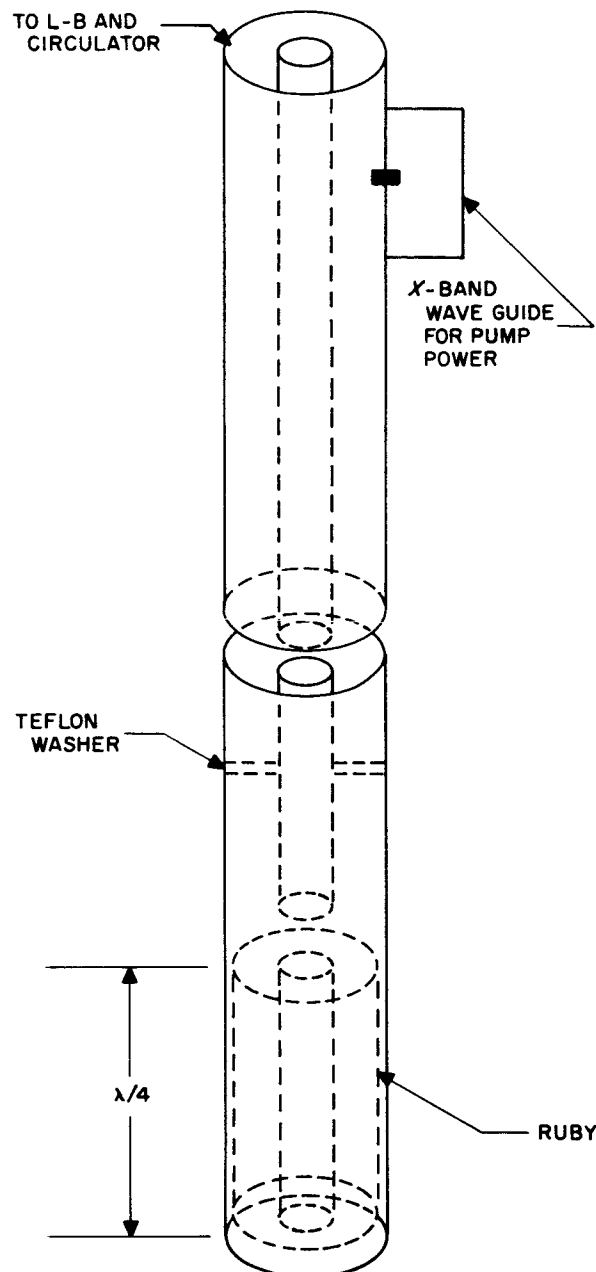


Figure 75. Solid state maser for Goldstone station

ally the amount of frequency tuning required is sufficiently small that it may be realized by a simple change in the magnetic field. The coaxial line also carries the X-band pump power in the TE_{11} mode.

The laboratory test model was found to have good gain stability at around 20 db of gain, and the bandwidth at this gain was 600 kc. The noise temperature for the system was measured as shown in Figure 76, and

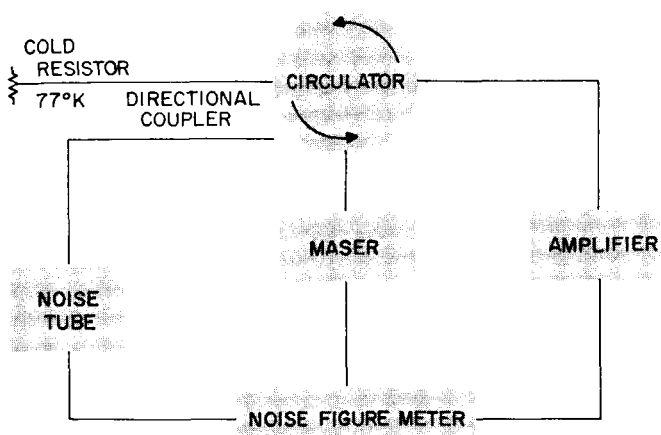


Figure 76. System for measuring noise temperature of solid state maser

was found to be as low as 35°K. This is encouraging since the Raytheon circulator contributes 15 to 20°K of this total. Further testing is in progress to improve the system and the measurement techniques. The dewar design is now nearly completed.

The very promising application of thin magnetic films to computer memories and logistics is being actively pursued. Equipment for testing the magnetic characteristics of evaporated permalloy films is nearing completion.

In support of a cryogenic gyro project which is in progress at JPL, considerable effort has been spent on the development of suitable superconducting films. Lead films have been deposited on various substrates both electrolytically and by evaporation. They display consistent superconductivity and have been successfully applied to the cryogenic gyro. Niobium has been evaporated to yield metallic deposits; however, the resultant films are not superconducting. The reasons for this are not fully understood but are believed to be related to chemical combination of the depositing metal with residual gases. Oxide film insulation on niobium wires and other structures has been provided where required by anodic treatment.

Concurrently with these projects, work is proceeding on the extension of the facilities for microminiaturization. This includes electron bombardment guns and floodlight sources to heat the materials to their vapor phase, micro-mask supports, and registration systems for accurate location of evaporate device elements in the vacuum equipment as well as the development of photographic and other tools for electroforming of masks on stainless steel and metallized glass substrates.

C. Molecular Aggregate Devices

1. Thin-Film Techniques

Studies of thin-film techniques and development work on their application to various devices are in progress at the Laboratory. The areas of activity include optical, micro-electronic, magnetic, and cryogenic applications of thin-film techniques.

In the field of optics, mirrors for collecting Lyman-alpha radiation in space are under development as part of a future spacecraft payload experiment. They consist of thin metallic reflecting surfaces on molded, accurately shaped plastic substrates. Their qualifications for payload use are evaluated by spectrophotometric methods on small 2 × 2-inch sample replicas.

In the area of microminiaturization and molecular electronics, a long-range investigation of single-crystal semiconductor films has been initiated with the ultimate objective of developing non-epitaxial techniques for the production of active semiconductor elements and complete devices. Methods for highly concentrated spot heating and melting of germanium and similar materials are under study.

D. Gas Bearings

1. Closed-Cycle Gas Supply System

In the preceding *Research Summary* (Vol I), a closed-cycle vapor supply system for gas bearings and other applications in spacecraft has been described. Freon vapor is *thermally pumped* to the required operating pressure and recirculated in a closed loop.

The experimental arrangement shown in RS 36-1, Figure 47, has been modified. The tubular heating coil which served as an evaporator was replaced by a dome-shaped vessel filled about one-half with liquid Freon 113 into which a pancake-shaped Chromalox heater coil is immersed; it is connected through a wattmeter to a variable transformer which operates from the 220-volt supply lines. Figure 77 is a photograph of the modified arrangement.

In each series of tests, the vapor flow rate F through the valve which simulates the gas bearing was held con-

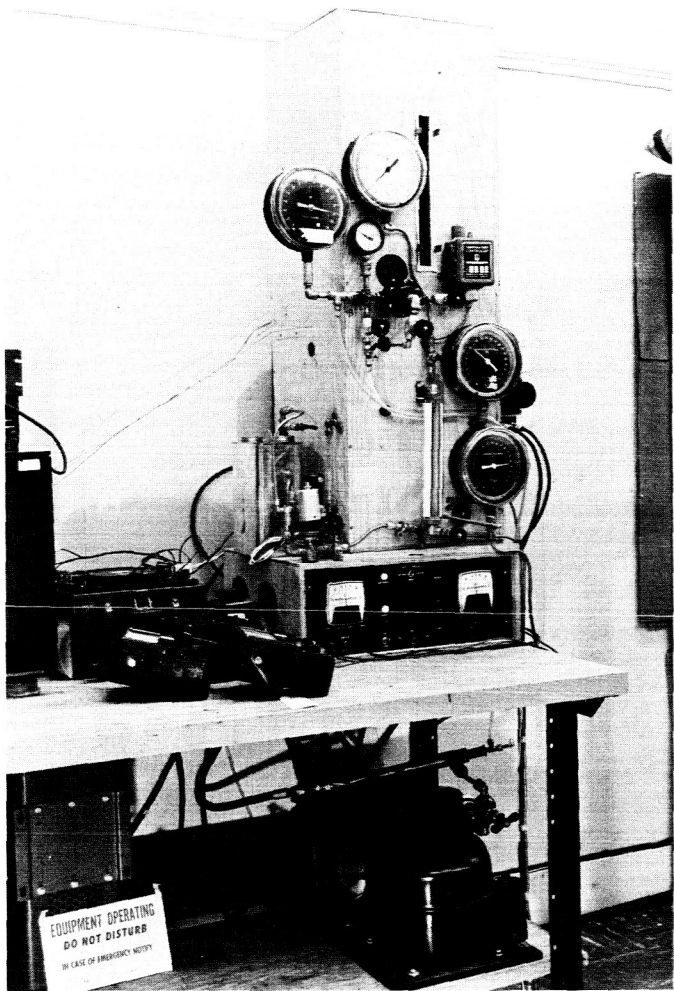


Figure 77. Closed-cycle gas supply experimental arrangement

stant and measured by a variable-orifice flowmeter on the downstream side, i.e., at atmospheric pressure. The wattage input to the heater coil was varied in uniform steps of 10 watts each, and both the pressure drop ΔP and the temperature T_F of the liquid (boiling) Freon in the evaporator were measured after they had reached steady state.

The results of four test runs at 1.0, 0.75, 0.50, and 0.25 cfm, respectively, are plotted in Figure 78. For a comparison of the experimental data with the predicted values, an estimate of the total heat losses is needed. To this end, the heater wattage was plotted in Figure 79 as a function of the vapor flow rate F with the pressure drop ΔP across the simulator valve as a parameter. For zero flow and zero pressure drop, a residual wattage of 70 watts is read from Figure 79. This value was also verified independently by operating the heater coil in *on-off* fashion at zero flow with a thermostatic relay set at

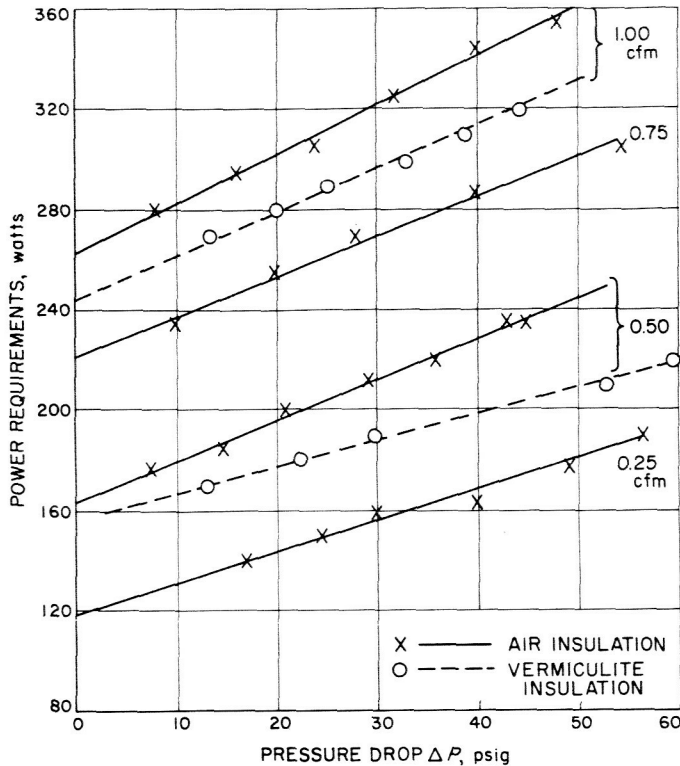


Figure 78. Thermal pumping power requirement as a function of pressure

118°F, the boiling temperature of the liquid Freon at atmospheric pressure. By measuring the *on-off* times and the wattage, the average wattage equaling the heat losses at $F = 0$ and $\Delta P = 0$ was determined to be 70 watts.

In RS 36-1, an energy balance calculation for loss-free operation at $F = 0.5$ cfm and $\Delta P = 48$ psig yielded a wattage requirement of 153.2 watts. The measured data at this operating point is $242 - 70 = 172$ watts. The difference of 18.8 watts can be accounted for by the heat input that is required to raise the temperature of the liquid Freon from 117.6°F (i.e., the boiling point at atmospheric pressure) to 212°F (i.e., the boiling point at 48 psig) which was omitted from the computed energy balance.

Further tests are now underway to verify the predicted performance more accurately by reducing the total heat losses of the system. The thermal insulation of the evaporator, simulating valve and flowmeter has been improved by filling the wooden enclosure with vermiculite. Also, the liquid Freon is preheated by returning it to the evaporator through a tubular helix around the outside wall of the evaporator. Test results so far obtained at $F = 1.0$ and 0.5 cfm indicate a substantial reduction in heat losses (dashed lines in Fig 78). The total wattage required

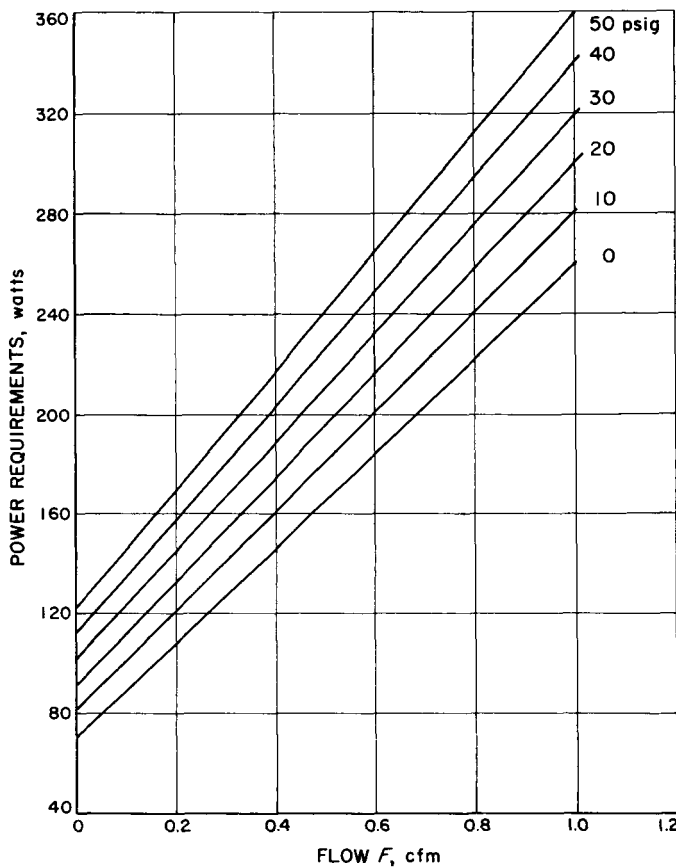


Figure 79. Thermal pumping power requirement as a function of flow rate

for a flow rate of 0.5 cfm and 48 psig pressure is now reduced to 208 watts. It should be noted that gas bearings can be designed to operate satisfactorily at considerably smaller flow rates and pressures. It can be expected therefore, that a closed-cycle Freon supply system for a typical gas bearing gyro requires less than 200 watts thermal pumping power.

2. Validity of Viscous Flow Theory

a. Reynolds and Mach numbers. The study of externally pressurized gas-lubricated bearings (pad-type, journal, and spherical bearings) which was described in CBS 63 to 68 and RS 1 to 7 yielded, in general, very satisfactory correlation between experiment and theory. The analytical approach used was the viscous flow theory; it treats the thin gas film in the bearing gap as subject to isothermal expansion and viscous forces only. Inertial forces are considered negligibly small; the flow is laminar and subsonic throughout the film. Obviously, this theory is valid only within a certain regime of fluid parameters and bearing dimensions. If its limitations can be estab-

lished, the performance of gas bearings designed to operate within these limits can be predicted with considerable assurance.

The criterion which determines whether the flow is in the viscous or turbulent regime is the Reynolds number Re ; the flow is subsonic as long as the Mach number M is smaller than 1. Reynolds numbers and Mach numbers have been calculated for the single-orifice circular pad bearings described in Reference 2 and in CBS 63 to 66. The Reynolds number is defined by

$$Re = \frac{Vh}{v} \quad (1)$$

and the Mach number by

$$M = \frac{V}{c} \quad (2)$$

where V is the local velocity of the gas in the film, h the height of the gap, v the kinematic viscosity, and c the speed of sound in the gas.

In the circular pad bearing (see CBS 66, Fig 73) the gas velocity at a distance r from the center is

$$V = \frac{Q}{2\pi rh} \quad (3)$$

where Q is the volumetric rate of flow.

If Equation (3) is inserted in (1), we find that in the circular pad bearing the Reynolds number Re is independent of the gap height h , i.e.,

$$Re = \frac{Q}{2\pi rv} \quad (4)$$

The Mach number M at a radius r is

$$M = \frac{V}{c} = \frac{Q}{2\pi rbc} \quad (5)$$

As an example, Reynolds numbers and Mach numbers for the circular pad bearing with $R = 0.565$ inch, $R/R_0 = 36.2$, have been calculated for a plenum pressure $P_{PL} = 32$ psig. The maximum of Re and M occurs for $r = R_0$, i.e., at the entrance to the gap; these values are plotted in Figure 80. The Mach number M has also been computed for the exit radius R for reasons explained later.

b. Relative importance of inertial and viscous forces. The relative importance of the viscous and inertial forces in the bearing can now be evaluated. In the Navier-Stokes equation,

$$\frac{\delta p}{\delta r} = \mu \frac{\delta^2 u}{\delta Y^2} - \rho u \frac{\delta u}{\delta r}, \quad (6)$$

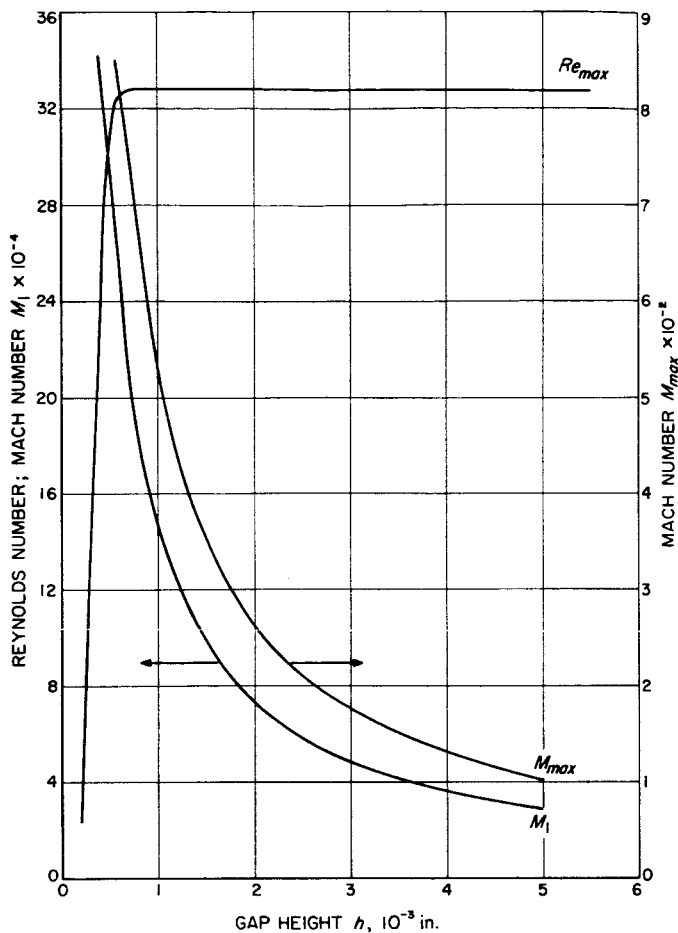


Figure 80. Mach and Reynolds numbers of pad bearing with $R = 0.565$ inch

the first term on the right is the contribution of the viscous forces, and the second term that of the inertial forces.

Solutions of Equation (6), with certain simplifying assumptions, have been obtained by several authors (Refs 3, 4). Comolet in his paper has shown that, for isothermal expansion of the gas, the pressure P at radius r can be expressed in the form

$$\frac{\left(\frac{P}{P_1}\right)^2 - 1}{\log \frac{R}{r}} + 1.68 \frac{\left(\frac{R}{r}\right)^2 - 1}{\log \frac{R}{r}} M_1^2 = \frac{12 \mu RV}{b^2 P_1} \quad (7)$$

in which the first term on the left is the contribution of the viscous and the second term that of the inertial forces.

Comolet has written Equation (7) in the form

$$\frac{X + Y}{M_1} = \frac{12 \mu RV}{b^2 P_1} \quad (7a)$$

and has verified experimentally that, for a given gap h ,

$(X + Y)/M_1$ has a constant value, as demanded by (7a), up to a critical Reynolds number Re_c of approximately 550. Below this value, therefore, Equation (7) is exact and can be used to accurately determine the relative effect of the viscous and inertial forces, i.e., the ratio

$$\frac{X}{Y} = \frac{\left(\frac{P}{P_1}\right)^2 - 1}{1.68 \left[\left(\frac{R}{r}\right)^2 - 1 \right] M_1^2} \quad (8)$$

If now it is stipulated that the inertial forces can be neglected as long as their contribution stays below 1% of that of the viscous forces, we obtain the limit for M_1 , from letting $X/Y = 100$ in (8), or

$$M_1^2 = \frac{1}{100} \frac{\left(\frac{P}{P_1}\right)^2 - 1}{1.68 \left[\left(\frac{R}{r}\right)^2 - 1 \right]} \quad (9)$$

from which the limit of M_1 can be determined for various pressures P and radii r . Figure 81 is a plot of $M_{1,Lim}$

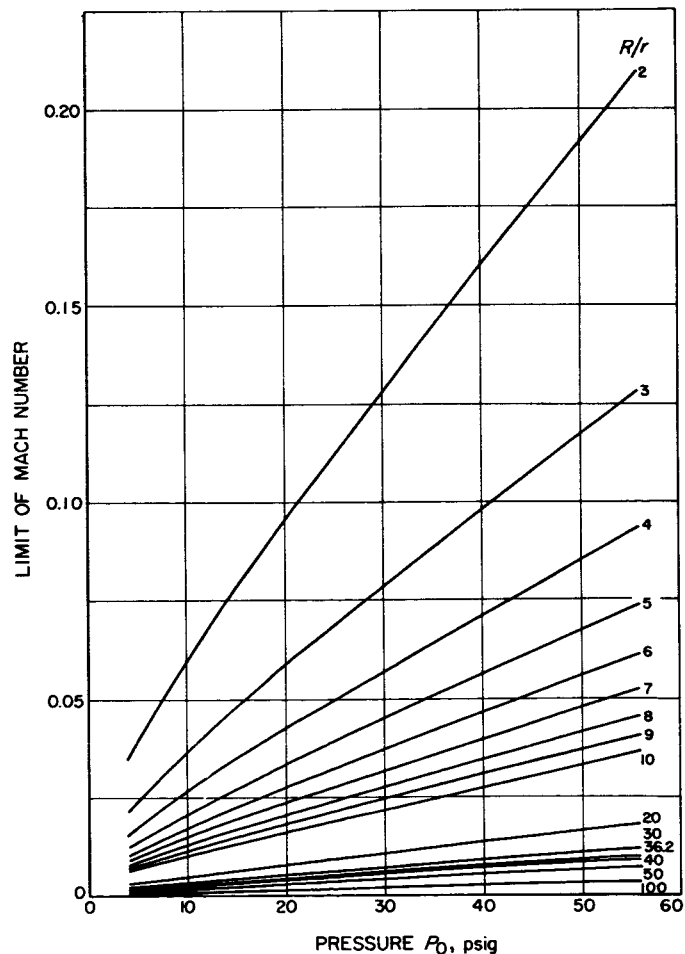


Figure 81. Limit of Mach number for $X/Y = 100$

calculated from (9) for pressures up to 56 psig and various ratios of R/r . For example, the pad bearing with $R/R_0 = 36.2$ which was previously investigated, operates at Mach $M_1 = 0.00303$ (Fig 80) at a gap h of 0.5×10^{-3} inch, $P_{PL} = 32$ psig and $P_0 = 18$ psig. Figure 80 shows that the limit is Mach 0.004, i.e., the inertial force is well under 1% of the viscous force. This figure also shows that the maximum Reynolds number (at $r = R_0$) at the same operating point of this bearing is $Re = 30.3$ which is well below the critical value of $Re_{cr} = 550$.

A step bearing with $R/R_0 = 2$, operating at 48 psig plenum pressure, $P_0 = 14.1$ psig, and $h = 0.4 \times 10^{-3}$ inch may further illustrate the validity of the *viscous theory*. Figure 81 shows that the inertial force is less than 1% of the viscous force as long as M_1 does not exceed 0.075; the bearing actually operates at $M_1 = 0.00335$ and at a maximum Reynolds number of $Re_{max} = 23$. It is, therefore, not surprising that in the previous investigation of this type of bearing the viscous flow theory yielded very satisfactory agreement with the experiment.

c. *Importance of minimizing flow rates.* From the above discussion, an important practical conclusion can be drawn pertaining to the design of externally pressurized gas bearings, namely that gas flow rates should be kept as low as possible. Both the Reynolds number and the Mach number are proportional to the local gas velocity V which in turn is proportional to the volumetric flow rate Q . Keeping the latter as low as possible not only assures staying within the viscous regime but also minimizes the risk of abnormal entrance effects associated with the development of shockwaves, negative pressure profiles and loss of load carrying capacity. By using small orifices, the additional bonus of economy of gas consumption is gained as has been pointed out in the discussion of elastic orifices in the preceding *Research Summary* (Vol I).

E. Parasol Solar Panel and Antenna

This study was initiated to examine some of the constraints associated with folding solar panel and antenna configurations. The result is a general design concept

unique in several respects. Both solar panels and antennas for spacecraft are large-sized, compared to other equipment. This presents a problem of storage and manipulation. In addition there is the problem, particularly with solar panels, of protection during launch and ejection. Large rigid structures have been required to properly support the solar cells. The idea of folding panels, parasol fashion, is chosen here to reduce the space required to contain them and to provide a shape which lends itself to protection support by vibration-damping material such as resilient cellular foam.

1. Construction of Parasol Model

A parasol model, shown in Figure 82, was constructed to demonstrate the physical size relationship of the components and to demonstrate the fundamental principle of operation. The panel disk is 20 inches in diameter, and the space required for storing is 6 inches in diameter and 11 inches long. To demonstrate the operation, the panel is attached to a telescoping boom long enough to extract the panel from the protective shell and extend it beyond the shell far enough to allow for orientation. The Sun-seeking mechanism is demonstrated on the model by a ball joint attachment between the disk and the boom. An air pump is used to pressurize the telescope in the model to eject the disk (Fig 82d). The disk panels are spring-loaded to the mounting collar to open the disk when ejected from the cushioned shell.

2. Size Comparison

Proportioning roughly from the model size, a parasol solar panel to provide a 20-ft² area (as used on *Ranger A*) would require a cylinder 10 inches in diameter and 16 inches long. Since one panel disk could only track through 180 spherical degrees, one 31-inch disk would be required on each of the two sides of the spacecraft. These would be stored in cylindrical spaces each 10 inches in diameter and 16 inches long. This dual configuration would allow full spherical tracking without spacecraft altitude control.

The parasol method of storing and erecting solar panels and antennas appears to have the following advantages:

- (1) It requires less space to store than other methods.
- (2) It offers an easy shape to protect and aid ejection.
- (3) It allows for simple operating and erecting mechanisms.
- (4) It allows for a reduction in weight required for supporting hardware by replacing metal with foam.

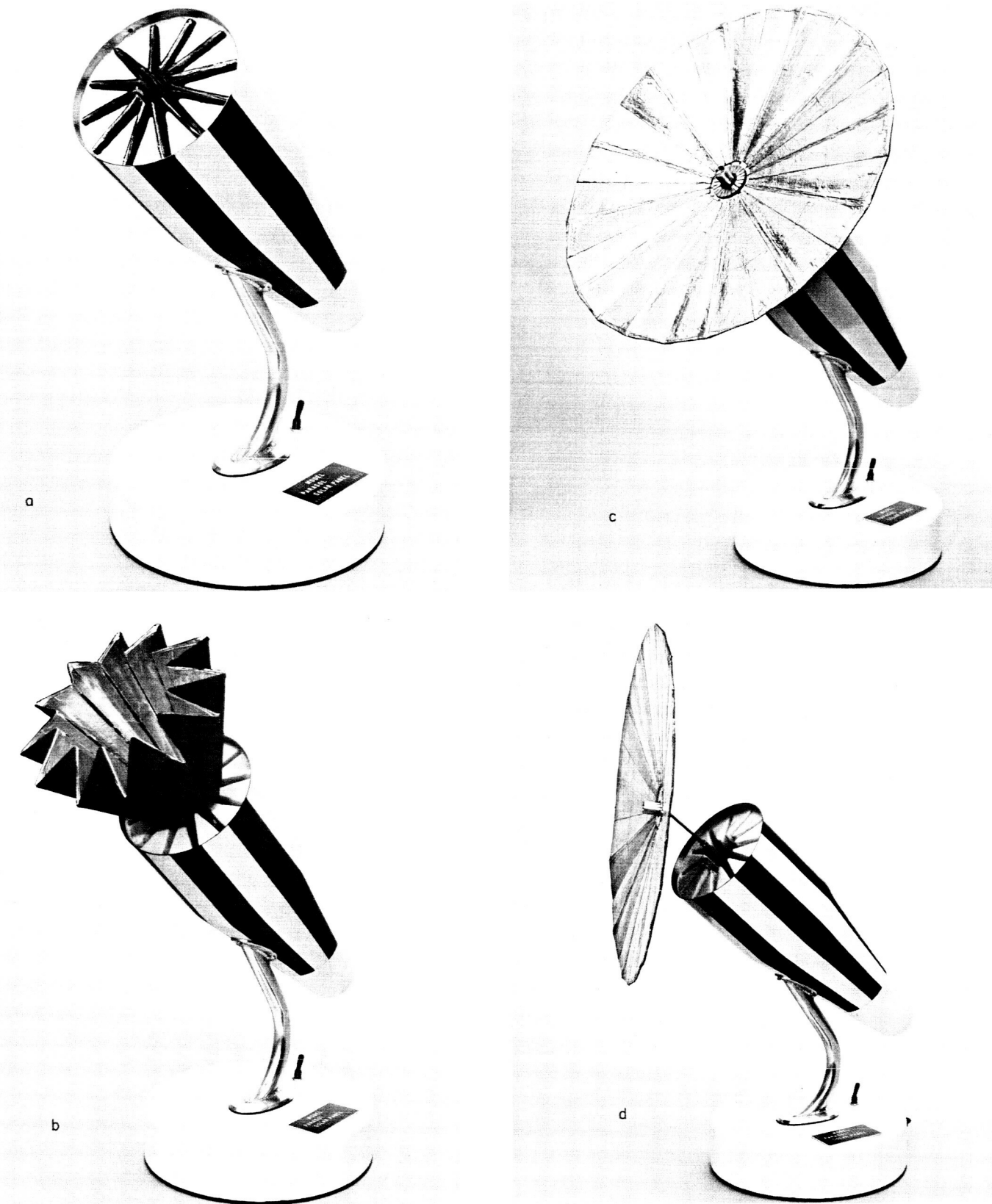


Figure 82. Model of parasol solar panel and antenna

References

1. James, H. M., Nichols, N. B., and Phillips, R. S., "Theory of Servomechanisms," Vol 25, *MIT Radiation Laboratory Series*, McGraw-Hill Book Co., New York, 1947.
2. Laub, J. H., *Hydrostatic Gas Bearings*, Progress Report No. 20-353, Jet Propulsion Laboratory, Pasadena, October 3, 1958.
3. Deuker, E. A., et Wojtech, A., "Écoulement radial d'un fluide visqueux entre deux disques très rapprochés. Théorie du palier à air." *Revue Générale de l'Hydraulique*, 65:227-234 and 66:283-294, 1951.
4. Comolet, R., "Écoulement d'un fluide entre deux plans parallèles. Contribution à l'étude des butées d'air," *Service de documentation et d'information technique de l'aéronautique*, Paris, 1957.